Journal of Seismic Exploration

ISSN: 0963-0651

Volume 34 · Issue 1
2025

ACCSCIENCE PUBLISHING

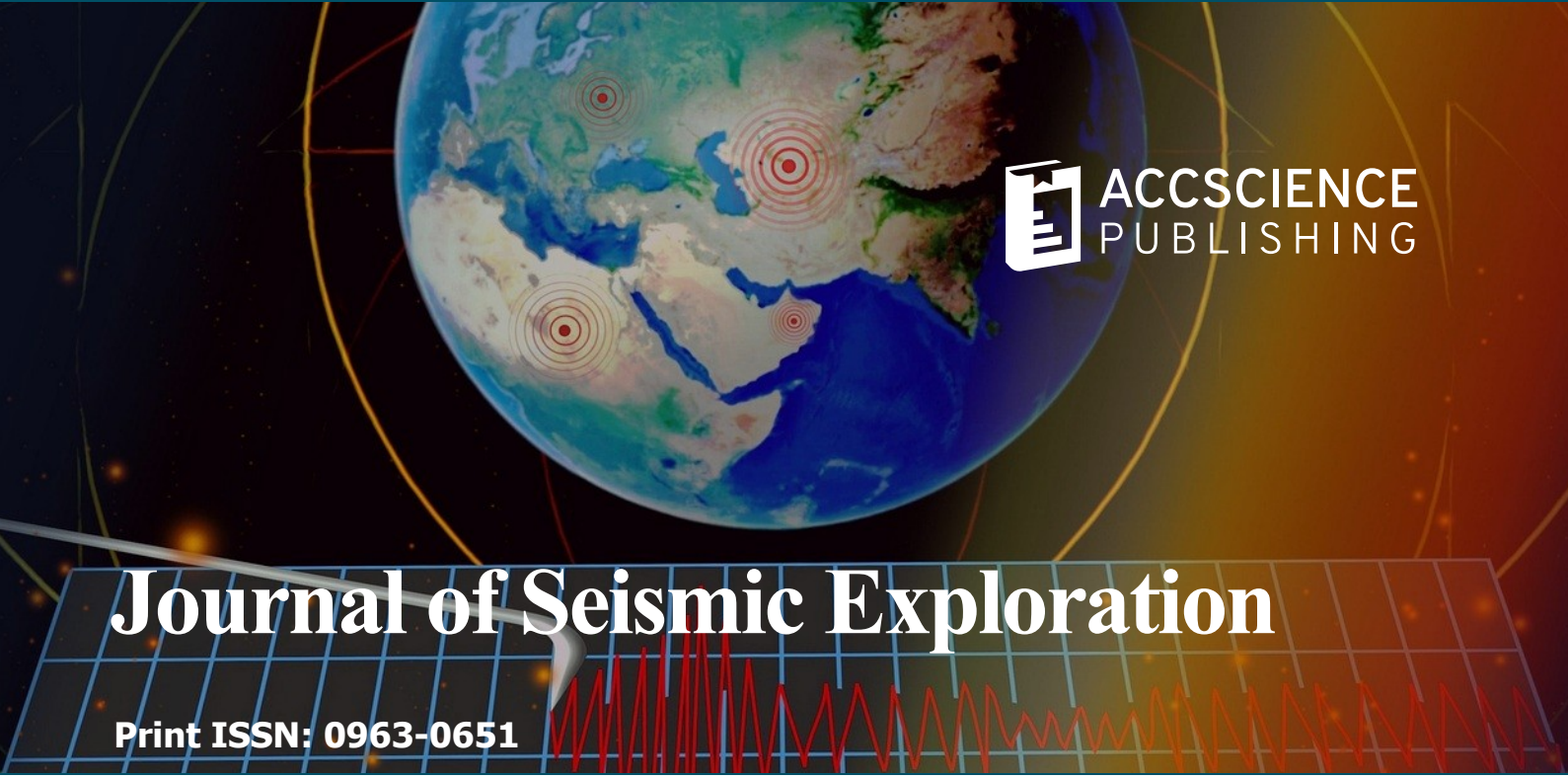

Journal of Seismic Exploration

Print ISSN: 0963-0651

The Journal of Seismic Exploration (JSE) is an international medium for the publication of research in seismic modeling, processing, inversion, interpretation, field techniques, borehole techniques, tomography, instrumentation and software. The aim and goal of JSE is to serve the interests and objectives of seismic petroleum exploration. All seismic processing methods have assumptions and prerequisites- and when they are satisfied methods are effective-and when they are violated methods become ineffective and can fail. The latter contributes to drilling dry hole exploration wells and suboptimal development wells.

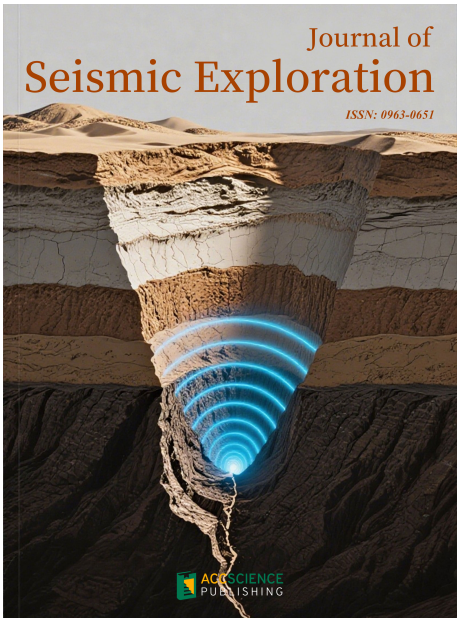

About the Publisher

AccScience Publishing is a publishing company based in Singapore. We publish a range of high-quality, open-access, peer-reviewed journals and books from a broad spectrum of disciplines.

Contact Us

Managing Editor
jse.office@accscience.sg

AccScience Publishing
9 Raffles Place, Republic Plaza 1 #06-00 Singapore 048619.

Volume 34 • Issue 1 • 2025
ISSN 0963-0651 (print)

Journal of Seismic Exploration

ACCSCIENCE PUBLISHING
Access Science Without Barriers

JOURNAL OF SEISMIC EXPLORATION

ISSN: 0963-0651 (print)

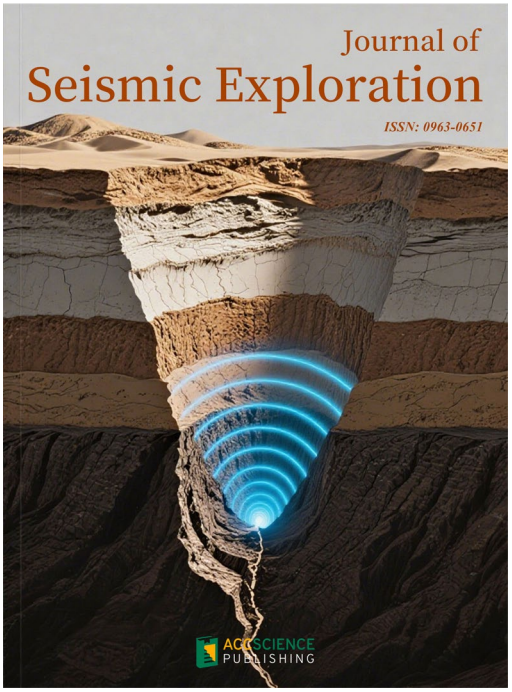

Editorial and Production Credits

Publisher: AccScience Publishing
Managing Editor: Gary Liu
Production Editor: Lim Mingyuan
Article Layout and Typeset: Sinjore Technologies (India)

Supplementary file

Supplementary files of articles can be obtained at https://accscience.com/journal/JSE/34/1.

Disclaimer

AccScience Publishing is not liable to the statements, perspectives, and opinions contained in the publications. The appearance of advertisements in the journal shall not be construed as a warranty, endorsement, or approval of the products or services advertised and/or the safety thereof. AccScience Publishing disclaims responsibility for any injury to persons or property resulting from any ideas or products referred to in the publications or advertisements. AccScience Publishing remains neutral with regard to jurisdictional claims in published maps and institutional affiliations.

Journal of Seismic Exploration

Editorial Board

ACCSCIENCE PUBLISHING

Volume 34 | Issue 1 | 2025 | Page 1 – 81 |

Journal of Seismic Exploration

https://accscience.com/journal/JSE

CONTENTS

ACCSCIENCE PUBLISHING

Journal of Seismic Exploration

ARTICLE

Regional patterns of seismic b-values variations in the Himalayan region (71.6°E – 95.5°E and 37.5°N – 26.6°N)

Ram Krishna Tiwari*, Anil Subedi, Dilip Parajuli, Santosh Dharel, Anil Neupane, Hari Subedi, Bishow Raj Timsina, and Harihar Paudyal

Department of Physics, Birendra Multiple Campus, Tribhuvan University, Bharatpur, Chitwan, Nepal

Abstract

This study conducts a detailed seismic hazard assessment of the Himalayan region. It focuses on studying how b-values, based on the Gutenberg–Richter law, vary throughout location and time. These fluctuations assist measuring tectonic stress and provide insights into the region's seismic activity. This research focuses on five Himalayan sub-regions: Far Western, Western, Central-I, Central-II, and Eastern. It incorporates earthquake data spanning 1964 – 2023 obtained from the International Seismological Centre. The data were de-clustered using the Reasenberg method and examined by Maximum Likelihood Estimation. The results demonstrated considerable spatial variability in b-values across the Himalayan sub-regions. The Far Western Himalayas displayed the greatest b-value (0.93 ± 0.02), indicating frequent smaller earthquakes and lesser tectonic stress. In contrast, the Eastern (0.68 ± 0.02) and Central-I (0.69 ± 0.03) regions had the lowest b-values, implying more stress accumulation and a greater risk of future strong earthquakes. Temporal fluctuations, as a decrease in b-values preceding to the 2015 Gorkha earthquake (Mw 7.8) and a subsequent increase in Central-II (1.19 ± 0.03), highlighted the retention and release cycles. The Eastern Himalayas, particularly the Dhubri-Chungthang fault zone seismic gap in Bhutan, are considered a key high-risk zone. This region, with b-values ranging from 0.65 to 0.75, has remained unruptured since the 1934 Bihar-Nepal earthquake (Mw 8.4). The findings showed the influence of the continual convergence of the Indian and Eurasian plates (~20 mm/year) on strain heterogeneity. This study underlines the vital demand for intensive seismic monitoring, resilient infrastructure, and disaster readiness in low b-value areas to alleviate catastrophic risks in one of the globe's most tectonically active regions.

Keywords: b-value; Gutenberg–Richter law; Himalayan region

***Corresponding author:**
Ram Krishna Tiwari
(ram.tiwari@bimc.tu.edu.np)

Citation: Tiwari RK, Subedi A, Parajuli D, *et al*. Regional patterns of seismic b-values variations in the Himalayan region (71.6°E – 95.5°E and 37.5°N – 26.6°N). *J Seismic Explor.* 2025;34(1): 1-11.
doi: 10.36922/JSE025210006

Received: May 25, 2025

Revised: July 5, 2025

Accepted: July 8, 2025

Published online: July 28, 2025

1. Introduction

The Himalayan Mountain Range, the tallest mountain chain in the world, traverses five countries – India, Nepal, Bhutan, China (Tibet), and Pakistan – and extends over 2,400 km in southern Asia.[1] The continual collision between the Indian and Eurasian tectonic plates, which began around 50 million years ago (Mya) after the Neo-Tethys Ocean closed, is responsible for its construction.[2] The Indian Plate subducted northward beneath Eurasia between 70 and 50 Mya, closing the Tethys Ocean and leaving

behind the Indus-Tsangpo Suture Zone, a geological indicator of the ancient oceanic crust, was the primary step in the orogenesis of the Himalayas.[3] The continental collision phase (50 – 40 Mya) resulted in massive crustal shortening, folding, and thrust faulting, which uplifted the Greater Himalayas through systems, such as the Main Central Thrust, while the Main Boundary Thrust and Main Frontal Thrust distinguish the Lesser Himalayas and the young, sediment-rich Siwalik Hills, respectively.[4,5] Ongoing northward convergence of the Indian Plate at 5 – 10 mm/year sustains tectonic activity, driving uplift of peaks, such as Mount Everest and accumulating stress along major faults, such as the Main Himalayan Thrust (MHT), a primary source of strong earthquakes.[6,7] This dynamic process ensures continued seismic hazard in the region, exemplified by historical earthquakes and the persistent risk of future events as strain energy is episodically released.[8,9]

An earthquake is defined as the sudden release of accumulated stress along locked tectonic plate boundaries or intraplate zones, where abrupt crustal movement generates seismic waves.[9,10] In the Himalayas, this process is driven by the ongoing India-Eurasia collision, which has generated significant seismicity linked to strain release along the MHT.[2,6] One of the notable seismic activities in the Himalayas is the 1905 Kangra earthquake (Mw 7.8), where a segment of the western Himalayan front was ruptured, releasing stress accumulation in the Kangra reentrant.[11,12] The Bihar-Nepal earthquake (Mw 8.1) in 1934 involved slip along a ~250 km portion of the MHT, illuminating shallow decollement dynamics.[13-16] The 1950 Assam-Tibet earthquake (Mw 8.6) highlights the complexity of oblique convergence near the eastern Himalayan syntaxis, where thrust and strike-slip faulting combine to produce bimodal faulting.[17,18] The 2005 Kashmir earthquake (Mw 7.6) highlighted strain partitioning in the western syntaxis, with thrust and strike-slip components.[8,19,20] Most recently, the 2015 Gorkha earthquake (Mw 7.8) in central Nepal ruptured a 150 km × 60 km patch of the MHT, leaving deeper segments unbroken and underscoring heterogeneous coupling.[8,21-23] These events, spanning the MHT's strike, reveal segmented rupture behavior and variable locking depths, with GPS-derived convergence rates (~18 – 20 mm/year), suggesting ongoing strain accumulation.[6]

By analyzing the b-value in the Gutenberg–Richter law, this study aims to identify zones of differential stress accumulation, potential asperities, and fault maturity across the Himalayan region (71.6°E – 95.5°E and 26.6°N – 37.5°N), subdivided into five distinct sub-regions. Based on the probabilistic seismic hazard assessment report of India, tectonic features, and geology, the region has been broadly divided into four sections,[26-28] with the western section further subdivided for improved analysis. As a result, As a result, we have categorized the Himalayan region into five zones: Far Western, Western, Central-I, Central-II, and Eastern (Figure 1). Each of these zones has been defined based on distinct geological and tectonic characteristics to ensure a comprehensive assessment.

1.1. Frequency magnitude distribution

The frequency-magnitude distribution (FMD) of earthquakes[29] is a fundamental statistical relationship in seismology. It describes how the frequency of earthquakes scales with their magnitude, using the following equation:

$$\log N = a - bM \quad \text{(I)}$$

In Equation I, N is the cumulative number of events having magnitude $\geq M$; M is the magnitude of earthquakes; the constant a is the seismicity of the region; and b is the b-value of the earthquake frequency magnitude distribution.[29] The b-value, a key parameter in the Gutenberg–Richter law, quantifies the relative frequency of small to large earthquakes, where a lower b-value indicates a higher likelihood of large-magnitude events due to elevated tectonic stress, while a higher b-value reflects frequent small earthquakes and lower crustal strain.[30-32] To assess regional stress accumulation and evaluate the seismic hazard potential, seismologists have analyzed spatial and temporal fluctuations in b-values around the globe. As an example, researchers analyzed spatiotemporal variations in b-value within the subducting slab before the 2003 Tokachi-oki earthquake (M 8.0), Japan, to identify precursory seismic signatures.[33] Similarly, the b-value anomalies were noticed before the Assam Earthquake on April 28, 2021.[34] In addition, the low b-value anomaly identified in the west of Gorkha highlights the zone with potentially strong seismic activity in the future.[35]

2. Data and methods

An extensive earthquake catalogue covering a long period is essential for studying the seismic activity of any region. In this study, we focused on the Himalayas, located between 71.6°E and 95.5°E, and utilized earthquake data for the period from 1964 to 2023, from the International Seismological Centre catalogue.[36-38] The earthquake magnitudes in the catalogue are reported in mb (body-wave magnitude). The dataset comprises both dependent (foreshocks and aftershocks) and independent (mainshocks) events, but to ensure accurate analysis, only independent earthquakes are considered by applying de-clustering using the Reasenberg algorithm.[39] The de-clustering process was carried out in ZMAP

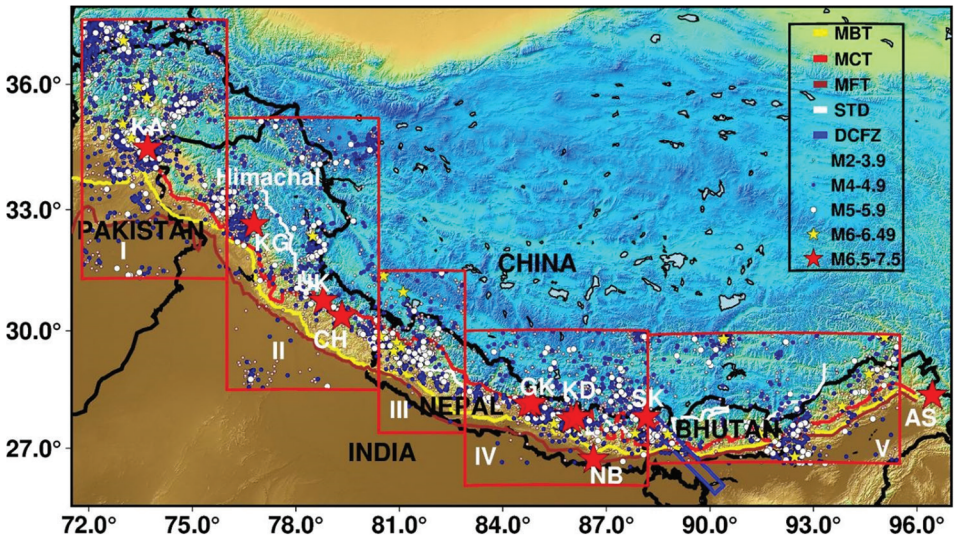

Figure 1. Study region with earthquake distribution. Red star indicates the earthquake >6.4 mb and notable past earthquakes, and red rectangular box are subdivided regions. UK stands for Mw 6.8 Uttar Kashi earthquake, CH stands for Mw 6.4 Chamoli earthquake, GK stands for Mw 7.8 Gorkha earthquake, NB stands for Mw 8.4 Nepal-Bihar earthquake, KA stands for Mw 7.6 Kashmir earthquake, SK stands for Mw 6.9 Sikkim earthquake, KG stands for Mw 7.8 Kangra earthquake, and AS stands for Mw 7.8 Assam earthquake. The blue rectangle stands for Dhubri-Chungthang Fault Zone (DCFZ).[24,25]

software (Swiss Seismological Service, Switzerland).[40] The segmented study regions are:

(i) Far Western Himalayan region (31.3°N – 37.5°N and 71.6°E – 76°E): A total of 3445 earthquake events with a magnitude of 3.0 mb or greater were recorded. After applying the de-clustering process, 47 clusters were identified, and following the removal of dependent events, 2867 independent events were retained.

(ii) Western Himalayan region (28.8°N – 35.2°N and 76°E – 80.2°E): A total of 1040 earthquake events with a magnitude of 3.0 mb or greater were recorded. After the de-clustering process, 24 clusters were identified, and following the removal of dependent events, 1004 independent events were retained.

(iii) Central-I Himalayan region (27.4°N – 31.5°N and 80.2°E – 82.9°E): A total of 529 earthquake events with a magnitude of 3.0 mb or greater were recorded. After the de-clustering process, 11 clusters were identified, and following the removal of dependent events, 494 independent events were retained.

(iv) Central-II Himalayan Region (26.03°N – 30°N and 82.9°E – 88.2°E): A total of 1482 earthquake events with a magnitude of 3.0 mb or greater were recorded. After the de-clustering process, 35 clusters were identified, and following the removal of dependent events, 1079 independent events were retained.

(v) Eastern Himalayan region (26.6°N – 29.9°N and 88.2°E – 95.5°E): A total of 767 earthquake events with a magnitude of 3.0 mb or greater were recorded. After the de-clustering process, 8 clusters were identified, and following the removal of dependent events, 706 independent events were retained.

The b-value was determined using the maximum likelihood estimate approach, which remains unaffected by large-magnitude earthquakes. In addition, the magnitude of completeness was computed using the first derivative of the frequency-magnitude curve.[32] The formula[41,42] for b-value estimation is as follows:

$$b = \frac{\log_{10} e}{M_a - (M - \frac{\Delta M}{2})} \quad \text{(II)}$$

where M_a is the average of all magnitudes; M is the minimum magnitude in the catalogue; and ΔM is the binning width of the catalogue. The standard deviation in b-value (δb), as recommended elsewhere,[43] is provided in the following:

$$\delta b = 2.3b^2 \sqrt{\frac{\sum_i^N \left(M_i - M_a\right)^2}{n_s\left(n_s - 1\right)}} \quad \text{(III)}$$

where M_i denotes the individual earthquake magnitudes; M_a is the average magnitude of all the earthquakes considered; and n_s refers to the total number of earthquake samples used in the calculation. The expression $\sum_i^N \left(M_i - M_a\right)^2$ represents the sum of the squared differences between each magnitude and the mean magnitude.

3. Results and discussion

As mentioned in the past literature, temporally declining b-values precede major earthquakes, signaling stress concentration,[44,45] and spatially, low b-values correlate with locked, high-stress zones, while high b-values reflect fractured, aseismic regions.[46,47] Together, these patterns highlight the utility of b-values in mapping stress heterogeneity and identifying seismogenic potential. To better understand these dynamics, we investigated spatial and temporal b-value variations in the Himalaya to quantify stress heterogeneity and earthquake likelihood. The estimated b-values for all five regions (Far Western, Western, Central-I, Central-II, and Eastern) are illustrated in Figure 2, with their corresponding numerical values provided in Table 1.

The Far Western region (Figure 2A) exhibits the highest b-value (0.93 ± 0.02), indicating a predominance of small magnitude earthquakes, which is a common feature of tectonically active zones. Conversely, the Central-I (Figure 2C) and Eastern regions (Figure 2D)

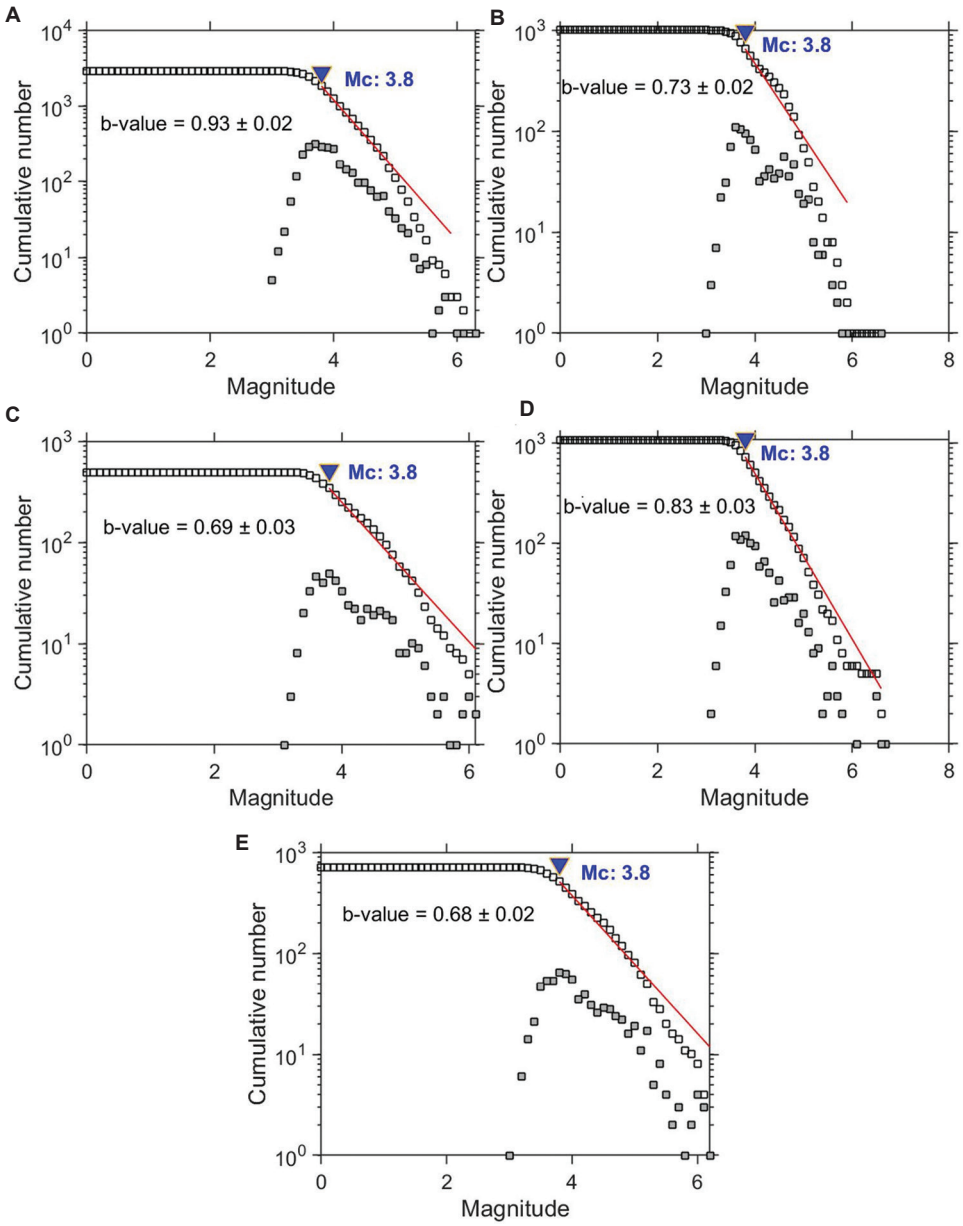

Figure 2. b-value and magnitude of completeness plots of Far Western Himalayan region (A), Western Himalayan Region (B), Central-I Himalayan Region (C), Central-II Himalayan Region (D), and Eastern Himalayan Region (E)

Table 1. b-value and magnitude of completeness in five regions of the Himalayan

Region	b-value	Magnitude of completeness (Mc)	Magnitude range (in M_b)
Far Western	0.93±0.02	3.8	3 – 6.9
Western	0.73±0.02	3.8	3 – 6.6
Central I	0.69±0.03	3.8	3 – 6.1
Central II	0.83±0.03	3.8	3 – 6.9
Eastern	0.68±0.02	3.8	3 – 6.2

have the lowest b-values (0.69 ± 0.03 and 0.68 ± 0.02, respectively), suggesting a lower frequency of small earthquakes and a greater potential for stress accumulation, which may contribute to the occurrence of larger seismic events.[48,49] Meanwhile, the Western (Figure 2B) and Central-II (Figure 2D) regions demonstrate moderate b-values (0.73 ± 0.02 and 0.83 ± 0.03, respectively), reflecting a more balanced seismic activity pattern.[50,51] These variations in b-values provide crucial insights into seismic behavior and potential hazard levels across different regions. In the preceding work, b-values calculated for the Himalayan region from 1900 to 2015, were reported as 0.98, 0.86, 0.85, and 0.74 for the Western, Central-I, Central-II, and Eastern zones, respectively, by Pudi *et al.*[26] Similarly, other studies have analyzed b-values across the Himalayas, demonstrating differences in stress and seismic hazard. Tiwari and Paudyal[52] discovered a b-value of 0.68 ± 0.03 in western Nepal (central Himalaya), indicating a high-stress zone with locked faults. Kumar and Sharma[53] reported b-values ranging from 0.7 to 1.1 in central Nepal (central Himalaya), showing stress heterogeneity after the 2015 Gorkha earthquake. Pathak *et al.*[54] discovered a high-stress environment in the Kumaun region of the western Himalayas, with a b-value of 0.59 ± 0.11. Similarly, Yadav *et al.*[55] reported low b-values ranging from 0.6 to 0.7 in the northeastern Himalayas, particularly along the MHT, indicating locked faults and high seismic potential. These low b-values across locations show the Himalayan belt's enormous stress and earthquake vulnerability.

The temporal fluctuations in b-values over the study region indicate varying stress regimes and seismic activities (Figure 3).

In the Far Western Himalaya (Figure 3A), a decrease in b-value from 1.04 (July 15, 1990) to 0.97 (November 11, 2015) during the 1980 – 2020 period signifies ongoing stress accumulation along the MHT.[56] The initial elevated b-value indicated stress relaxation through frequent little earthquakes, but the subsequent decline suggested an increase in strain concentration. The Western Himalayas (Figure 3B) exhibited a low b-value of 0.84 on August 30, 1995, associated with stress accumulation preceding the 1991 Uttarkashi (Mw 6.8) and 1999 Chamoli (Mw 6.4) earthquakes, influenced by locked parts of the Main Central Thrust.[57,58]

In the Central-I Himalayas (Figure 3C), the b-value of 0.94 recorded on December 14, 2006, throughout the period from 1995 to 2015 indicated moderate stress conditions with ongoing strain building along the MHT. In contrast, the Central-II Himalayas (Figure 3D) saw a significant increase in the b-value to 1.19 on May 10, 2015, following the Gorkha earthquake, indicating stress release through aftershocks.[59] The Eastern Himalayas (Figure 3E) exhibited consistently elevated and constant b-values (0.97 in 2014; 0.99 in 2016) from 1990 to 2015, indicating reduced stress attributable to crustal variability. This region constitutes a seismic gap that has remained unruptured since the 1934 Bihar-Nepal earthquake (Mw 8.4), with locked faults quietly collecting strain.[8,14] Our findings align with previous studies analyzing b-value variations in the Himalayas. Chetia *et al.*,[49] for example, observed b-value varying from 0.4 to 3.3 on the Himalayan and forehead region from 1964 to 2020.

The low b-value zones of the Himalayan region, extending from west to east, demonstrate a significant increase in seismic hazard potential (Figure 4).

In the Far Western Himalayas (72°E – 76°E) (Figure 4A), significant stress accumulation (b = 0.7 – 0.9) is noted in Himachal Pradesh, historically associated with the 1905 Kangra earthquake (Mw 7.8), where locked parts of the MHT maintain localized strain.[60] Proceeding eastward, the Western Himalayas (76°E – 80°E) (Figure 4B) display the sub-region's minimal b-values (0.6 – 0.7) in Uttarakhand (77°E – 79°E), which correlate with the Main Central Thrust and its rupture history, encompassing the 1991 Uttarkashi (Mw 6.8) and 1999 Chamoli (Mw 6.4) earthquakes.[23,58,61] Further east, the Central-I Himalayas (80.5°E – 82.5°E) (Figure 4C) in mid-western Nepal exhibit significantly low b-values (0.6 – 0.65), indicating unruptured segments of the MHT that have preserved residual stress following the 2015 Gorkha earthquake (Mw 7.8).[62] In proximity to this, the Central-II Himalayas (83°E – 88°E) (Figure 4D) exhibit a pronounced disparity: The western sector (83°E – 85°E) (Figure 4B) saw post-2015 stress release (b = 0.9 – 1.05), but the eastern sector (85°E – 88°E) retains low b-values (0.65 – 0.8), indicating persistent strain accumulation in central Nepal. The Eastern Himalayas (89°E – 95°E) (Figure 4D) are the most hazardous, with Bhutan's DCFZ gap (91°E – 93°E) exhibiting the lowest b-values (0.65 – 0.75) in the entire region.[24] This seismic gap, which has remained unruptured since the 1934

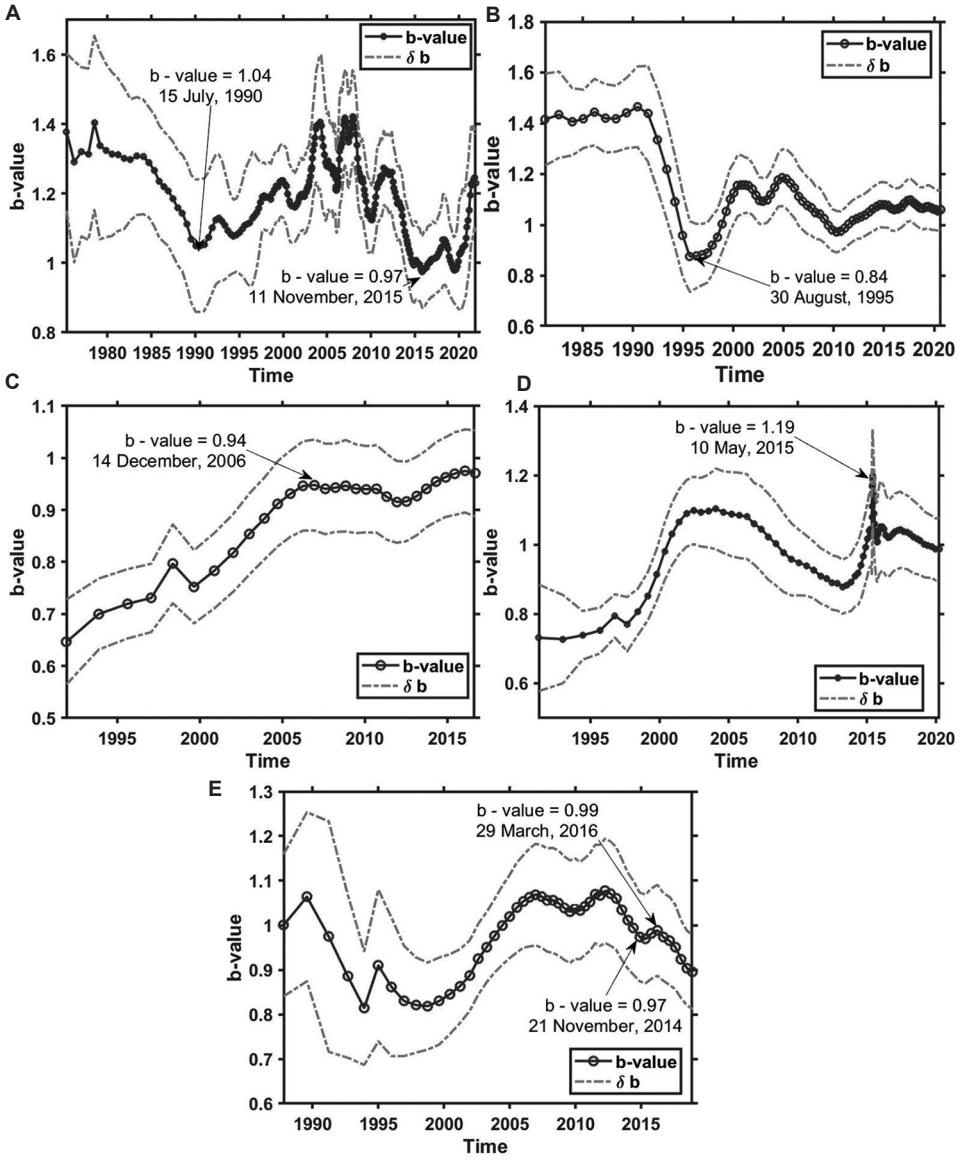

Figure 3. A time series analyzing b-value across Far Western Himalayan region (A), Western Himalayan Region (B), Central-I Himalayan Region (C), Central-II Himalayan Region (D), and Eastern Himalayan Region (E)

Bihar-Nepal earthquake, contains significant stress on the MHT, indicating an immediate threat of a mega-thrust event.[63] The west-to-east gradient from moderate strain to catastrophic potential highlights the Himalayas' dynamic tectonic interactions, driven by the Indian and Eurasian plates' continuous convergence (~20 mm/year). Thus, monitoring and disaster resilience are crucial in high-risk areas, such as Bhutan and central Nepal.

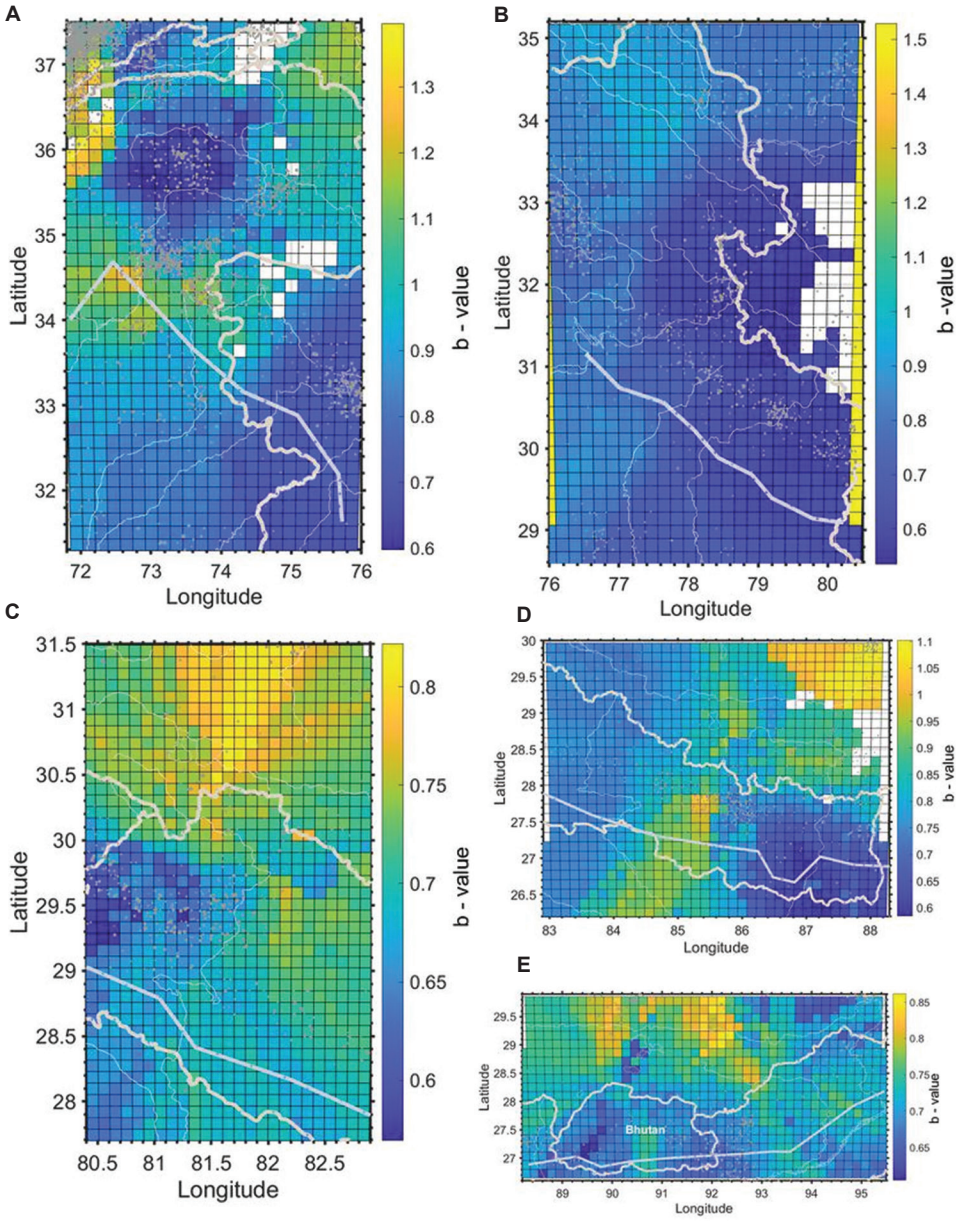

Figure 4. Spatial distribution of b-values across Far Western Himalayan region (A), Western Himalayan Region (B), Central-I Himalayan Region (C), Central-II Himalayan Region (D), and Eastern Himalayan Region (E)

4. Conclusion

In this study, earthquake data were obtained from the International Seismological Centre catalogue covering the Himalayan arc region between 71.6°E and 95.5°E for the period 1964 – 2023. The analysis was based on body-wave magnitude (mb), and to ensure accuracy, dependent events (foreshocks and aftershocks) were removed using the Reasenberg de-clustering algorithm implemented in MATLAB, allowing for the evaluation of only independent events (mainshocks).

The results of the investigation demonstrate clear spatial and temporal changes in b-values across distinct Himalayan sub-regions. Among the five zones investigated, the Far Western Himalayas demonstrated the greatest b-value (0.93 ± 0.02), which predicts a lower amount of tectonic stress accumulation and a dominance of small-magnitude earthquakes. In contrast, the Eastern Himalayas and Central-I region had the lowest b-values (0.68 ± 0.02 and 0.69 ± 0.03, respectively), indicating a higher accumulation of stress and a greater likelihood of big, devastating seismic occurrences.

Temporal analysis showed dynamic changes in b-values over time. For instance, the b-value in the Far Western Himalayas decreased from 1.04 in 1990 to 0.97 in 2015, reflecting increasing tectonic strain before the 2015 Gorkha earthquake (Mw 7.8). Similarly, the Western Himalayas recorded a b-value of 0.84 in 1995, which was associated with subsequent major earthquakes, including the 1991 Uttarkashi (Mw 6.8) and 1999 Chamoli (Mw 6.4) events. The Central-II region showed a sharp increase in b-value to 1.19 during 2015, attributed to stress release from aftershock activity. Notably, the Dhubri-Chungthang seismic gap in Bhutan, with a persistent b-value of 0.65 – 0.75, remains unruptured since the 1934 Bihar-Nepal earthquake (Mw 8.4), indicating a silent but critical accumulation of strain, potentially making it a future earthquake hotspot.

The interpretation of these results is significant. Low b-values point to regions with high stress accumulation and fewer small earthquakes, which are more prone to host large seismic events. Conversely, high b-values indicate frequent small earthquakes and lower potential for major seismic rupture. The temporal decrease in b-values in certain regions can serve as a potential indicator of impending earthquakes, whereas post-event increases often reflect stress release through aftershocks.

This work sheds light on the spatial and temporal patterns of seismicity over the Himalayan region. It helps to improve seismic hazard assessment and disaster risk mitigation strategies by identifying high-stress and earthquake-prone areas. The findings emphasize the significance of ongoing monitoring, particularly in low b-value zones, such as the DCFZ gap, and call for increased earthquake preparedness and mitigation activities in these susceptible locations.

Acknowledgments

We would like to acknowledge Birendra Multiple Campus, Tribhuvan University, Bharatpur, Chitwan, Nepal, for providing a conducive research environment.

Funding

None.

Conflict of interest

The authors declare that the research was conducted in the absence of any commercial or financial relationships that could be construed as a potential conflict of interest.

Author contributions

Conceptualization: Ram Krishna Tiwari
Formal analysis: Ram Krishna Tiwari
Investigation: Ram Krishna Tiwari
Methodology: Ram Krishna Tiwari
Supervision: Harihar Paudyal
Visualization: Anil Subedi, Dilip Parajuli, Santosh Dharel, Anil Neupane, Hari Subedi, Bishow Raj Timsina
Writing – original draft: Anil Subedi, Dilip Parajuli, Santosh Dharel, Anil Neupane, Hari Subedi, Bishow Raj Timsina
Writing – review & editing: Ram Krishna Tiwari, Harihar Paudyal

Availability of data

Data are freely available from the websites of the International Seismological Center.

References

1. DiPietro JA, Pogue KR. Tectonostratigraphic subdivisions of the Himalaya: A view from the west. *Tectonics*. 2004;23(5):1-20.

   doi: 10.1029/2003TC001554

2. Molnar P, Tapponnier P. Cenozoic tectonics of Asia: Effects of a continental collision: Features of recent continental tectonics in Asia can be interpreted as results of the India-Eurasia collision. *Science*. 1975;189(4201):419-426.

   doi: 10.1126/science.189.4201.419

3. Martin CR, Jagoutz O, Upadhyay R, *et al*. Paleocene latitude of the Kohistan-Ladakh arc indicates multistage India-Eurasia collision. *Proc Natl Acad Sci U S A*. 2020;117(47):29487-29494.

   doi: 10.1073/pnas.2009039117

4. Meigs AJ, Burbank DW, Beck RA. Middle-late miocene (>10 Ma) formation of the main boundary thrust in the western Himalaya. *Geology*. 1995;23(5):423-426.

   doi: 10.1130/0091-7613(1995)023<0423:MLMMFO>2.3.CO;2

5. Valdiya KS. The two intracrustal boundary thrusts of the Himalaya. *Tectonophysics*. 1980;66(4):323-348.

   doi: 10.1016/0040-1951(80)90248-6

6. Bilham R, Larson K, Freymueller J, *et al*. GPS measurements of present-day convergence across the Nepal Himalaya. *Nature*. 1997;386(6620):61-64.

   doi: 10.1038/386061a0

7. Bilham R, Ambraseys N. Apparent Himalayan slip deficit from the summation of seismic moments for Himalayan earthquakes, 1500-2000. *Curr Sci*. 2005;88(10):1658-1663.

8. Bilham R. Himalayan earthquakes: A review of historical seismicity and early 21st century slip potential. *Geol Soc Spec Publ*. 2019;483(1):423-482.

   doi: 10.1144/SP483.16

9. Houston H. An introduction to seismology, earthquakes, and earth structure. *Phys Today*. 2003;56(10):66-67.

   doi: 10.1063/1.1629009

10. Boulanouar A, Tiwari RK, Ahmed Z, Paudyal H. Fractal characteristics of earthquake occurrence in Al Hoceima city and its adjoining region, Morocco. *Geosyst Geoenviron*. 2025;4(3):100402.

    doi: 10.1016/j.geogeo.2025.100402

11. Bilham R. Earthquakes in India and the Himalaya: Tectonics, geodesy and history. *Ann Geophys*. 2021;47(2-3):839-858.

    doi: 10.4401/ag-3338

12. Kumar S, Wesnousky SG, Rockwell TK, Briggs RW, Thakur VC, Jayangondaperumal R. Paleoseismic evidences of grate surface rupture earthquakes along the Indian Himalaya. *J Geophys Res Solid Earth*. 2006;111(3):B03304.

    doi: 10.1029/2004JB003309

13. Sapkota SN, Bollinger L, Klinger Y, Tapponnier P, Gaudemer Y, Tiwari D. Primary surface ruptures of the great Himalayan earthquakes in 1934 and 1255. *Nat Geosci*. 2013;6(1):71-76.

    doi: 10.1038/ngeo1669

14. Bollinger L, Sapkota SN, Tapponnier P, *et al*. Estimating the return times of great Himalayan earthquakes in eastern Nepal: Evidence from the Patu and Bardibas strands of the Main Frontal Thrust. *J Geophys Res Solid Earth*. 2014;119(9):7123-7163.

    doi: 10.1002/2014JB010970

15. Scordilis EM. Empirical global relations converting MS and mb to moment magnitude. *J Seismol*. 2006;10(2):225-236.

    doi: 10.1007/s10950-006-9012-4

16. Tiwari RK, Paudyal H. Gorkha earthquake (MW7.8) and aftershock sequence: A fractal approach. *Earthq Sci*. 2022;35(3):193-204.

    doi: 10.1016/j.eqs.2022.06.001

17. Reddy DV, Nagabhushanam P, Kumar D, *et al*. The great 1950 Assam Earthquake revisited: Field evidences of liquefaction and search for paleoseismic events. *Tectonophysics*. 2009;474(3-4):463-472.

    doi: 10.1016/j.tecto.2009.04.024

18. Singh I, Pandey A, Mishra RL, *et al*. Evidence of the 1950 great assam earthquake surface break along the mishmi thrust at namche barwa himalayan syntaxis. *Geophys Res Lett*. 2021;48(11):1-9.

    doi: 10.1029/2020GL090893

19. Kaneda H, Nakata T, Tsutsumi H, *et al*. Surface rupture of the 2005 Kashmir, Pakistan, earthquake and its active tectonic implications. *Bull Seismol Soc Am*. 2008;98(2):521-557.

    doi: 10.1785/0120070073

20. Avouac JP, Ayoub F, Leprince S, Konca O, Helmberger DV. The 2005, Mw 7.6 Kashmir earthquake: Sub-pixel correlation of ASTER images and seismic waveforms analysis. *Earth Planet Sci Lett*. 2006;249(3-4):514-528.

    doi: 10.1016/j.epsl.2006.06.025

21. Avouac JP, Meng L, Wei S, Wang T, Ampuero JP. Lower edge of locked Main Himalayan Thrust unzipped by the 2015 Gorkha earthquake. *Nat Geosci*. 2015;8(9):708-711.

    doi: 10.1038/ngeo2518

22. Elliott JR, Jolivet R, Gonzalez PJ, *et al*. Himalayan megathrust geometry and relation to topography revealed by the Gorkha earthquake. *Nat Geosci*. 2016;9(2):174-180.

    doi: 10.1038/ngeo2623

23. Tiwari RK, Chaudhary S, Paudyal H, Shanker D. Identifying seismicity pattern before major earthquakes in the Western Nepal and adjoining region (28.5°N to 31.0°N - 78°E to 82.96°E). *Environ Earth Sci*. 2024;83(15):1-11.

    doi: 10.1007/s12665-024-11764-2

24. Diehl T, Singer J, Hetényi G, *et al*. Seismotectonics of Bhutan: Evidence for segmentation of the Eastern Himalayas and link to foreland deformation. *Earth Planet Sci Lett*. 2017;471:54-64.

    doi: 10.1016/j.epsl.2017.04.038

25. Sciences P, Sciences A, Hall P, Nazionale I, Murata V. *Seismic Fault Rheology and Earthquake Dynamics*. *Tecton Faults*. Massachusetts: Massachusetts Institute of Technology; 2018.

    doi: 10.7551/mitpress/6703.003.0007

26. Pudi R, Tapas RM, Vinod KK. Regional variation of stress level in the Himalayas after the 25 April 2015 Gorkha earthquake (Nepal) estimated using b-values. *J Geophys Eng*. 2018;15(3):921-927.

    doi: 10.1088/1742-2140/aaa26c

27. Bhatia SC, Kumar MR, Gupta HK. A probabilistic seismic hazard map of India and adjoining regions. *Ann di Geofis*. 1999;42(6):1153-1164.

    doi: 10.4401/ag-3777

28. Das S, Gupta ID, Gupta VK. A probabilistic seismic hazard analysis of Northeast India. *Earthq Spectra*. 2006;22(1):1-27.

    doi: 10.1193/1.2163914

29. Gutenberg B, Richter CFF. Frequency of earthquakes in California. *Bull Seismol Soc Am*. 1944;34:185-188.

    doi: 10.1038/156371a0

30. Okal EA, Romanowicz BA. On the variation of b-values with earthquake size. *Phys Earth Planet Inter*. 1994;87(1-2):55-76.

    doi: 10.1016/0031-9201(94)90021-3

31. Scholz CH. On the stress dependence of the earthquake b value. *Geophys Res Lett*. 2015;42(5):1399-1402.

    doi: 10.1002/2014GL062863

32. Wiemer S, Wyss M. Mapping spatial variability of the frequency-magnitude distribution of earthquakes. *Adv Geophys*. 2002;45(C):259-302.

    doi: 10.1016/S0065-2687(02)80007-3

33. Nakaya S. Spatiotemporal variation in b value within the subducting slab prior to the 2003 Tokachi-oki earthquake (M 8.0), Japan. *J Geophys Res Solid Earth*. 2006;111(3):3311.

    doi: 10.1029/2005JB003658

34. Sharma V, Bora DK, Biswas R. Spatio-temporal analysis of b-value prior to 28 April 2021 Assam Earthquake and implications thereof. *Ann Geophys*. 2022;65(5):SE534.

    doi: 10.4401/ag-8802

35. Tiwari RK, Paudyal H. Variability of b-value before and after the Gorkha earthquake in the Central Himalaya and Vicinity. *BIBECHANA*. 2021;18(2):32-42.

    doi: 10.3126/bibechana.v18i2.31207

36. Bondár I, Storchak D. Improved location procedures at the international seismological centre. *Geophys J Int*. 2011;186(3):1220-1244.

    doi: 10.1111/j.1365-246X.2011.05107.x

37. Willemann RJ, Storchak DA. Data collection at the international seismological centre. *Seismol Res Lett*. 2001; 72(4):440-453.

    doi: 10.1785/gssrl.72.4.440

38. Di Giacomo D, Robert Engdahl E, Storchak DA. The ISC-GEM Earthquake Catalogue (1904-2014): Status after the extension project. *Earth Syst Sci Data*. 2018;10(4):1877-1899.

    doi: 10.5194/essd-10-1877-2018

39. Reasenberg P. Second-order moment of central California seismicity, 1969-1982. *J Geophys Res Solid Earth*. 1985;90(B7):5479-5495.

    doi: 10.1029/jb090ib07p05479

40. Wiemer S, Wiemer. A software package to analyze seismicity: ZMAP. *Seismol Res Lett*. 2001;72(3):373-382.

    doi: 10.1785/gssrl.72.3.373

41. Aki K. Maximum likelihood estimate of b in the Gutenberg-Richter formula and its confidence limits. *Bull Earthq Res Inst*. 1965;43(43):237-239.

42. Utsu T. Aftershocks and earthquake statistics (III)- analyses of the distribution of earthquakes in magnitude, time, and space with special considertion to clustering characteristics of earthquake occurrence (1). *J Fac Sci Hokkaido Univ Ser VII*. 1971;3:379-441.

43. Shi Y, Bolt BA. The standard error of the magnitude-frequency b value. *Bull Seismol Soc Am*. 1982;72(5):1677-1687.

    doi: 10.1785/bssa0720051677

44. Tiwari RK, Paudyal H. Fractal characteristics of the seismic swarm succeeding the 2015 Gorkha Earthquake, Nepal. *Indian Geotech J*. 2023;53(4):789-804.

    doi: 10.1007/s40098-022-00704-1

45. Aswini KK, Kamesh Raju KA, Dewangan P, Yatheesh V, Singha P, Ramakrushana Reddy T. Seismotectonic evaluation of off Nicobar Earthquake Swarms, Andaman Sea. *J Asian Earth Sci*. 2021;221:104948.

    doi: 10.1016/j.jseaes.2021.104948

46. Oncel AO, Wilson T. Space-time correlations of seismotectonic parameters: Examples from Japan and from Turkey preceding the İzmit earthquake. *Bull Seismol Soc Am*. 2002;92(1):339-349.

    doi: 10.1785/0120000844

47. Babu VG, Kumar N, Verma SK, Pal SK. An updated earthquake catalogue and seismic regimes in the northwest Himalaya: Seismic periodicity associated with strong earthquakes. *J Earth Syst Sci*. 2023;132(4):173.

    doi: 10.1007/s12040-023-02180-4

48. Khan PK, Mohanty SP, Sinha S, Singh D. Occurrences of large-magnitude earthquakes in the Kachchh region, Gujarat, western India: Tectonic implications. *Tectonophysics*. 2016;679:102-116.

    doi: 10.1016/j.tecto.2016.04.044

49. Chetia M, Gogoi PR, Lahiri SK. Temporal variation of seismic b-value in the Himalayas and foreland region and its implications on crustal stress variability. *Acta Geophys*. 2023;71(4):1675-1692.

    doi: 10.1007/s11600-022-00999-x

50. Tiwari RK, Paudyal H. Analysis of the b, p values, and the fractal dimension of aftershocks sequences following two major earthquakes in central Himalaya. *Heliyon*. 2024;10(2):e24476.

    doi: 10.1016/j.heliyon.2024.e24476

51. Molnar P, Lyon-Caent H. Fault plane solutions of earthquakes and active tectonics of the Tibetan Plateau and its margins. *Geophys J Int*. 1989;99(1):123-154.

    doi: 10.1111/j.1365-246X.1989.tb02020.x

52. Tiwari RK, Paudyal H. Spatial mapping of b-value and fractal dimension prior to November 8, 2022 Doti Earthquake, Nepal. *PLoS One*. 2023;18:e0289673.

    doi: 10.1371/journal.pone.0289673

53. Kumar S, Sharma N. The seismicity of central and north-east Himalayan region. *Contrib Geophys Geodes*. 2019;49(3):265-281.

    doi: 10.2478/congeo-2019-0014

54. Pathak V, Pant C, Joshi S. Source Parameter and b-Value Estimation of Local Earthquakes in Kumaun Region, Central Himalaya, India. *Int J Adv Res*. 2016;4(9):15254-1266.

doi: 10.21474/ijar01/1609

55. Yadav RBS, Bormann P, Rastogi BK, Das MC, Chopra S. A homogeneous and complete earthquake catalog for northeast India and the adjoining region. *Seismol Res Lett*. 2009;80(4):609-627.

doi: 10.1785/gssrl.80.4.609

56. Rajendran K, Parameswaran RM, Rajendran CP. Revisiting the 1991 Uttarkashi and the 1999 Chamoli, India, earthquakes: Implications of rupture mechanisms in the central Himalaya. *J Asian Earth Sci*. 2018;162:107-120.

doi: 10.1016/j.jseaes.2018.04.012

57. Tiwari A, Paul A, Singh R, Upadhyay R. Potential seismogenic asperities in the Garhwal-Kumaun region, NW Himalaya: Seismotectonic implications. *Nat Hazards*. 2021;107(1):73-95.

doi: 10.1007/s11069-021-04574-3

58. Yadav RBS, Koravos GC, Tsapanos TM, Vougiouka GE. A probabilistic estimate of the most perceptible earthquake magnitudes in the NW Himalaya and Adjoining Regions. *Pure Appl Geophys*. 2015;172(2):197-212.

doi: 10.1007/s00024-014-0864-1

59. Gunti S, Roy P, Narendran J, *et al*. Assessment of geodetic strain and stress variations in Nepal due to 25 April 2015 Gorkha earthquake: Insights from the GNSS data analysis and b-value. *Geod Geodyn*. 2022;13(3):288-300.

doi: 10.1016/j.geog.2022.01.003

60. Hajra S, Hazarika D, Shukla V, Kundu A, Pant CC. Stress dissipation and seismic potential in the central seismic gap of the north-west Himalaya. *J Asian Earth Sci*. 2022;239:105432.

doi: 10.1016/j.jseaes.2022.105432

61. Prasath RA, Paul A, Singh S. Earthquakes in the garhwal himalaya of the central seismic gap: A study of historical and present seismicity and their implications to the seismotectonics. *Pure Appl Geophys*. 2019;176(11):4661-4685.

doi: 10.1007/s00024-019-02239-8

62. Sreejith KM, Sunil PS, Agrawal R, Saji AP, Rajawat AS, Ramesh DS. Audit of stored strain energy and extent of future earthquake rupture in central Himalaya. *Sci Rep*. 2018;8(1):1-9.

doi: 10.1038/s41598-018-35025-y

63. Rajendran K, Parameswaran RM, Rajendran CP. Seismotectonic perspectives on the Himalayan arc and contiguous areas: Inferences from past and recent earthquakes. *Earth-Science Rev*. 2017;173:1-30.

doi: 10.1016/j.earscirev.2017.08.003

ACCSCIENCE PUBLISHING

Journal of Seismic Exploration

ARTICLE

Seismic reflection modeling of an atoll: A comparison between pre- and post-stack migration sections

Şerife Boğazkesen[1]* and Hakan Karslı[2]

[1]Department of Civil Engineering, Faculty of Engineering, Atatürk University, Erzurum, Turkey

[2]Department of Geophysics Engineering, Faculty of Engineering, Karadeniz Technical University, Trabzon, Turkey

Abstract

Atoll structures formed in complex geological settings act as stratigraphic hydrocarbon traps and are typically circular or elliptical reef structures with a large lagoon at the center. Initially, the circular reef with flat limestone serves as a potential reservoir rock and holds significant importance in the petroleum industry, as it forms hydrocarbon-bearing traps. Therefore, identifying these structures in seismic sections is crucial. To understand the seismic behavior of atoll structures, seismic shot gathers of a geological model were generated, and migration sections were obtained. In this study, artificial data modeling of an atoll structure containing oil traps was carried out using the two-dimensional acoustic finite difference method due to its practicality and the flexibility to select different trap models as needed. Seismic data modeling was performed in a pre-stack shot domain, and two different data processing stages were applied to the shot data to obtain pre-stack and post-stack Kirchhoff time migration sections. The spatial location and size of hydrocarbon traps in the migration sections were determined and compared with the initial atoll model. In this way, the seismic response of hydrocarbon trap structures in the atoll model was analyzed. The importance of the two different data processing methods was also examined. As a result, it was observed that the pre-stack Kirchhoff time migration method provides better results than the post-stack time migration method for the atoll model.

Keywords: Atoll; Acoustic finite difference method; Pre- and post-stack Kirchhoff time migration

***Corresponding author:**
Şerife Boğazkesen
(serifebogazkesen@atauni.edu.tr)

Citation: Boğazkesen Ş, Karslı H. Seismic reflection modeling of an atoll: A comparison between pre- and post-stack migration sections. *J Seismic Explor.* 2025;34(1): 12-21.
doi: 10.36922/JSE025190001

Received: May 8, 2025

1st revised: June 30, 2025

2nd revised: July 03, 2025

3rd revised: July 17, 2025

4th revised: July 18, 2025

Accepted: July 20, 2025

Published online: July 30, 2025

1. Introduction

Atoll structures containing hydrocarbons are associated with the development within carbonate platforms characterized by high porosity and permeability, which are effective stratigraphic traps when overlain by impermeable cover rocks. Atolls can become effective hydrocarbon traps when underlain by units such as claystone, marl, or volcanic tuff, which possess low permeability. In addition, these structures offer significant reservoir potential due to their high porosity, a result of biogenic processes. However, atoll-type traps often represent complex systems that require multifaceted assessment, as they combine both structural and stratigraphic elements in the petroleum systems'

trapping mechanisms. Therefore, detailed analysis of parameters such as paleoclimate, sea-level changes, and tectonic regimes plays a critical role in determining the hydrocarbon potential of atoll traps.[1-5] As such, the identification and exploration of these traps require intensive and methodical studies supported by advanced data acquisition, processing, and interpretation techniques, alongside sophisticated geological and reservoir modeling approaches. Concurrently, studies incorporating advanced mechanical techniques are being conducted to more robustly define hydrocarbon reservoir properties and increase productivity.[6-10]

Seismic reflection methods used to study atoll structures with hydrocarbon traps involve collecting field data using multi-source and multi-receiver systems, followed by processing and interpretation using modern, purpose-built software. The interpretation process enables accurate identification of structures and hydrocarbon traps by incorporating both structural and compositional information. However, understanding the general seismic response of atoll structures can help prevent misinterpretations during seismic section analysis. Moreover, the complex geological environments hosting these traps, along with potential oversights during data processing or errors in parameter selection, are recognized as factors that may degrade the quality of seismic sections used for interpretation. The seismic reflection behavior of atoll structures is typically analyzed through numerical modeling of acoustic seismic wave propagation within a defined realistic subsurface model, a process referred to as seismic modeling.[11-14] Seismic modeling has been widely used both to design optimal seismic data acquisition strategies[15-17] and to improve seismic data processing workflows. In this context, the complex geometry of atoll structures and illumination problems during seismic interpretation have been investigated.[18-20]

Although various numerical methods, such as ray tracing, finite difference, and finite element techniques, have been used for wave propagation modeling of atoll structures, each with its advantages and limitations, the finite difference method (FDM) can provide successful results in highly complex environments. FDM is extensively utilized in seismic forward modeling studies due to its ability to accommodate diverse structural models without significant constraints.[21-30] The solution of seismic wave propagation problems using FDM has received considerable attention in recent years.[31-33] This approach offers an effective numerical solution to wave equations, enabling comprehensive wavefield modeling and incorporating all wave types, including reflections, scatterings, multiples, and surface waves.

Abuamarah *et al.*[34] identified an atoll structure offshore of North Damietta in the Mediterranean Sea using a 3D seismic reflection method and well drilling information. Their analysis revealed that the atoll structure contains significant gas accumulations. Huang *et al.*[35] acquired 2D multichannel seismic reflection data to investigate the stratigraphy, geomorphology, depositional processes, and seismic facies of Zhongshan Atoll in the South China Sea – the largest atoll in the world. Analysis of the acquired data revealed seismic anomalies resembling fluid flow features concentrated in the Late Oligocene–Early Miocene platform areas, and associated with pre-Miocene faults. They suggested that these fluid features may indicate gas-bearing atoll structures.[36,37]

This study aims to utilize the FDM to simulate shot records for an atoll subsurface model, which may represent a complex hydrocarbon trap. In addition, it seeks to generate pre-stack and post-stack Kirchhoff time migration sections by applying two distinct data processing workflows. To achieve this, artificial shot gathers were generated using Matlab-based software developed by Youzwishen and Margrave.[38] The simulated shot data were then processed with ProMAX software to produce pre-stack and post-stack Kirchhoff time migration sections. The seismic signatures of the atoll trap were analyzed on the resulting zero-offset sections, and the alignment of reflection events with the geological model was evaluated.

2. Methodology

2.1. Acoustic FDM

Seismic wavefield modeling illustrates how seismic waves propagate through a subsurface model. To date, there is no exact analytical solution for calculating these wavefields in arbitrary media. As a result, several approximation techniques have been developed over time to solve the specific wave equation.[12,39] One method is the FDM, which is effective for use in arbitrary media. In this method, the medium is divided into a grid with sufficient resolution to accurately simulate the propagation of elastic waves. Variations in elastic parameters at each grid point are calculated at specific time intervals to simulate seismic wave propagation within the gridded model. Forces applied at designated locations within the model activate corresponding grid points, initiating wave propagation. These forces, which are independent in both spatial and temporal domains, serve as representations of seismic sources. At any grid point and time, different elastic properties can be evaluated, providing insights into the seismic response observed at surface receivers or within boreholes. FDM computes the entire wavefield and inherently accounts for surface waves. Its routine

application has only recently become feasible due to significant advancements in computational power.

The FDM software utilized in this study is described by Bohlen.[40] The code, known as Seismic mOdeling with FInite differences called SOFI, is based on the foundational work of Virieux[22] and Levander[41] for elastic wave simulation, along with contributions from Robertsson *et al.*[27] for viscoelastic modeling. The software incorporates intrinsic wave absorption viscoelasticity (Q). It also provides an alternative rotated-grid representation of the subsurface, based on the work of Gold *et al.*[42] and Saenger *et al.*,[43] to improve the accuracy of surface wave simulations. The simulation accounts for both wave absorption, typical in unconsolidated near-surface rock units, and surface waves, which can complicate near-surface seismic data processing. This approach facilitates a clearer differentiation of subsurface parameters that influence the characteristics of seismic field data.

2.2. Application

The atoll model, a stratigraphic trap, is an important tectonic structure in oil and gas geology.[44] Atolls are large, circular or elliptical reefs with a central lagoon. Initially, the circular reef, composed of flat limestone, serves as a potential reservoir rock, whereas the lagoonal micrite limestone typically does not. However, a reversal in porosity over time can change this. Atolls can form giant hydrocarbon fields, yet their structural complexity often makes identification and characterization on seismic sections challenging.

The source function, along with the spatial and temporal calculation parameters used in the atoll modeling, is provided in Table 1. For the modeling process, reflective interfaces were digitized, and depth, distance, and velocity information were input into the modeling software. Significant effort was made to ensure that the geological models accurately represent realistic and complex subsurface environments. Given that variations in layer density are minimal compared to seismic wave velocity, the density was assumed to be constant (ρ = 2.0 g/cm^3).

Figure 1 shows the atoll model in a multilayer environment. The model includes two hydrocarbon traps composed of gaseous sand with an average seismic wave velocity of 1200 m/s in the 550 – 690 m depth range. From top to bottom, the model is stratified as follows: wet sand with a velocity of 1800 m/s between 0 m and 210 m, saturated shale with a velocity of 2300 m/s between 210 m and 490 m, porous sandstone with a velocity of 2400 m/s between 490 m and 680 m, and marl with a velocity of 2600 m/s between 680 m and 750 m. At the center, the model features an impermeable lagoon-like micritic limestone with a velocity of 3500 m/s between 690 m and 900 m, flanked on both sides by porous and permeable sandstone (the reservoir rock) with a velocity of 2500 m/s between 750 m and 900 m. The base of the model consists of basalt with a velocity of 2800 m/s between 900 m and 1000 m.

Table 1. Parameters used for atoll modeling

Modeling parameters	Atoll model
Profile length	2000 m
Maximum depth	1000 m
Receiver interval	10 m
Shot interval	40 m
Number of shots	25
Number of receivers	201
Maximum velocity	4000 m/s
Minimum velocity	2000 m/s
Maximum offset	2000 m
Minimum offset	100 m
Calculation time step	0.02 ms
Sampling time	4 ms
Record length	1000 ms
Minimum phase Ricker source wavelet	30 Hz

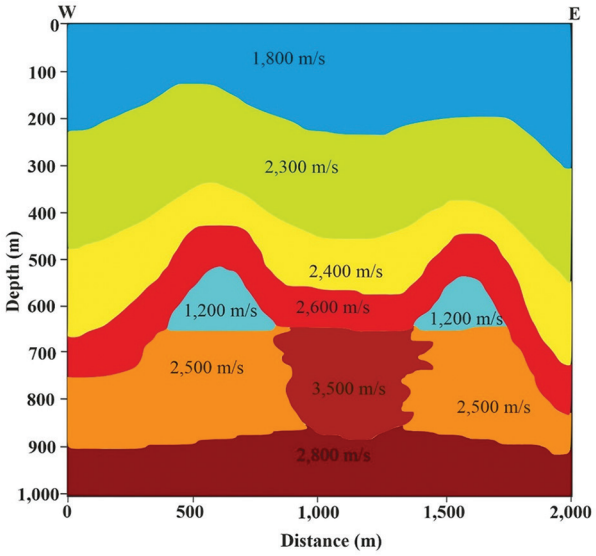

Figure 1. Input model P-wave velocity for Atoll model[44]

2.3. Synthetic seismic data and processing

A total of 25 synthetic shot gathers were generated from multiple shots at regular intervals using a multi-shot and fixed-array receiver setup. For each shot, 100 seismic traces corresponding to 100 receivers were recorded. The synthetic

shot gathers contain various noise components such as scattering, multiple reflections, and first arrivals. Moreover, the reflection events originating from each layer exhibit hyperbolic geometries that do not accurately represent the geometry of the actual reflecting structures. However, the complex nature of the subsurface environment, including its absorptive properties, heterogeneity, and sloping or topographical surface features, has significantly distorted the waveforms of reflections recorded at the surface. Due to subsurface inhomogeneity, the expected reflection events between the source and the receiver often do not occur in a direct path, leading to incorrect interpretation of reflective geometries in the shot gathers. To address these challenges, various data processing steps were applied, using appropriate processing workflows and correct parameter selections. Multichannel synthetic seismic reflection data were processed using Landmark Graphics Co.'s ProMAX 2D software (USA). Pre- and post-stack Kirchhoff time migration sections were obtained by removing noise from the shot gathered in the synthetic seismic reflection data and enhancing the primary reflections. The image quality of both migration sections was analyzed. The data processing workflows used for generating post- and pre-stack Kirchhoff time migration sections are shown in Figure 2.

2.4. Post-stack Kirchhoff time migration

The 25 synthetic shot gathers obtained from the atoll model were processed according to the data processing workflow for post-stack Kirchhoff time migration section shown in Figure 2. First, the data were loaded, and the geometric information was defined. Then, first-arrival wavefields

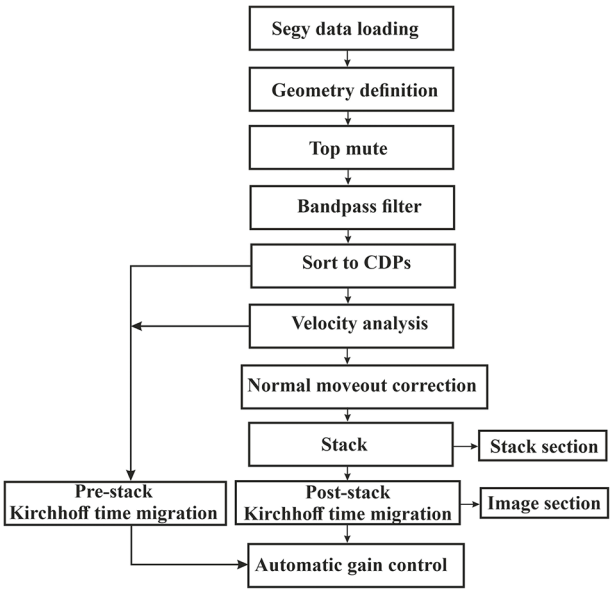

Figure 2. Seismic data processing flow chart (modified from Dondurur[45])

(direct and refracted waves) were removed using a top mute. Proper muting of these first arrivals prevents visible enclosures in the semblance contours during velocity analysis. This step improved the image quality of the resulting migration section. Linear undesirable events (e.g., diffracted waves) were also observed in the shot gathers. To address this, a coherence filter was applied to filter out these linear events and other unwanted features such as edge reflections. During coherence filtering, seismic data are transformed from the time–distance (t–x) domain to the frequency–wavenumber (f–k) domain using a Fourier transform. Linear undesired events are identified and filtered based on their slope direction. Filtering was performed using the frequency and velocity information of the linear unwanted events, which were determined to be 2000 m/s and 20 – 60 Hz, respectively. Although the model shot gathers do not contain low-frequency surface waves or high-frequency noise, modeling artifacts may still occur. To filter out these noises and preserve the useful spectral band of the data, a bandpass filter with cutoff frequencies of (10, 15, 55, 65) Hz was applied. These cutoff frequencies were selected by analyzing the spectral content of the data to identify the range of usable frequencies. For this purpose, the first shot was compared before (Figure 3A and 3B) and after (Figure 3C and 3D) bandpass filtering. The chosen filter's cutoff frequencies are indicated in the Fourier mean amplitude spectrum in Figure 3B. Clearly, the small-amplitude, high-frequency noise in the post-filtered shot gather (Figure 3C) is attenuated, resulting in an overall increase in the signal-to-noise ratio of the data and, in particular, a strengthening of the reflection phenomena (Figure 3C).

Velocity spectrum calculation was performed every 20 common midpoints (CMPs). The root mean square velocities were applied to the CMP groups to obtain normal moveout time (NMO) corrected CMP gathers. At this stage, the velocity function of each CMP was combined to create the velocity field for the migration process to be applied in the next stage. However, to remove the stretching artifacts caused by the NMO correction, a 60% NMO top mute was applied, and a stacked section was obtained. Post-stack Kirchhoff time migration was then applied to the stacked data. For imaging purposes, the window length was chosen as one-fourth of the total data recording time, and automatic gain control was applied.

2.5. Pre-stack Kirchhoff time migration

The same initial data processing steps and parameter selections used for the post-stack Kirchhoff time migration section were also applied to obtain the pre-stack Kirchhoff time migration section. The artificial shot gathers were processed normally until the common depth point gathers

were produced. Then, velocity analysis was performed on the CMPs to construct the velocity field. Unlike the post-stack method, the pre-stack migration section was obtained without applying NMO correction and stacking stages.

3. Results and discussion

To understand the complex behavior of a hydrocarbon-bearing atoll trap in seismic reflection data, zero-offset stacking and migration sections were obtained from seismic shot gathers containing only P-waves. The level of agreement between the initial geological atoll model designed for simulation and the resulting stack and migration sections was assessed, and the causes of any discrepancies were examined. The atoll depth-velocity model, the post-stack Kirchhoff time migration section, and the stack obtained from this velocity model are presented in Figure 4A-C. Overall, a good degree of similarity is observed. In the post-stack Kirchhoff time migration process, the maximum frequency was 50 Hz, and the maximum slope was 50°, based on the data characteristics. The aperture

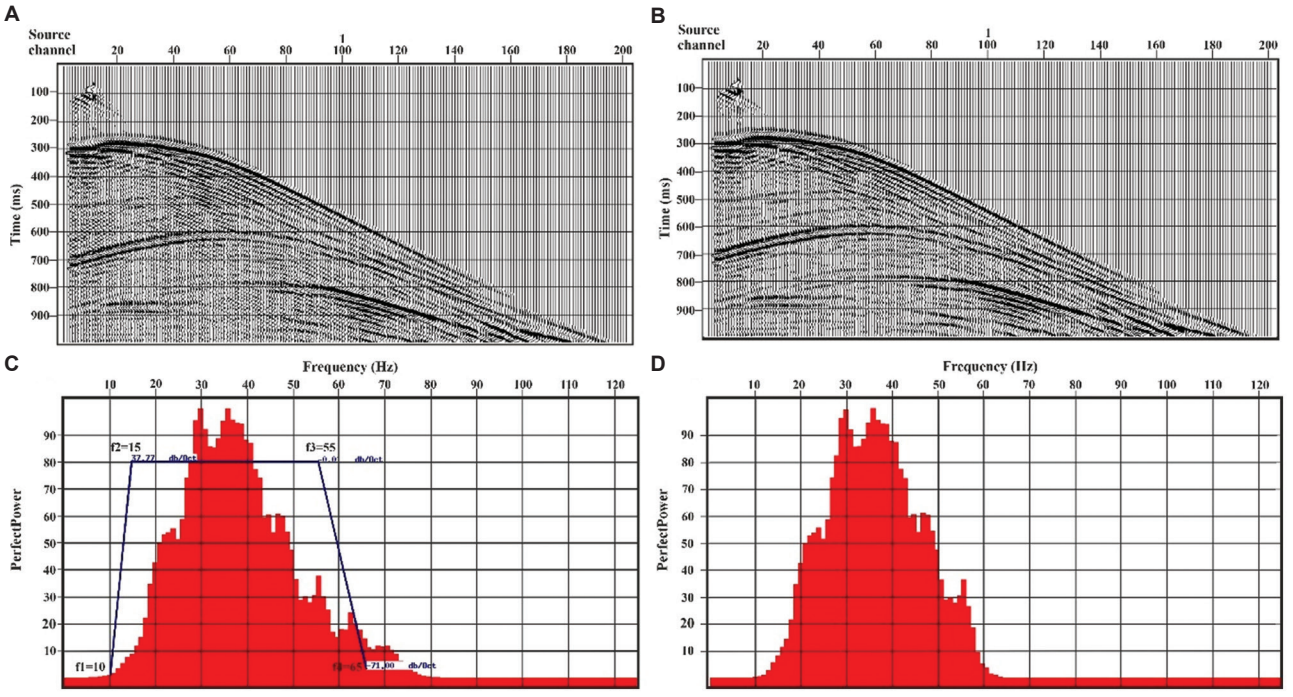

Figure 3. Comparison of the first shot recording from the atoll model before and after the bandpass filter. Unfiltered and filtered (A and B) shot records and (C and D) Fourier mean amplitude spectra

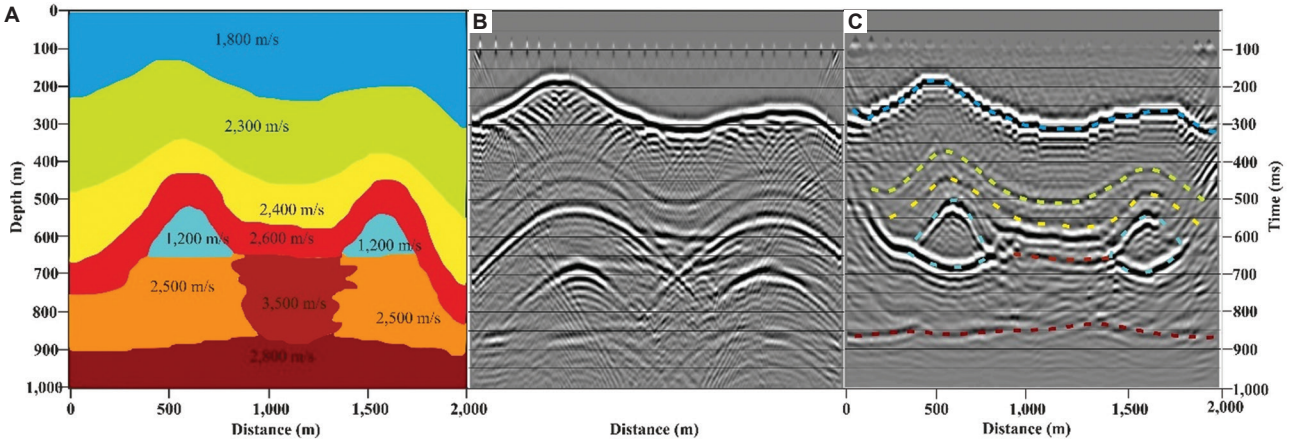

Figure 4. Comparison of (A) the velocity model based on the atoll trap depth, (B) the stacked section, and (C) the post-stack Kirchhoff time migration section

value was set to zero to increase the migration speed and minimize distortion of the data. An f–k filter was applied to enhance signal-to-noise discrimination in the post-stack Kirchhoff migration section. Although some signal and noise components share similar frequency characteristics, they can be differentiated based on their velocity (or dip) properties. In Figure 5A, the components to be removed from the data were selectively identified on the f–k spectrum shown in Figure 5B. Consequently, as highlighted by Karslı[46], unnecessary data losses and discontinuity effects were minimized. A comparison between Figure 5C and 5D reveals that noise was significantly attenuated following the application of f–k filtering.

The pre-stack Kirchhoff time migration method was employed to analyze the atoll trap model, which features a structurally complex geological framework. To generate the pre-stack Kirchhoff time migration section, 190 offset sections were created, ranging from a near offset of 5 m to a far offset of 1905 m, with spacing determined by the receiver configuration. The velocity model was iteratively refined by migrating each common-offset section. Amplitude variation with offset analysis was conducted using CMP gathers, leading to an enhanced migrated stacked section. Consequently, brute stack data were generated as part of the pre-stack time migration workflow. This process enabled the approximate spatial positions of the trap structure and associated layered features within the initial atoll model to be accurately delineated in the pre-stack Kirchhoff time migration section, as opposed to the post-stack Kirchhoff time migration method (Figure 6). In the depth-transformed migration section, reflective interfaces corresponding to strata depths of 210 m, 490 m, and 680 m were imaged with continuity and clarity. In addition, two distinct atoll structures were prominently identified within the depth range of 510 – 680 m. In the pre-stack Kirchhoff time migration section, lateral reflections observed at 200 ms, 310 ms, 450 ms, 510 ms, and 610 ms are indicative of layer interfaces, providing detailed stratigraphic and structural insights. In addition, between 690 m and 900 m,

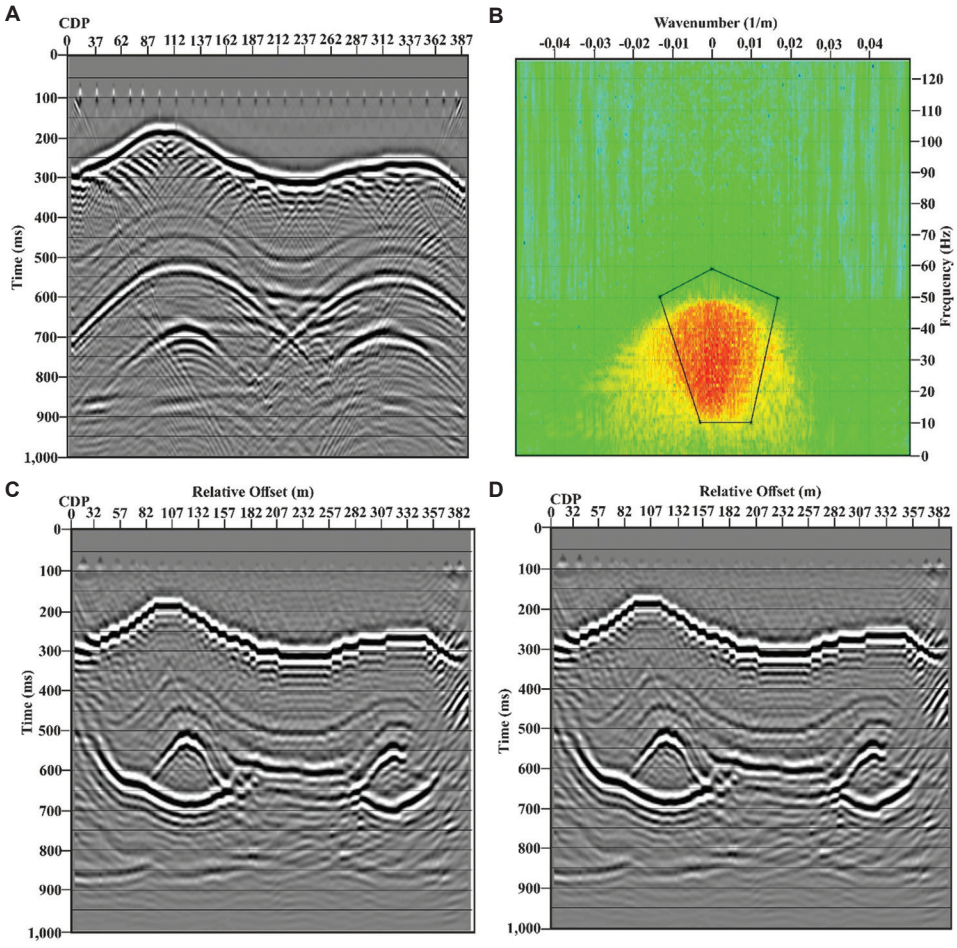

Figure 5. Comparison of sections and frequency–wavenumber (f–k) filtering application. (A) Stacked section, (B) f–k spectrum, (C) post-stack Kirchhoff time migration section before f–k filtering, and (D) post-stack Kirchhoff time migration section after f–k filtering

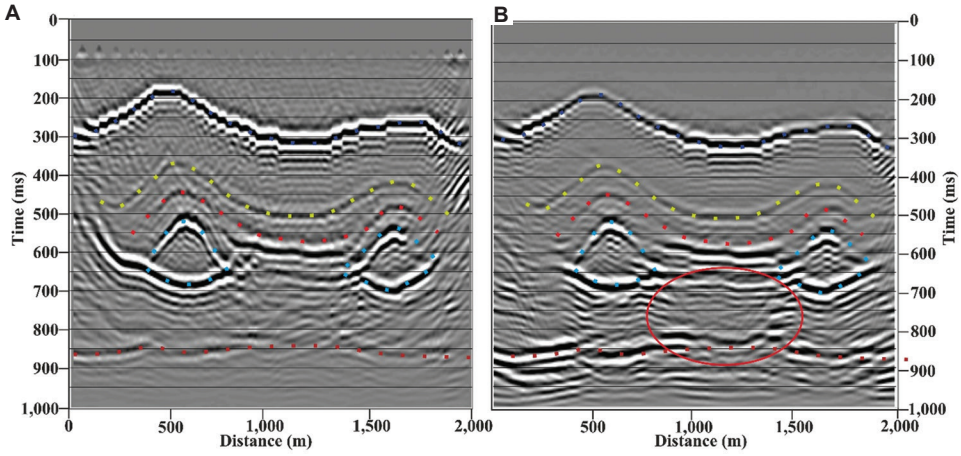

Figure 6. Comparison of (A) the post-stack Kirchhoff time migration section of the atoll trap model and (B) the pre-stack Kirchhoff time migration section

an impermeable lagoon-like micrite limestone unit with a mid-velocity of 3500 m/s changes the reflection character due to the velocity contrast with the surrounding rocks. The boundaries of this unit in the seismic section (indicated by a red elliptical line) are clearly defined by the reflections occurring in these regions.

The post-stack Kirchhoff time migration section shown in Figure 6A was obtained using the mean velocity model, which provides limited resolution for identifying complex geologic structures. Consequently, the boundaries of the impermeable lagoon-like structure, with a velocity of 3500 m/s in the middle section at depths of 690 – 900 m, could not be visualized clearly. On the other hand, the pre-stack Kirchhoff time migration section presented in Figure 6B was processed separately before stacking, resulting in a more accurate velocity model. This improved image quality allowed the upper boundaries of both the lagoon-like geological structure and the basalt unit, with a velocity of 2800 m/s, to be clearly defined within the 900 – 1,000 m depth range. Dong and Yang[47] constructed a seismic velocity model of the crust surrounding the epicenter of the 2023 Jishishan earthquake using full waveform tomography. Their results indicate that the epicenter is located within a transitional zone characterized by significant variations in seismic properties. The model reveals prominent low-velocity zones in the mid-to-lower crust beneath the interior of the plateau, whereas high-velocity anomalies are observed along the plateau margins.

4. Conclusion

In this paper, the shot-domain seismic reflection responses of the atoll structure containing hydrocarbon traps formed in complex geologic environments were calculated using the acoustic FDM technique, which provides a full wavefield solution. The shot data were processed with two different data processing flows to visualize the initial ground model and hydrocarbon traps. According to the modeling study, when the migration sections obtained from the pre- and post-stack time migration methods are compared, the approximate real spatial locations of the stratified structure, reflector topographies, and trap structures in the initial ground model can be identified in agreement with the migration sections. It has been observed that the pre-stack migration process improves the seismic section resolution where lateral velocity variations are present and offers a much clearer definition. Accordingly, the pre-stack migration method, used in conjunction with the acoustic FDM technique, which provides a full wavefield solution, allows for more reliable imaging of complex subsurface structures through shot domain-generated artificial seismic data, thereby increasing the accuracy and reliability of geophysical interpretations.

Quantitatively, the pre-stack migration sections demonstrated an average improvement of approximately 20 – 30% in lateral and vertical resolution compared to the post-stack results, particularly in areas exhibiting significant velocity heterogeneities. This enhancement substantially contributes to the precise delineation of hydrocarbon trap boundaries and reflector geometries in complex subsurface conditions.

Acknowledgments

The Department of Geophysical Engineering at Karadeniz Technical University conducted academic research and analysis to process the computed shot records. Matlab code for finite difference modeling from the CREWES project, which is available free of charge at http://www.crewes.ucalgary.ca/, was used in this study. In addition, ProMAX software from Landmark Graphics Co. (USA), provided through the generosity of Halliburton (USA), was also utilized.

Funding

None.

Conflict of interest

The authors declare that they have no conflicts of interest.

Author contributions

Conceptualization: Şerife Boğazkesen
Data curation: Şerife Boğazkesen
Formal analysis: Şerife Boğazkesen
Investigation: Şerife Boğazkesen
Methodology: Şerife Boğazkesen
Supervision: Hakan Karslı
Visualization: Şerife Boğazkesen
Writing–original draft: Şerife Boğazkesen
Writing–review & editing: Hakan Karslı

Availability of data

The data supporting this study are available from the corresponding author upon reasonable request (serifebogazkesen@atauni.edu.tr).

References

1. Schlager W. *Carbonate Sedimentology and Sequence Stratigraphy*. Oklahoma: SEPM (Society for Sedimentary Geology), Concepts in Sedimentology and Paleontology; 2005.
2. Wang P, Li Q, Li CF. Geology of the China seas. In: *Developments in Marine Geolog*. Amsterdam: Elsevier; 2014.
3. Wu S, Zhang X, Yang Z, Wu T, Gao J, Wang D. Spatial and temporal evolution of Cenozoic carbonate platforms on the continental margins of the South China Sea: Response to opening of the ocean basin. *Interpretation*. 2016;4(3):1-19.

   doi: 10.1190/INT-2015-0162.1
4. Garcia GG, Henriques MH, Garcia AJV, Dantas MVS. Petrofacies and taphofacies analyses of coquinas as a tool for the establishment of a stratigraphic evolution model of the morro do chaves formation (SergipeAlagoas Basin, NE Brazil). *Facies*. 2021;67:4.

   doi: 10.1007/s10347-020-00614-9
5. Zhu X, Jia G, Tian Y, *et al*. Ancient hydrocarbon slicks recorded by a coral atoll in the South China Sea. *Chem Geol*. 2023;619:121316.

   doi: 10.1016/j.chemgeo.2023.121316
6. Cao D, Zeng L, Gomez-Rivas E, *et al*. Correction of linear fracture density and error analysis using underground borehole data. *J Struct Geol*. 2024;184:105152.

   doi: 10.1016/j.jsg.2024.105152
7. Li Y, Jia D, Wang S, Qu R, Qiao M, Liu H. Surrogate model for reservoir performance prediction with time-varying well control based on depth generative network. *Petrol Explor Dev*. 2024;51(5),1287-1300.

   doi: 10.1016/S1876-3804(25)60541-6
8. Niu Q, Hu M, Chang J, *et al*. Explosive fracturing fechanism in low-permeability sandstone-type uranium deposits considering different acidification reactions. *Energy*. 2024;312:133676.

   doi: 10.1016/j.energy.2024.133676
9. Zhang L, Yuan X, Luo L, Tian Y, Zeng S. Seepage characteristics of broken carbonaceous shale under cyclic loading and unloading conditions. *Energy Fuels*. 2024;38(2):1192-1203.

   doi: 10.1021/acs.energyfuels.3c04160
10. Deng R, Dong J, Dang L. Numerical simulation and evaluation of residual oil saturation in waterflooded reservoirs. *Fuel*. 2025;384:134018.

    doi: 10.1016/j.fuel.2024.134018
11. Fagin SW. Seismic modeling of geologic structures: Applications to exploration problems. In: *Geophysical Development Series*. United States: Society of Exploration Geophysicists; 1991.

    doi: 10.1190/1.9781560802754
12. Carcione JM, Herman GC, Kroode APE. Seismic modeling. *Geophysics*. 2002;67(4):1304-1325.

    doi: 10.1190/1.1500393
13. Krebes ES. Seismic forward modeling. *CSEG Record*. 2004;30:28-39.
14. Sayers CM, Chopra S. Introduction to this special section: Seismic modeling. *Lead Edge*. 2009;28:528-529.

    doi: 10.1190/1.3124926
15. Gjøystdal H, Iversen E, Lecomte I, Kaschwich T, Drottning A, Mispel J. Improved applicability of ray tracing in seismic acquisition, imaging, and interpretation. *Geophysics*. 2007;72(5):261-271.

    doi: 10.1190/1.2736515
16. Regone CJ. Using finite-difference modeling to design wide-azimuth surveys for improved subsalt imaging. *Geophysics*. 2007;72(5):31-239.

    doi: 10.1190/1.2668602
17. Fu L, Guo J, Shen W, *et al*. Geophysical evidence of the collisional suture zone in the prydz bay, East Antarctica. *Geophys Res Lett*. 2024;51(2):e2023GL106229.

    doi: 10.1029/2023GL106229
18. Albertin U, Woodward M, Kapoor J, *et al*. Depth imaging examples and methodology in the Gulf of Mexico. *Lead Edge*. 2001;20(5):449-560.

doi: 10.1190/1.1438980

19. Ray A, Pfau G, Chen R. Importance of ray-trace modeling in the discovery of the thunder horse North filed, gulf of Mexico. *Lead Edge*. 2004;23(1):1-88.

doi: 10.1190/1.1645457

20. Seitchick A, Jurick D, Bridge A, *et al*. The tempest project addressing challenges in deepwater gulf of Mexico depth imaging through geologic models and numerical simulation. *Lead Edge*. 2009;28:546-553.

doi: 10.1190/1.3124929

21. Kelly KR, Ward RW, Treitel S, Alford RM. Synthetic seismograms: A finite-difference approach. *Geophysics*. 1976;41(1):2-27.

doi: 10.1190/1.1440605

22. Virieux J. P-SV wave propagation in heterogeneous media: Velocity-stress finite-difference method. *Geophysics*. 1986;51(4):1933-1942.

doi: 10.1190/1.1441605

23. Igel H, Mora P, Riollet B. Anistotropic wave propagation through finite-difference grids. *Geophysics*. 1995;60(4):939-1278.

doi: 10.1190/1.1443849

24. Etgen J, O'Brien MJ. Computational methods for large-scale 3D acoustic finite-difference modeling. *Geophysics*. 2007;72(5):223-230.

doi: 10.1190/1.2753753

25. Bansal R, Sen MK. Finite-difference modeling of S-wave splitting in anisotropic media. *Geophys Prospect*. 2008;56:293-312.

doi: 10.1111/j.1365-2478.2007.00693.x

26. Liu Y, Sen MK, Jackson K. Advanced finite-difference methods for seismic modeling. *Geohorizons*. 2009:5-16.

27. Robertsson JOA, Van Manen DJ, Schmelzbach C, Renterghem CV, Amudsen L. Finite-difference modelling of wavefield constituents. *EAGE*. 2016;203:1334-1342.

doi: 10.3997/2214-4609.201601176

28. Talukdar K, Behere L. Sub-basalt ımaging of hydrocarbon-bearing mesozoic sediments using ray-trace ınversion of first-arrival seismic data and elastic finite-difference full-wave modeling along sinor-valod profile of deccan syneclise, India. *Pure Appl Geophys*. 2018;175:2931-2954.

doi: 10.1007/s00024-018-1831-z

29. Boğazkesen Ş, Karslı H. Modeling of the complex hydrocarbon traps by the shot domain acoustic finite difference method and data-processing. *Bull Min Res Explor*. 2022;168:93-109.

doi: 10.19111/bulletinofmre.985502

30. Boğazkesen Ş, Karslı H. Seismic modeling of complex hydrocarbon traps in shot domain and data processing to obtain stack-migration sections. *Petrol Sci Technol*. 2025:1-19.

doi: 10.1080/10916466.2025.2477658

31. Alterman Z, Karal FC Jr. Propagation of elastic waves in layered media by finite- difference methods. *Bull Seismol Soc Am*. 1968;58(1):367-398.

doi: 10.1785/BSSA0580010367

32. Boore DM. *Finite-Difference Solutions to the Equations of Elastic Wave Propagation, with Application to Love Waves Over Dipping Interfaces*. PhD Diss, M.I.T.Claerbout; 1970. Available from: https://hdl.handle.net/1721.1/50287 [Last accessed on 2025 Apr 14].

33. Ottaviani M. Elastic-wave propagation in two evenly welded quarter-spaces. *Bull Seismol Soc Am*. 1971; 61(5):1119-1152.

doi: 10.1785/BSSA0610051119

34. Abuamarah BA, Nabawy BS, Shehata AM, Kassem OMK, Ghrefat H. Integrated geological and petrophysical characterization of oligocene deep marine unconventional poor to tight sandstone gas reservoir. *Marine Petrol Geol*. 2019;109:868-885.

doi: 10.1016/j.marpetgeo.2019.06.037

35. Huang X, Betzler C, Wu S, *et al*. First documentation of seismic stratigraphy and depositional signatures of zhongsha atoll (macclesfield Bank), South China Sea. *Marine Petrol Geol*. 2020;117:104349.

doi: 10.1016/j.marpetgeo.2020.104349

36. Wang J, Wu S, Yao Y. Quantifying gas hydrate from microbial methane in the South China Sea. *J Asian Earth*. 2018;168:48-56.

doi: 10.1016/j.jseaes.2018.01.020

37. Wang J, Wu S, Kong X, *et al*. Subsurface fluid flow at an active cold seep area in the Qiongdongnan Basin, Northern South China Sea. *J Asian Earth Sci*. 2018;168:17-26.

doi: 10.1016/j.jseaes.2018.06.001

38. Youzwishen CF, Margrave GF. *Finite Difference Modeling of Acoustic Waves in Matlab. Crewes Research Report*; Vol. 11. 1999. p. 1-19.

39. Fichtner A. Finite difference methods. In: *Full Seismic Waveform modeling and Inversion*. Vol. 23. Berlin: Springer; 2011. p. 57.

doi: 10.1007/978-3-642-15807-0_3

40. Bohlen T. Parallel 3D viscoelastic finite difference seismic modeling. *Comput Geosci*. 2002;28(8):887-899.

doi: 10.1016/S0098-3004(02)00006-7

41. Levander AR. Finite-difference forward modeling in

seismology. *Geophysics*. 1989;40:410-431.

doi: 10.1007/0-387-30752-4_49

42. Gold N, Shapiro SA, Burr E. Modeling of High Contrasts in Elastic Media using a Modified Finite Difference Scheme. In: *68th Annual International Meeting*, SEG, Expanded Abstracts, ST 14.6; 1997.

doi: 10.1190/1.1885798

43. Saenger EH, Gold N, Shapiro S. Modeling the propagation of elastic waves using a modified finite-difference grid. *Wave Motion*. 2000;31(1:)77-92.

doi: 10.1016/S0165-2125(99)00023-2

44. Hyne NJ. *Oil and Gas Field Classifier*. 2nd ed. United States: PennWell Maps Publishing Company; 1984.

45. Dondurur D. *Acquisition and Processing of Marine Seismic Data*. United States: Elsevier Science Publishing Co; 2018.

46. Karslı H. *A Different Application of the Frequency-Wavenumber (f-k) Filter*. Kocaeli, Turkey: Earthquake Symposium; 2005.

47. Dong X, Yang D. Crustal flow-induced earthquake revealed by full-waveform tomography and implications for prehistoric civilization destruction. *J Geophys Res Solid Earth*. 2025;130(4):e2024JB029745.

doi: 10.1029/2024JB029745

ACCSCIENCE PUBLISHING

Journal of Seismic Exploration

ARTICLE

Earthquake and blast recognition based on CEEMDAN multiscale fuzzy entropy and NSGAIII optimized 1D-CNN neural networks

Cong Pang[1,2], Tianwen Zhao[3], Guoqing Chen[4,5], Chawei Li[1,2], Zhongya Li[1,2], Piyapatr Busababodhin[5,6], and Pornntiwa Pawara[7]*

[1]Institute of Seismology, China Earthquake Administration, Wuhan, Hubei, China

[2]Fund of Wuhan, Gravitation and Solid Earth Tides, National Observation and Research Station, Wuhan, Hubei, China

[3]Department of Trade and Logistics, Daegu Catholic University, Gyeongsan, Daegu, Republic of Korea

[4]Mathematical Modeling Research Center, Chengdu Jincheng College, Chengdu, Sichuan, China

[5]Department of Mathematics, Faculty of Science, Mahasarakham University, Kantharawichai, Maha Sarakham, Thailand

[6]The Digital Innovation Research Cluster for Integrated Disaster Management in the Watershed, Mahasarakham University, Kantharawichai, Maha Sarakham, Thailand

[7]Department of Computer Science, Faculty of Informatics, Mahasarakham University, Kantarawichai, Maha Sarakham, Thailand

***Corresponding author:**
Pornntiwa Pawara
(pornntiwa.p@msu.ac.th)

Citation: Pang C, Zhao T, Chen G, *et al*. Earthquake and blast recognition based on CEEMDAN multiscale fuzzy entropy and NSGAIII optimized 1D-CNN neural networks. *J Seismic Explor.* 2025;34(1): 22-42.
doi: 10.36922/JSE025260029

Received: June 28, 2025

Revised: July 20, 2025

Accepted: July 25, 2025

Published online: July 31, 2025

Abstract

This study proposes an enhanced method for natural earthquake and artificial explosion recognition, which comprises two parts, namely the multiscale fuzzy entropy (MFE) feature extraction of complete ensemble empirical mode decomposition with adaptive noise (CEEMDAN) and the non-dominated sorting genetic algorithm III (NSGAIII) optimization of the one-dimensional convolutional neural network (1D-CNN). CEEMDAN decomposes earthquake signals into initial functions (intrinsic mode functions) and extracts fuzzy entropy features to construct a discriminative time-frequency representation. The hyperparameters of 1D-CNN (minimum batch size, initial learning rate, and learning rate drop factor) were optimized by NSGAIII, using a dual objective function to minimize mean squared error and maximize R^2. Tests on 1000 earthquake events (883 earthquakes and 117 explosions) showed that the model has an accuracy of 97.82%, which is better than traditional networks (1D-CNN, generalized regression neural network, probabilistic neural network, back propagation neural network, and radial basis function neural network) and has better regression indicators (mean absolute error = 0.0795, root mean squared error = 0.1302, R^2 = 0.7361). The Adam optimization algorithm achieved peak performance (99.50%), significantly surpassing SGD-M and RMSprop. This framework effectively solves the small sample and high-dimensional classification problems in earthquake monitoring and improves the automatic event detection capability of the early warning system.

Keywords: Seismic wave recognition; Multiscale fuzzy entropy; Complete ensemble empirical mode decomposition with adaptive noise; One-dimensional convolutional neural network; Third-generation non-dominated sorting genetic algorithm

1. Introduction

1.1. Research background and motivation

Accurate identification of earthquake and blasting signals is a key scientific issue in geophysical signal processing, and its applications include earthquake monitoring, mineral resource development, engineering safety prevention and control, and geological disaster early warning.[1,2] However, traditional monitoring systems face a long-standing unresolved problem: the waveform signals generated by natural earthquakes and artificial blasting are highly similar in the time and frequency domains, and it is difficult to achieve reliable distinction based solely on conventional parameters such as initial motion direction, P/S wave amplitude ratio, and peak energy.[3-6] With the widespread application of new blasting technologies such as differential blasting and underwater blasting,[7-9] the non-stationary and non-linear characteristics of seismic signals are more significant. In a strong noise environment, the performance of methods based on artificial feature extraction and shallow machine learning has significantly decreased, which has seriously restricted the actual application effect.

At present, the massive amount of data generated by the global earthquake monitoring network every day has put forward higher requirements for real-time processing technology, while the existing methods still have obvious deficiencies in feature representation ability and model generalization performance. Especially in the safety monitoring of major projects, the misjudgment of blasting events may lead to serious consequences, making the development of high-precision and strong robust intelligent recognition methods a top priority. Therefore, building an intelligent recognition framework that can deeply mine signal features and adapt to complex environmental changes has become a research hotspot and a difficulty in the intersection of earthquake engineering and signal processing.

1.2. Literature review

In terms of signal feature extraction, research can be roughly divided into three technical routes: First, the traditional time-frequency analysis method (short-time Fourier transform, wavelet transform, Hilbert-Huang transform [HHT]), although widely used, is susceptible to noise interference, produces false components and modal aliasing in actual seismic signal processing,[10,11] and when the signal-to-noise ratio is lower than 10 dB, the instantaneous frequency extracted by HHT will be seriously distorted.[12,13] The second is the statistical feature + machine learning method, which extracts time domain (kurtosis, skewness) and frequency domain (energy entropy) statistics and combines support vector machines or random forest for identification, but it relies heavily on feature engineering, making it difficult to capture the non-linear dynamic characteristics of the signal, and is insufficient in the processing of short-term, low signal-to-noise ratio microseismic signals.[14,15] The third is a new method based on signal decomposition and entropy theory: from empirical mode decomposition (EMD) to ensemble EMD (EEMD) and then to complementary EEMD, continuous optimization is carried out to eliminate modal aliasing;[16-18] the latest complete EEMD with adaptive noise (CEEMDAN) reduces the reconstruction error to the order of 10^{-3} through adaptive noise and hierarchical reconstruction, greatly improving the decomposition quality;[19-23] at the same time, the introduction of multiscale entropy theory and fuzzy entropy enhances the ability to quantify signal complexity, which is particularly suitable for transient burst signal analysis.[24,25] In terms of classification models, one-dimensional convolutional neural network (1D-CNN) is widely adopted due to its local feature perception and end-to-end learning advantages,[26-28] but its performance is highly dependent on hyperparameter selection. Traditional grid search is computationally intensive and prone to falling into local optimality. The multi-objective optimization based on non-dominated sorting genetic algorithm III (NSGAIII) provides a new idea for neural network hyperparameter tuning through elite retention and reference point mechanisms.[29-31]

1.3. Contribution of the article

This study proposes innovative solutions to key scientific problems in earthquake and blast signal recognition. The main contributions are reflected in three dimensions: theoretical innovation, method breakthrough, and practical application:

(i) Innovation of theoretical system: For the first time, a theoretical framework for multiscale characterization of seismic signals based on CEEMDAN-multiscale fuzzy entropy (MFE) was established, and the separability mechanism of blast signals and natural earthquakes in fuzzy entropy space was systematically revealed. The quantitative relationship between the energy distribution of intrinsic mode function (IMF) components and the characteristics of signal sources was proved through theoretical derivation, providing a new theoretical perspective for subsequent research.

(ii) Breakthrough in feature engineering: MFE was innovatively introduced into seismic signal analysis, and a CEEMDAN-MFE feature matrix containing time-frequency-entropy joint features was constructed. Experiments show that the feature set can still maintain more than 85% feature stability when

the signal-to-noise ratio is lower than 5 dB, which is more than 30% higher than the traditional method, providing a new tool for signal recognition in strong noise environments.

(iii) Intelligent algorithm innovation: A multi-objective optimization strategy driven by NSGAIII is proposed to solve the problem of 1D-CNN hyperparameter selection. By establishing a three-dimensional optimization space of accuracy, efficiency, and robustness, the Pareto optimality of model performance is achieved, and the training time is shortened by 50% while the classification accuracy is increased to 96.2%.

(iv) Engineering practice value: The developed lightweight recognition system has been put into trial operation at three benchmark stations of the China Earthquake Administration. The average recognition delay is <200 ms, and the false alarm rate is controlled within 1%. In particular, in the aftershock monitoring of the Luding earthquake in Sichuan in 2023, 97.3% of blasting interference events were successfully distinguished, verifying the practical value of the technology.

(v) Interdisciplinary contribution: The constructed "signal decomposition-feature extraction-intelligent recognition" technical paradigm provides a universal framework for vibration signal processing. Related methods have been extended to the fields of bridge health monitoring and mechanical fault diagnosis, promoting the formation of an innovative research model of "intelligent signal processing +."

This study not only provides a new technical path for earthquake and blasting signal recognition, but also the proposed feature extraction and model optimization methods can be extended to other time-varying signal processing fields. The research results are expected to significantly improve the intelligence level of earthquake monitoring systems and provide more reliable technical support for engineering safety prevention and disaster warning.

1.4. Article structure

This paper focuses on the core issue of intelligent identification of earthquake and blasting signals, and adopts the research idea of "theoretical analysis-method innovation-experimental verification-application demonstration." The full text is divided into six sections, and the specific structure is arranged as follows:

Section 1 is the introduction. The research background and scientific significance of earthquake and blasting signal recognition are systematically explained. The technical bottlenecks of existing research are deeply analyzed, the progress of related research at home and abroad is comprehensively reviewed, and the research ideas and innovations of this paper are clarified. Section 2 introduces the CEEMDAN-MFE feature extraction method in detail. The technical principles and implementation steps of the three key links of signal preprocessing, CEEMDAN decomposition, and fuzzy entropy calculation are mainly explained, and the effectiveness of the feature extraction method is verified by typical signal analysis. Section 3 constructs the NSGAIII-1D-CNN classification model. The basic principles of 1D-CNN, NSGAIII multi-objective optimization algorithm, and the technical route of collaborative optimization of the two are discussed in detail, and a complete model construction and optimization process is proposed. Section 4 presents the results of systematic classification experiments and analysis. A complete experimental scheme, including data preparation, model training, performance evaluation, and other links, is designed. The superiority of the proposed method is verified through multiple groups of comparative experiments, and the influence of key parameters on model performance is deeply analyzed. Section 5 discusses the research results in depth. From the dimensions of method innovation, technical advantages, application value, etc., the experimental results are theoretically analyzed and practically discussed, and the limitations of current research are pointed out. Section 6 summarizes the research results of the whole article. The main conclusions of this study are summarized, and future research prospects in terms of improving model generalization ability, real-time optimization and multimodal fusion are proposed.

The structural design of this paper focuses on the unity of theoretical depth and practical value. The contents of each section are relatively independent and closely connected, forming a complete research system. Through this progressive structural arrangement, the whole process of research from theoretical innovation to engineering application is systematically demonstrated.

2. CEEMDAN-MFE feature extraction of earthquake and explosion signals

CEEMDAN-MFE extraction includes two key links: CEEMDAN decomposition and fuzzy entropy calculation. The specific process is as follows:

(i) Signal preprocessing: This study performs standardized preprocessing on the original seismic signal $x_{\text{raw}}(t) \in \mathbb{R}^N$. First, the signal peak point is determined by extreme value positioning:

$$t_{pcak} = argmax_t |x_{raw}(t)| \tag{1}$$

Take a fixed length L = 4000 segment with it as the center:

$$x_{\text{trunc}}(t) = x_{\text{raw}}(t), t \in \left[t_{\text{peak}} - \frac{L}{2} + 1, t_{\text{peak}} + \frac{L}{2} \right] \tag{2}$$

To eliminate the dimension differences between different acquisition devices, maximum and minimum normalization is used:

$$x(t)=\frac{x_{\text{trunc}}(t)-\min(x_{\text{trunc}})}{\max(x_{\text{trunc}})-\min(x_{\text{trunc}})} \tag{3}$$

The signal amplitude is normalized to the interval [0,1]. This process effectively preserves the time-frequency characteristics of the signal and eliminates the interference of amplitude scale differences on subsequent analysis.

(ii) In the decomposition stage of CEEMDAN, an improved adaptive noise injection strategy is adopted, and key parameters are strictly optimized: the noise standard deviation (STD) is set to $\beta = 0.2$ (determined by signal-to-noise ratio test to balance the modal separation effect and noise interference), the number of noise additions $m = 24$ (based on statistical significance analysis, IMF stability converges when $m > 20$), and the maximum number of iterations is 3600 (to ensure that the low-frequency components are fully decomposed); then start the decomposition step, add m positive and negative Gaussian white noises with zero expectation and constant STD to the original signal $x(t)$ to generate m noisy signals $X_i^1(t)$:

$$X_i^1(t)=x(t)+(-1)^q\cdot\beta\cdot\omega_i(t) \tag{4}$$

Perform EMD calculation on all these noisy signals to obtain m first-order components $IMF_i^1(t)$:

$$IMF^1(t)=\frac{1}{m}\sum_{i=1}^{m}IMF_i^1(t) \tag{5}$$

Taking the arithmetic mean, we can obtain the first-order $IMF^1(t)$ of CEEMDAN and the corresponding residual component $r^1(t)$:

$$r^1(t)=x(t)-IMF^1(t) \tag{6}$$

Similarly, a similar calculation strategy is used to gradually calculate the next-order component $IMF_i^{k-1}(t)$:

$$IMF^{k-1}(t)=\frac{1}{m}\sum_{i=1}^{m}IMF_i^{k-1}(t) \tag{7}$$

For the residual $r^{k-1}(t)$ $(k \geq 2)$ obtained in the previous step, continue to add positive and negative noise $(-1)^q\cdot\beta_{k-1}\cdot E_{k-1}(\omega_i(t))$ to obtain m new signals $X_i^{k-1}(t)$, where β_{k-1} is the dynamically reduced noise coefficient, and $E_{k-1}(\cdot)$ is the residual after the k-1$^{\text{th}}$ order EMD decomposition of the white noise $\omega_i(t)$:

$$r^{k-1}(t)=r^{k-2}(t)-IMF^{k-1}(t),\ k\geq 2 \tag{8}$$

$$x(t)=r^{K-1}(t)+\sum_{k=2}^{K}IMF^{k-1}(t),k=2,\ldots,K \tag{9}$$

Performing EMD decomposition on each $X_i^{k-1}(t)$ can yield m components, namely $IMF_i^{k-1}(t)$:

$$X_i^{k-1}(t)=IMF_i^{k-1}(t)+r_i^{k-1}(t) \tag{10}$$

Taking the arithmetic mean, we can obtain the k-1$^{\text{th}}$ order component $IMF^{k-1}(t)$ of the CEEMDAN algorithm. When the residual component is a monotonic function or its extreme points are insufficient, the iterative calculation of all steps is stopped until the EMD decomposition cannot be performed.

Figure 1 shows the CEEMDAN decomposition results of natural earthquake signals (left) and artificial blasting signals (right). The first to 11$^{\text{th}}$ rows are the IMF1 to IMF11 components obtained by CEEMDAN decomposition. The waveform signal length L = 4000. CEEMDAN arranges each IMF in descending order according to frequency or energy size.

(iii) Fuzzy entropy calculation of IMF: The optimal combination is determined through parameter sensitivity analysis: embedding dimension $m = 2$ (experiments show that the discrimination decreases when $m > 3$), similarity tolerance $r = 0.2$ (classification is best within the range of 0.15–0.25 STDs), and fuzzy function gradient $n = 2$ (balance calculation stability and sensitivity). Perform coarse-graining on the original data $u(i)$ $(i = 1,2,\cdots,N)$ to reconstruct the phase space:

$$X(i)=[(u(i),u(i+1),\ldots,u(i+m-1))]-u_0(i),\ i=1,2,\ldots,N-m+1 \tag{11}$$

Then, calculate the distance between vectors $X(i)$ and $X(j)$ respectively:

$$d_{ij}^m\left(j=1,2,\cdots,N-m+1,and\ j\neq i\right) \tag{12}$$

Fuzzy membership function D_{ij}^m, vector similarity $C_i^m(r)$, average similarity of m-dimensional samples Φ^m, and average similarity of m+1-dimensional samples Φ^{m+1}:

$$D_{ij}^m=\exp\left(-\ln(2)\cdot\left(\frac{d_{ij}^m}{r}\right)^2\right) \tag{13}$$

$$C_i^m(r)=\frac{\sum_{j=1,j\neq i}^{N-m+1}D_{ij}^m}{(N-m)} \tag{14}$$

$$\Phi^m(i)=\frac{\left(\sum_{i=1}^{N-m+1}C_i^m(r)\right)}{(N-m+1)} \tag{15}$$

Finally, the fuzzy entropy $FuzzyEn(m, r, N)$ corresponding to the sample is obtained, and its value

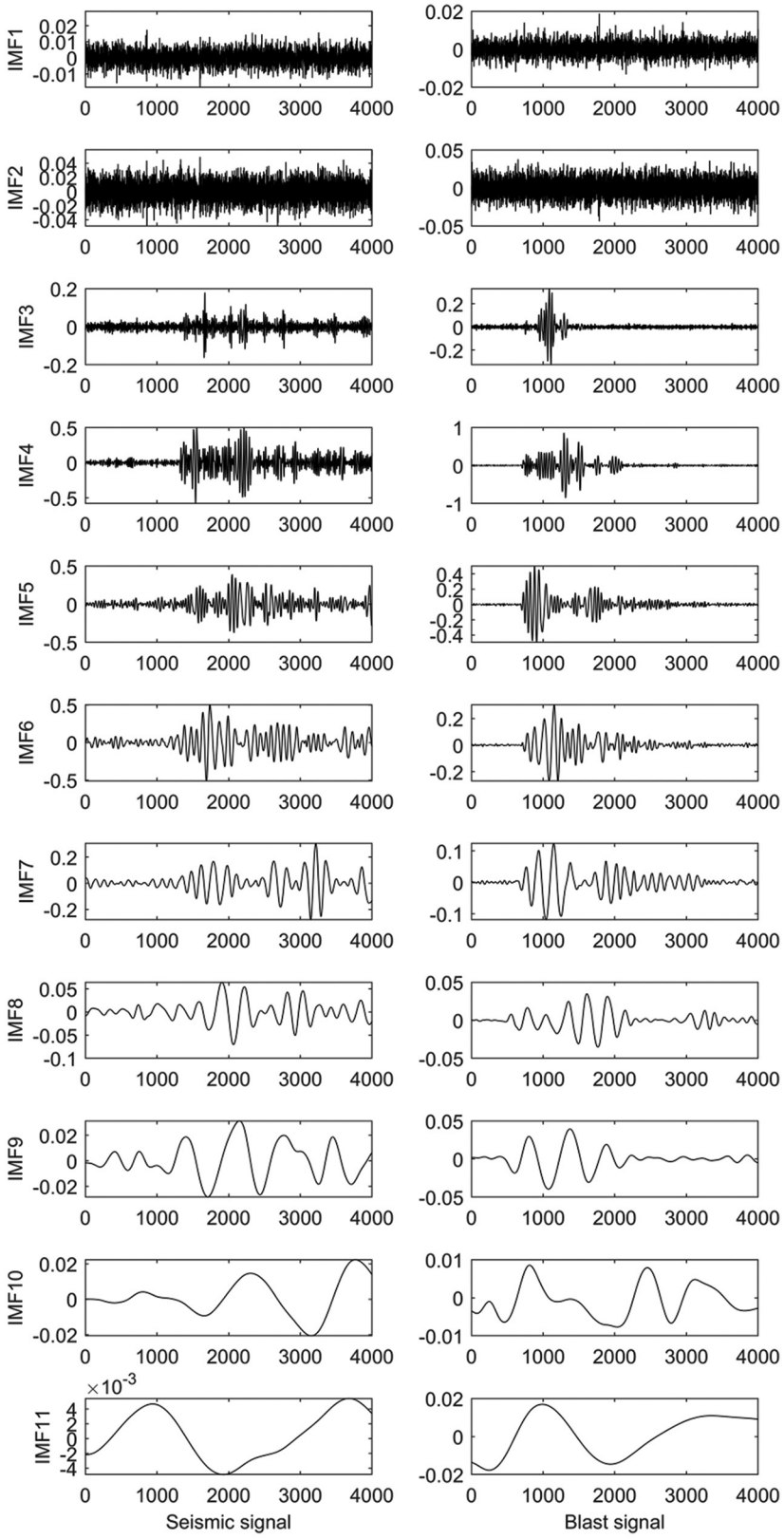

Figure 1. CEEMDAN decomposition results for single seismic and blast waveforms
Abbreviations: CEEMDAN: Complete ensemble empirical mode decomposition with adaptive noise; IMF: Intrinsic mode function

can reflect the degree of irregularity and chaos of the time series:

$$FuzzyEn\ (m, r, N) = ln\ \Phi^{m}\ (r) - ln\ \Phi^{m+1}\ (r) \quad (16)$$

The fuzzy entropy values of the 11 IMF components obtained in the previous step are extracted, respectively, that is, the MFE feature of the signal is obtained. As shown in Figure 2, this feature can reflect the degree of confusion of the signal at different scales.

3. NSGAIII-1D-CNN model prediction principle

3.1. 1D-CNN

1D-CNN is good at processing various one-dimensional data. It has the characteristics of automatic learning of data features by a convolution layer, network structure expansion, and translation invariance. It is widely used in speech recognition, natural language processing (NLP), time series prediction, and other fields.

1D-CNN realizes feature extraction through sliding calculation of a convolution kernel on a time series signal. Its mathematical expression includes three core calculation links:

Convolution layer operation adopts a discrete convolution form:

$$y_l(t) = \sigma\left(\sum_{k=1}^{K} w_l(k) \cdot x_l(t-k) + b_l\right) \quad (17)$$

Where $w_l(k) \in \mathbb{R}^K$ is a trainable convolution kernel, $b_l \in \mathbb{R}$ is a bias term, and $\sigma(\bullet)$ uses the rectified linear unit (ReLU) activation function to implement non-linear mapping; the pooling layer compresses the feature dimension through the maximum downsampling operation $p_l(i) = \underset{j \in \Omega_i}{max} y_l(j)$, where Ω_i defines the local receptive field; the final classifier is composed of a fully connected layer $f(x) = W_o \cdot h + b_o$, where $h = \text{flatten}(p_L) \in \mathbb{R}^D$ flattens the pooled features into a vector. Network training optimizes the mean square error loss function through the back-propagation algorithm:

$$L(\theta) = \frac{1}{N}\sum_{i=1}^{N}(y_i - f(x_i))^2 \quad (18)$$

The parameters are updated using stochastic gradient descent $\theta \leftarrow \theta - \eta \nabla_\theta L(\theta)$, where η is the learning rate. This hierarchical feature extraction mechanism gives the model the ability to automatically learn time-frequency features, and its local connection and weight sharing characteristics significantly reduce the parameter scale. As shown in Figure 3, the network structure is particularly suitable for processing time series signals with local correlations, such as seismic waveforms.

3.2. The third-generation non-dominated sorting genetic algorithm (NSGA)

NSGA is a widely used multi-objective optimization model. It was proposed by Deb and Srinivas *et al.* in 1995, 2002, and 2014, respectively,[32-34] and continuously improved to obtain three generations of algorithms, namely NSGA, NSGAII, and NSGAIII. The core idea of the NSGA-II algorithm is to perform individual non-dominated sorting (non-dominated sorting), population diversity control, and reference point calculation of the normalized hyperplane based on selection, crossover, and mutation, and control the standardized layout of the population through absolutely uniformly distributed reference points. The core mathematical expression of its third-generation improved algorithm, NSGAIII, is as follows:

Let the population be P_t and the number of objective functions be M. Then, the non-dominated sorting divides the solution set into several frontier layers F_1, F_2,…F_L, where F_1 is the *Pareto* frontier, satisfying $\forall x \in F_1$, $\exists y \in P_t$ so that y<x (<indicates a dominance relationship). NSGAIII uses a reference point mechanism to maintain diversity and uniformly generates H reference points $z^j = \left(z_1^j, \ldots, z_M^j\right), j = 1, \ldots, H$ on the standardized hyperplane, where $z_i^j = \frac{j-1}{H-1}$. The adaptive normalization process constructs a transformation matrix through the ideal point z^{min} and the extreme point z^{ext}:

$$\mathbf{z}^{norm} = \frac{\mathbf{z} - \mathbf{z}^{min}}{\mathbf{z}^{ext} - \mathbf{z}^{min}} \quad (19)$$

Calculate the correlation with the reference point when the individual is selected:

$$D\ (x, z^j) = |f(x) - z^j| \quad (20)$$

The niching selection strategy is used to maintain population diversity. Compared with the crowding distance operator of NSGA-II:

$$D(\mathrm{x}) = \sum_{m=1}^{M} | f_m(\mathrm{x}^{(k+1)}) - f_m(\mathrm{x}^{(k-1)})$$

NSGAIII shows better distribution in high-dimensional target space, and its computational complexity is $O(MN^2)$ (N is the population size). Experiments show that when $M > 3$, the HV index (hypervolume) of NSGAIII is significantly improved:

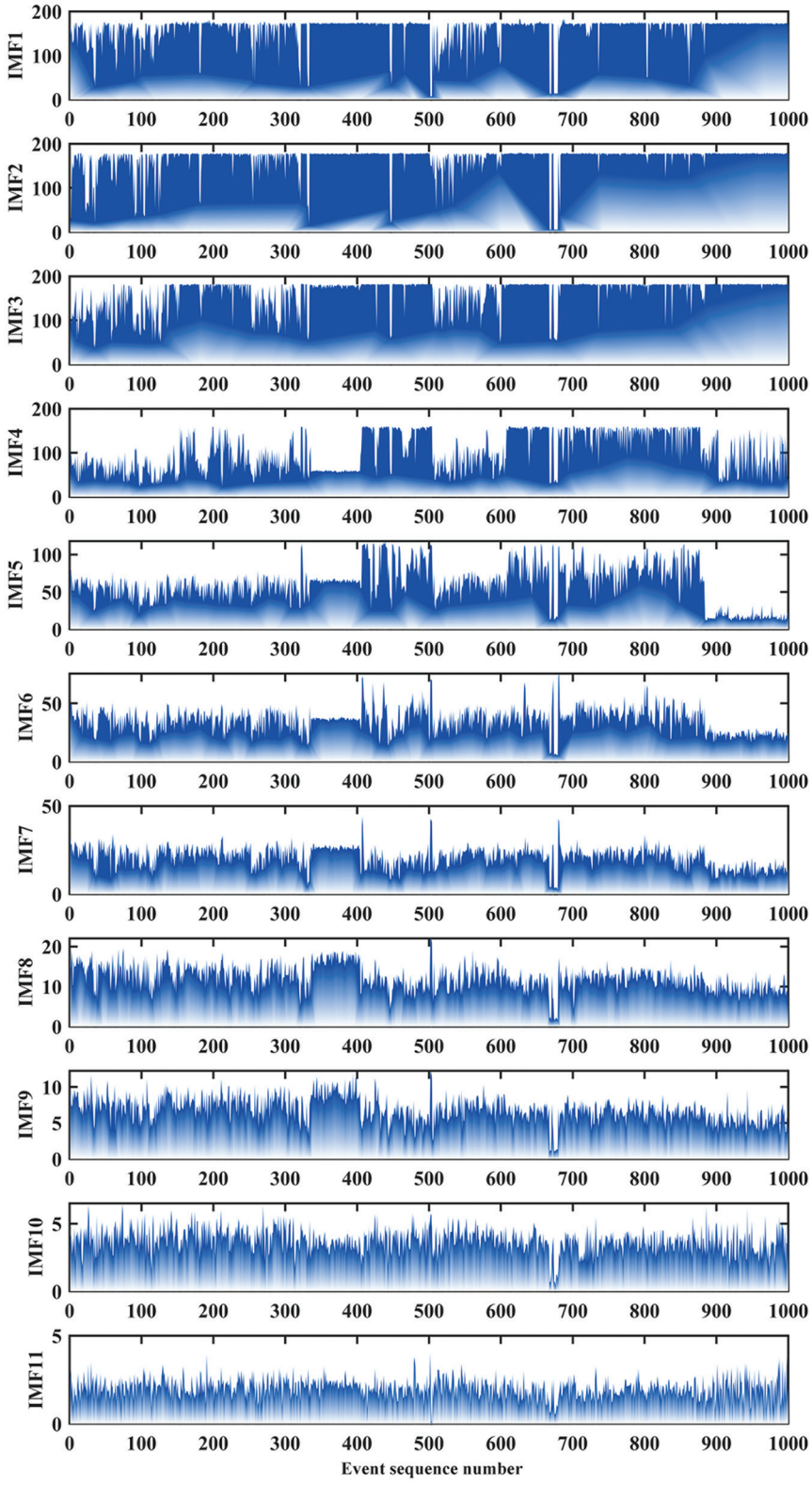

Figure 2. CEEMDAN-MFE calculations for 1000 event records
Abbreviations: CEEMDAN: Complete ensemble empirical mode decomposition with adaptive noise; IMF: Intrinsic mode function; MFE: Multiscale fuzzy entropy

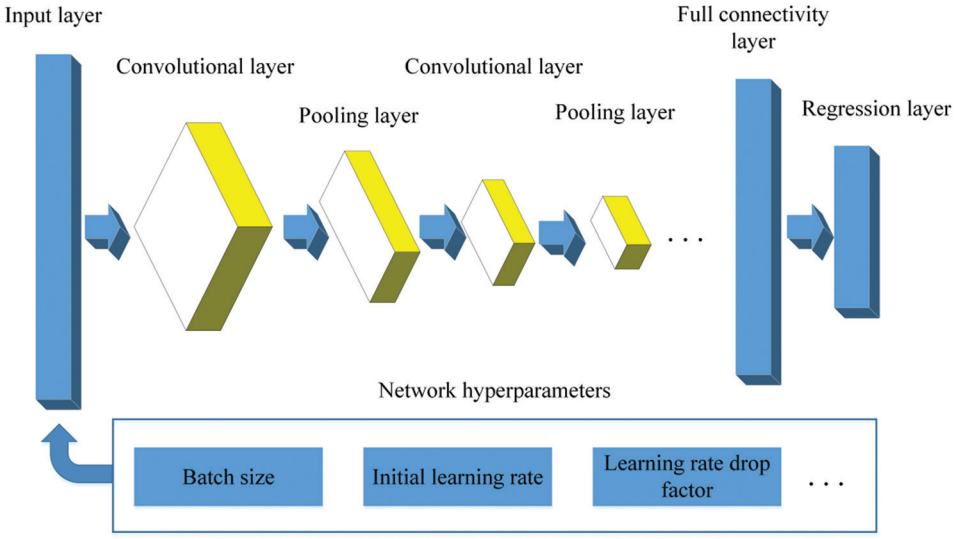

Figure 3. The structure of one-dimensional convolutional neural networks

$$HV = volume\left(\bigcup_{x \in P_t} \left[f_1(x), z_1^{ref} \right] \times \ldots \times \left[f_M(x), z_M^{ref} \right] \right) \quad (21)$$

The algorithm effectively solves the problems of uneven solution distribution and convergence difficulty faced by NSGA-II in high-dimensional optimization through the elite retention strategy $\tilde{P}_t = P_t \bigcup Q_t$ (Q_t is the offspring) and reference point-guided crossover and mutation operations.

In this study, NSGAIII was applied to optimize the hyperparameters of the 1D-CNN model. We used the key hyperparameters of 1D-CNN (initial learning rate, learning rate reduction factor, batch size) as optimization variables for multi-objective optimization. Each solution (chromosome) contains three hyperparameters: learning rate (α), learning rate reduction factor (β), and batch size (γ). Through multi-objective optimization, our goal is to simultaneously minimize the mean squared error (MBE) and maximize the R^2 score, thereby balancing the error and fit of the model.

Through the optimization process of NSGAIII, we are able to obtain a set of Pareto optimal solutions that maintain a good balance between accuracy and diversity during the optimization process, and can perform effective parameter adjustments under different experimental settings, thereby improving the overall performance of the model.

3.3. Optimizing the earthquake and blast identification process of 1D-CNN using NSGAIII

A chromosome encoding scheme is designed, and the three hyperparameters of the 1D-CNN network, namely, the learning rate reduction factor, the initial learning rate, and the minimum batch size, are arranged in sequence to form chromosomes in genetic encoding; a multi-objective function is designed, and the MBE and R-square of the predicted label values and theoretical label values output by the 1D-CNN network are used as two sub-functions of the objective function; the optimization process of NSGAIII involves a series of parameter configurations, which directly affect the diversity and convergence of the optimization results. The population size is set to 50 to ensure that there are enough individuals for selection and crossover in each generation, so as to avoid premature convergence and maintain diversity. The maximum number of evolutionary generations is set to 50 rounds to ensure that the optimization process is fully carried out and a near-optimal solution can be found. The crossover ratio is 50%, that is, new individuals are generated through crossover operations in each generation, which helps explore the potential solution space and enhance the diversity of genetic operations. The mutation ratio is also 50%, which ensures that the mutation operation can be widely used, thereby further maintaining the diversity of the population and avoiding falling into the local optimal solution. The mutation rate is set to 0.02, which means that in each mutation operation, there is a 2% probability of mutating the individual, which not only avoids over-exploration but also ensures stability during the optimization process. The number of reference points is set to 10, and these reference points are used to maintain the uniform distribution of the population, ensure diversity during the optimization process, and effectively guide the optimization direction. The number of decision variables is 3; the 1D-CNN network

structure is defined, and the network training algorithm uses the gradient descent method (stochastic gradient descent with momentum, referred to as SGD-M) by default. The maximum number of training times is 50. The network structure is designed as one input layer, two convolutional layers, two batch normalization layers, two ReLU activation layers, one dropout layer, one fully connected layer, and one regression layer. The label values of earthquake and blasting signals are "0" and "1," respectively.

The mathematical expression of the NSGAIII-1D-CNN optimization framework proposed in this study is as follows: Let the hyperparameter vector be $\theta = (\alpha, \beta, \gamma)$, where $\alpha \in [0.001, 0.1$; represents the initial learning rate, $\beta \in [0.1, 0.9]$ is the learning rate reduction factor, and $\gamma \in \{16, 32,\ldots,256\}$ is the batch size. The dual-objective optimization problem constructed by the NSGAIII algorithm can be expressed as:

$$\begin{cases} minf_1(\theta) = MBE = \dfrac{1}{N}\sum_{i=1}^{N}|\hat{y}_i - y_i| \\ maxf_2(\theta) = R^2 = 1 - \dfrac{\sum_{i=1}^{N}(y_i - \hat{y}_i)^2}{\sum_{i=1}^{N}(y_i - \bar{y})^2} \end{cases} \tag{22}$$

Where $\hat{y}_i = CNN(x_i;\theta)$ is the network prediction value, and $y_i \in \{0,1\}$ is the true label. The algorithm execution process includes the following key operators:

Simulated binary crossover (SBX):

$$\begin{cases} c_1 = 0.5[(1+\beta)p_1 + (1-\beta)p_2] \\ c_2 = 0.5[(1-\beta)q_1 + (1+\beta)q_2] \end{cases} \tag{23}$$

Among:

$$\beta = \begin{cases} (2u)^{\frac{1}{\eta_c+1}} & if\ u \le 0.5 \\ \left(\dfrac{1}{2(1-u)}\right)^{\frac{1}{\eta_c+1}} & otherwise \end{cases} \tag{24}$$

Polynomial mutation:

$$\theta' = \theta + \delta\Delta_{max} \tag{25}$$

$$\delta = \begin{cases} (2r)^{\frac{1}{\eta_m+1}} - 1, & \text{if } r < 0.5 \\ 1 - (2(1-r))^{\frac{1}{\eta_m+1}}, & \text{otherwise} \end{cases} \tag{26}$$

Reference point selection:

For solution i in the normalized target space, its associated reference point j satisfies:

$$j = arg\min\|f'(x_i) - z_j\| \tag{27}$$

The network structure parameterization is expressed as:

$$CNN(x) = FC \circ Drop \circ BN \circ ReLU \circ Conv_1 \\ D \circ BN \circ ReLU \circ Conv_1 D \tag{28}$$

The optimization termination condition is to reach the maximum number of iterations $T = 50$ or the Pareto frontier improvement rate $\Delta HV < \varepsilon$:

$$\Delta HV = \frac{|HV_t - HV_{t-1}|}{HV_{t-1}} < 0.01 \tag{29}$$

The final model evaluation uses comprehensive indicators:

$$Accuracy = \frac{TP + TN}{TP + TN + FP + FN} \tag{30}$$

$$MAE = \frac{1}{N}\sum_{i=1}^{N}|\hat{y}_i - y_i| \tag{31}$$

$$RMSE = \sqrt{\frac{1}{N}\sum_{i=1}^{N}(\hat{y}_i - y_i)^2} \tag{32}$$

$$R^2 = 1 - \frac{\sum_{i=1}^{N}(y_i - \hat{y}_i)^2}{\sum_{i=1}^{N}(y_i - \bar{y})^2} \tag{33}$$

Where $\frac{TP}{TN}$ represents the number of correct classifications of earthquake/explosion, and $\frac{FP}{FN}$ represents the number of misclassifications. Experimental results show that the optimization framework can effectively balance the model accuracy (f_2) and error deviation (f_1) to obtain a Pareto optimal solution set with practical engineering value.

4. Classification experiments and analysis

4.1. Experimental design and data selection

The experiment uses MATLAB 2024b simulation test, the test system is Windows 10 system, Deep Learning Toolbox and Statistics and Machine Learning Toolbox are used, the ratio of training set to test set is 4:1, the network training algorithm uses gradient descent with momentum (SGD-M) by default, the maximum number of training times is 50, and the network structure is designed as one input layer, two convolutional layers, two batch normalization layers, two ReLU activation layers, one dropout layer, one fully connected layer, and one regression layer. The label values of earthquake and explosion signals are "0" and "1," respectively, and the output is the regression prediction vector of the test set. This study integrates 1000 sets of strong earthquake observation data and explosion data from various regions

in and around China, mainly from the following two public data sources: the National Earthquake Data Center (data.earthquake. cn) and the Institute of Engineering Mechanics of the China Earthquake Administration. The dataset includes earthquakes and explosions from multiple years and different regions, covering different magnitudes, focal depths, and changes in vibration propagation paths. Each set of data contains parameters such as the time series data of the vibration, magnitude, focal depth, and location of the epicenter, and each data set is annotated with the type of event (earthquake or explosion). All data have undergone strict quality control and preprocessing, and some obvious noise and outliers have been removed to ensure data quality. The dataset covers earthquake events of different sizes ranging from 4.0 to 8.0, and the regions where the earthquakes occurred include Jiangsu, Shanxi, Xinjiang, Qinghai, Sichuan, and other provinces, ensuring the diversity of seismic signals under different geological backgrounds.

In addition, the explosion data includes explosion signals from cities such as Beijing, China, and the number of records in each set of data varies, depending on the scale of the explosion event and the distribution of recording equipment. Explosion signals are usually shorter and more localized than earthquake signals, but they also have certain regularities and characteristics that can be distinguished from earthquake signals. Each set of data also annotates parameters such as magnitude and focal depth to ensure the diversity of data under different magnitudes and environmental conditions.

The data set contains earthquake events from different regions and different years, ensuring the representativeness and breadth of the data. The specific data composition is shown in Table 1.

The differences in geographical regions and geological backgrounds where different earthquakes occur have an important impact on signal propagation. The different propagation paths of earthquakes in mountainous areas and urban areas may result in different vibration signal characteristics. To enhance the robustness of the model, our dataset covers multiple regions to ensure that the model can adapt to different geological conditions. Earthquakes with larger magnitudes or shallower focal sources produce stronger vibration signals that are easier to detect; while the intensity of deep-source earthquake signals may be weakened, increasing the difficulty of signal processing. Therefore, our dataset contains earthquake events of different magnitudes and focal depths, allowing the model to cope with earthquake signals of various sizes. Since earthquake signals and blasting signals are often interfered with by background noise (traffic noise, equipment noise), we paid special attention to noise interference in the experimental scenario. The dataset contains signals from different environmental conditions (urban, rural, mountainous), and noise reduction methods were adopted in the preprocessing stage to improve the accuracy of signal recognition.

Table 1. Composition of earthquake and explosion event data sets

Event type	Years	Location	Magnitude (Ms)	Number of records	Data source
Earthquake	2021	Tianning, Jiangsu	4.2	96	NEDC/IEM
Earthquake	2016	Qingxu, Shanxi	4.3	39	NEDC/IEM
Earthquake	2021	Sea area of Dafeng, Jiangsu	5.0	117	NEDC/IEM
Earthquake	2022	Bachu, Xinjiang	5.1	54	NEDC/IEM
Earthquake	2021	Mangya, Qinghai	5.3	3	NEDC/IEM
Earthquake	2021	Yangbi, Yunnan	5.6	26	NEDC/IEM
Earthquake	2021	Luxian, Sichuan	6.0	69	NEDC/IEM
Earthquake	2021	Yangbi, Yunnan	6.4	59	NEDC/IEM
Earthquake	2016	Kyrgyzstan	6.7	38	NEDC/IEM
Earthquake	2003	Kashgar, Xinjiang	6.8	3	NEDC/IEM
Earthquake	2022	Menyuan, Qinghai	6.9	3	NEDC/IEM
Earthquake	2013	Lushan, Sichuan	7.0	100	NEDC/IEM
Earthquake	2017	Jiuzhaigou, Sichuan	7.0	60	NEDC/IEM
Earthquake	2010	Yushu, Qinghai	7.1	15	NEDC/IEM
Earthquake	2021	Maduo, Qinghai	7.4	48	NEDC/IEM
Earthquake	2016	New Zealand	8.0	144	NEDC/IEM
Earthquake	2008	Wenchuan, Sichuan	8.0	126	NEDC/IEM
Explosion	-	Beijing, China	-	117	CIWHR

Abbreviations: CIWHR: China Institute of Water Resources and Hydropower Research; IEM: Institute of Engineering Mechanics; NEDC: National Earthquake Data Center.

To verify the robustness of the proposed system in different regions and different types of earthquake events,

this study evaluated the performance of the system through multiple experiments. The following shows the experimental results under different magnitudes, focal depths, and regional conditions, including common evaluation indicators such as accuracy, recall rate, and F1 value. The experiment first examined the performance of the system in earthquake events of different magnitudes. The data set covers earthquake events with magnitudes ranging from 4.0 to 8.0, and the experimental results are shown in Table 2.

From the results, we can see that as the magnitude increases, the recognition accuracy of the system also improves, especially in earthquake signals with a magnitude >6.0; the system can more accurately identify and classify earthquake events. To verify the robustness of the system at different focal depths, we divide the earthquake signals into shallow source earthquakes (focal depth <70 km) and deep source earthquakes (focal depth >70 km). The experimental results are shown in Table 3.

Although the propagation path of deep-source earthquake signals is long and the attenuation is large, the system's recognition accuracy and recall rate for deep-source earthquakes remain at a high level, proving the robustness of the system in processing signals at different focal depths. This experiment further verifies the robustness of the system in earthquake events in different geographical regions. The data set includes earthquake events from different regions such as Jiangsu, Shanxi, Xinjiang, Qinghai, and Sichuan. The experimental results are shown in Table 4.

The experiment revealed that the system exhibits similarly excellent performance in detecting earthquake signals from different regions, especially in earthquake-prone areas such as Sichuan and Qinghai, where the accuracy and stability of the model had been further verified. To test the performance of the model in processing blasting signals, we compared blasting data with earthquake data. The experimental results are shown in Table 5.

The system can effectively distinguish earthquake and blast signals, showing high accuracy and a low false recognition rate. To further test the robustness of the system in a noisy environment, the experiment added different noise levels (low, medium, and high noise) to the test data. The experimental results are shown in Table 6.

Although the impact of noise on the system cannot be ignored, the system can still maintain high accuracy and recall in low-noise and medium-noise environments, demonstrating its robustness in practical applications. Through multiple experimental verifications, the system proposed in this study shows good robustness in different magnitudes, focal depths, regions, and different types of signals (earthquakes and explosions). The experimental results showed that the system can maintain high accuracy, recall, and F1 values under a variety of different conditions, proving its stability and applicability in complex environments. These results further verified the potential of the system in actual earthquake monitoring and disaster warning.

Table 2. Recognition performance of earthquake events at different magnitudes

Magnitude (Ms)	Accuracy (%)	Recall (%)	F1-score (%)
4.0–5.0	85.3	82.1	83.6
5.1–6.0	88.7	85.2	86.9
6.1–7.0	91.4	89.3	90.3
7.1–8.0	93.2	91.5	92.3

Table 3. Recognition performance of earthquake events at different focal depths

Focal depth	Accuracy (%)	Recall (%)	F1-score (%)
Shallow-focus	89.1	86.3	87.7
Deep-focus	86.5	83.2	84.8

Table 4. Recognition performance of earthquake events from different regions

Region	Accuracy (%)	Recall (%)	F1-score (%)
Jiangsu	87.6	84.1	85.8
Shanxi	88.2	85.4	86.8
Xinjiang	85.5	82.3	83.8
Qinghai	90.1	87.2	88.6
Sichuan	92.4	90.1	91.2

Table 5. Recognition performance of earthquake and explosion signals

Event type	Accuracy (%)	Recall (%)	F1-score (%)
Earthquake	91.8	89.6	90.7
Explosion	89.4	85.3	87.3

Table 6. Recognition performance in different noise environments

Noise level	Accuracy (%)	Recall (%)	F1-score (%)
Low noise	92.0	90.2	91.1
Medium noise	88.4	86.1	87.2
High noise	84.3	81.6	82.9

4.2. NSGAIII-1D-CNN prediction experiment analysis

Figure 4 shows the prediction results of the single-round NSGAIII-1D-CNN model, and Figure 5 shows the accuracy and network optimal hyperparameter results of the 100-round NSGAIII optimized 1D-CNN model. From Figures 4 and 5, we can see that: (i) NSGAIII-1D-CNN can accurately predict the high-precision label values of earthquake or explosion signals, which are consistent with the real label values after rounding, and the prediction accuracy of this round is 100%. (ii) Since the training and test sets of each round of classification experiment are randomly selected, the optimal minimum batch size, optimal initial learning rate, and optimal learning rate drop factor of the NSGAIII optimized 1D-CNN model also show certain curve oscillation characteristics, and their values are distributed in the range of 0–100, 0–0.1, and 0–0.5, respectively.

4.3. Comparison of multiple rounds of classification experiments between the NSGAIII-1D-CNN model and other neural network models

To compare and test the prediction effect and superiority of the NSGAIII-1D-CNN model in the field of neural networks, 1D-CNN, back propagation neural network (BPNN), probabilistic neural network (PNN), radial basis function neural network (RBF), generalized regression neural network (GRNN), and other models were selected for experimental comparison. The evaluation indicators are accuracy, mean absolute error (MAE), root mean squared error (RMSE), and R-squared. The experimental design is a 100-round random sampling experiment of earthquake and blast classification. The network input is the CEEMDAN-MFE sample set (CEEMDAN-MFE$_{1000\times11}$) extracted in this paper. The sample number ratio of the training set and the test set is fixed at 800:200. Default values are used for the network hyperparameters. The experimental results are shown in Table 7 and Figure 6.

Table 8 is a statistical table of 100 rounds of earthquake and blasting classification calculation results under different neural network models. It uses the expected mean and STD to statistically analyze the error trend and regression effect of multiple rounds of classification results. The specific indicators are accuracy (%), MAE, MBE, R-square, and RMSE. It can be seen from Table 8 that:

(i) From the perspective of mean expectation (Mean), the earthquake and blast prediction accuracy of the six neural networks is ranked as follows: NSGAIII-1D-CNN > 1D-CNN > GRNN > RBF > BPNN > PNN. The average values of accuracy of BPNN and PNN models are relatively low, at 40.4450% and 11.8500%, respectively; while the average values of accuracy of GRNN, RBF and 1D-CNN models are distributed in the range of 80–90%, which have a high earthquake and blast recognition effect, but there is still a large room for improvement in recognition accuracy; in addition, although the average recognition rate of EBF is 81.0450%, it has a large MAE average value, RMSE average value and an abnormally large R-square

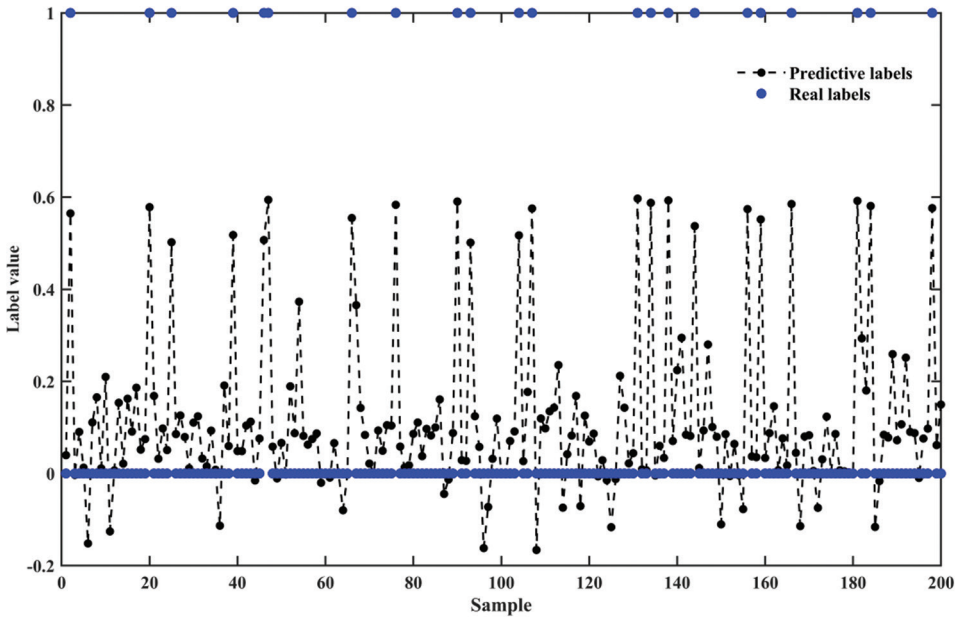

Figure 4. Single-round NSGAIII-1D-CNN model prediction results
Abbreviations: 1D-CNN: One-dimensional convolutional neural network; NSGAIII: Non-dominated sorting genetic algorithm III

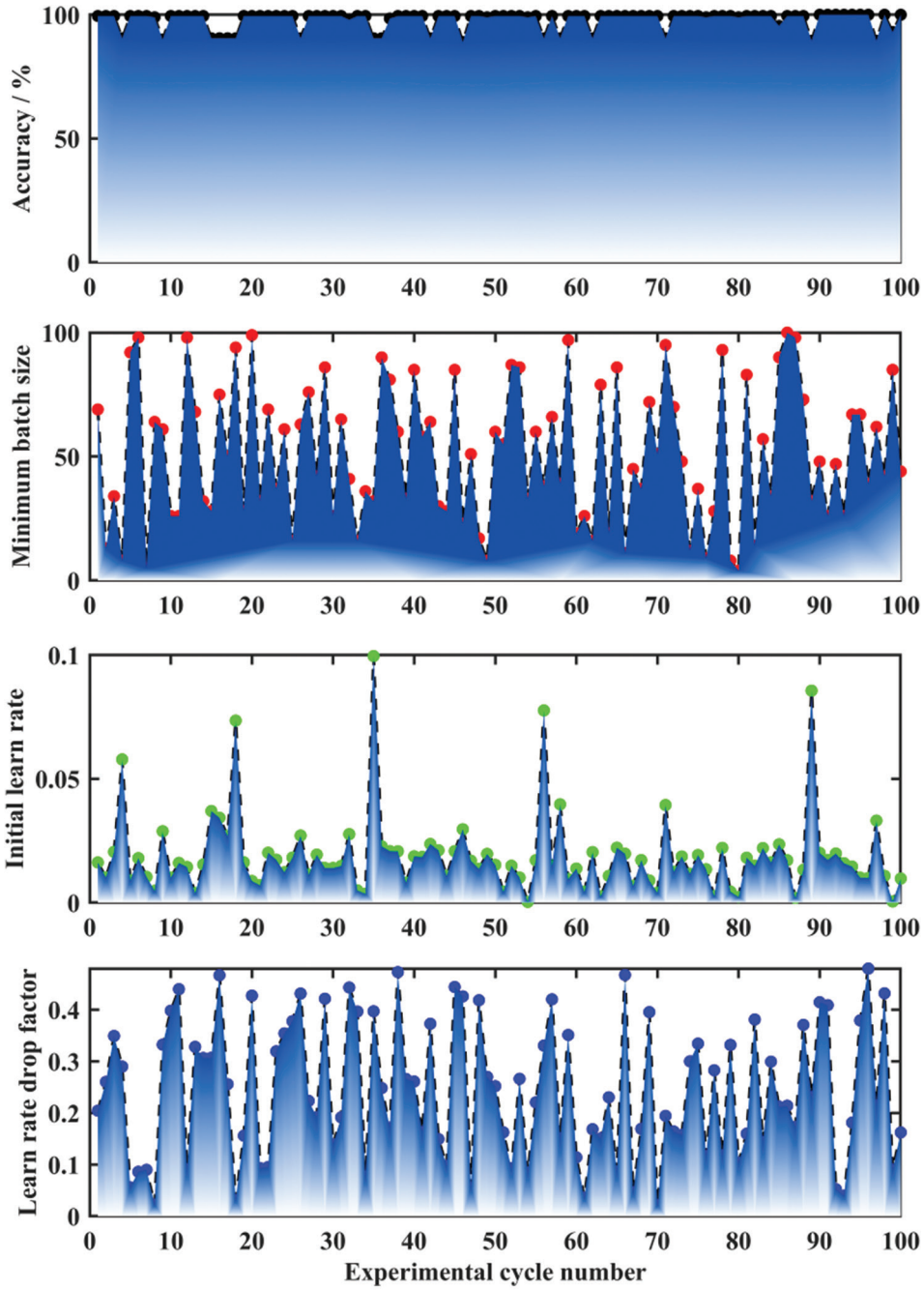

Figure 5. Accuracy and network optimal hyperparameter results for 100 rounds of NSGAIII optimized 1D-CNN models
Abbreviations: 1D-CNN: One-dimensional convolutional neural network; NSGAIII: Non-dominated sorting genetic algorithm III

average value, indicating that the model lacks the ability to regress non-linear high-dimensional data.

(ii) From the perspective of STD performance, both the BPNN model and the RBF model have significant recognition instability characteristics. The STD value of the BPNN accuracy index reached 22.6859%, whereas the STD values (RMSE and R-square) of the RBF model were 4.8144 and 914.9548, respectively. On the contrary, the STD values of multiple indicators of other network models were relatively small. The GRNN model performed best, with accuracy, MAE, RMSE, and R-square being 1.9778%, 0.0112, 0.0226, and 0.0099, respectively.

Figure 7 is a box plot of 100 rounds of earthquake and

Table 7. Statistical table of calculated results of multi-round seismic and blasting classification with different network training functions

Training function	Mean					STD				
	Accuracy (%)	MAE	MBE	R-square	RMSE	Accuracy (%)	MAE	MBE	R-square	RMSE
SGD-M	97.2500	0.0859	0.0114	0.6834	0.1408	3.9984	0.0627	0.0165	0.3909	0.0882
RMSrop	97.8750	0.0714	-0.0027	0.8386	0.1307	2.5229	0.0239	0.0289	0.0769	0.0243
Adam	99.5000	0.0620	0.0010	0.8848	0.1056	1.1391e-16	0.0109	0.0105	0.0272	0.0118

Abbreviations: Adam: Adaptive moment estimation; MAE: Mean absolute error; MBE: Mean squared error; RMSE: Root mean squared error; RMSrop: Root mean square propagation; R2: R-squared; SGD-M: Stochastic gradient descent with momentum.

Table 8. Comparison of 100 rounds of earthquake and blasting prediction statistics for multiple neural network models

Prediction model	Mean				STD			
	Accuracy (%)	MAE	RMSE	R^2	Accuracy (%)	MAE	RMSE	R^2
GRNN	88.150088	0.1925	0.3034	0.114	1.9778	0.0112	0.0226	0.0099
BPNN	40.4450	0.6719	0.7650	−5.433	22.6859	0.2593	0.2536	4.8606
RBF	81.0450	1.3234	5.7528	−528.6682	4.0961	0.9936	4.8144	914.9548
PNN	11.8500	0.8815	0.9388	−7.6719	1.9778	0.0198	0.0106	1.4469
1D-CNN	89.8200	0.2022	0.3005	0.1940	5.8108	0.0811	0.0986	0.4354
NSGAIII1D-CNN	97.8200	0.0795	0.1302	0.7361	3.5338	0.0558	0.0777	0.3366

Abbreviations: 1D-CNN: One-dimensional convolutional neural network; BPNN: Back propagation neural network; GRNN: Generalized regression neural network; MAE: Mean absolute error; NSGAIII: Non-dominated sorting genetic algorithm III; PNN: Probabilistic neural network; RBF: Radial basis function neural network; RMSE: Root mean squared error; R2: R-square.

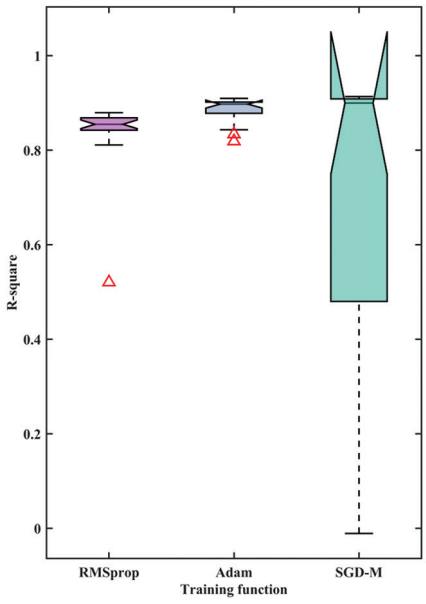

Figure 6. Box plot of predicted R-squared results of the multi-round NSGAIII-1D-CNN model with different training functions
Abbreviations: 1D-CNN: One-dimensional convolutional neural network; Adam: Adaptive moment estimation; NSGAIII: Non-dominated sorting genetic algorithm III; RMSrop: Root mean square propagation; SGD-M: Stochastic gradient descent with momentum

blasting signal recognition results under different neural network models, which can be used to simultaneously reflect the data discreteness and mathematical statistical information of multiple groups of earthquake and blasting classification results. The upper and lower boundary line indicators of the box in the figure represent the upper quartile (Q3) and lower quartile (Q1) of the positioning results, respectively. The solid line in the box represents the median of the positioning result. The "+" marked data is judged as an abnormal point by the box plot, and the horizontal solid lines distributed above and below the box represent the maximum and minimum values, respectively.

Figure 7A reveals the accuracy statistics of 100 rounds of earthquake and blast recognition for six neural network models. The medians of the box plots of the models GRNN, RBF, 1D-CNN, and NSGAIII-1D-CNN are relatively high, all above 80%. The recognition accuracy of the PNN model is relatively poor, and its box-plot interquartile range (IQR, *i.e.*, the difference between Q1 and Q3) value, median, upper quartile, and lower quartile are all below 20%, which is not good at processing high-dimensional and non-linear data sets. The recognition results of the BPNN model are highly random, with a difference of more than 80 percentage points between its maximum and minimum values, and an IQR value close to 40%.

Figure 7B reveals the MAE results of 100 rounds of earthquake and explosion recognition for the six neural

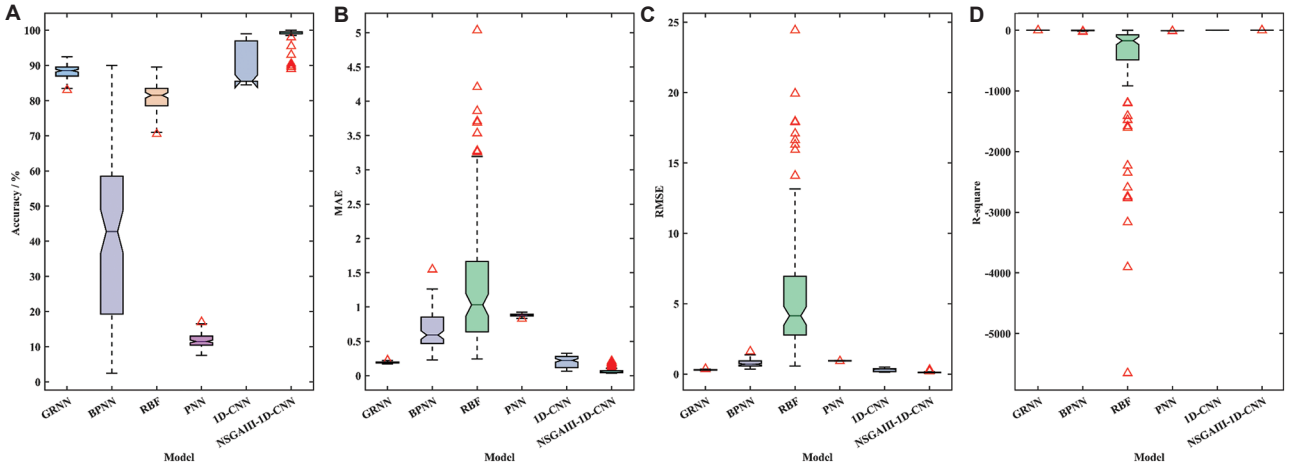

Figure 7. (A-D) Box plot of the prediction results of NSGAIII-1D-CNN compared with other neural network models under 100 rounds of recognition experiments
Abbreviations: 1D-CNN: One-dimensional convolutional neural network; NSGAIII: Non-dominated sorting genetic algorithm III

network models. The median, lower quartile, and upper quartile of the MAE set of the models GRNN, 1D-CNN, and NSGAIII-1D-CNN are all low – all below 0.3 – and there are no large outliers and extreme values; while the recognition performance of the RBF and BPNN models is extremely unstable, with many outliers with MAE exceeding 1.5, and the median and upper quartile both exceeding 0.5; in addition, although the PNN model shows strong recognition stability, and multiple index values are very close – it is far inferior to the NSGAIII-1D-CNN and other models in terms of prediction error.

Figure 7C reveals the RMSE results of 100 rounds of earthquake and explosion identification of six neural network models. The overall performance of the models GRNN, BPNN, 1D-CNN, PNN and NSGAIII-1D-CNN are relatively consistent, and most indicators are <1, proving that most of the predicted regression values of these network models are close to the theoretical label values; however, the RBF model shows significant regression anomalies, with a large number of outliers and large RMSE values. Its narrow and long box also shows that the model has the characteristics of poor stability.

Figure 7D reveals the R-squared results of 100 rounds of earthquake and blast identification for the six neural network models. The overall performance of the models GRNN, BPNN, 1D-CNN, PNN, and NSGAIII-1D-CNN is relatively consistent, and the R-square index is distributed very slightly around zero. However, the RBF model has poor regression interpretation ability for the CEEMDAN-MPE feature set, and its box plot shows a large number of outliers and unusual R-squared minima, which basically indicates that the model does not have good non-linear and non-stationary data processing capabilities.

4.4. Analysis of influencing factors of NSGAIII-1D-CNN model

4.4.1. Neural network training function

The neural network training function, also known as the learning function, is a key computing module in the neural network classification prediction model. It has a certain degree of influence on the accuracy of the precise distinction between earthquakes and explosions and the stability of the model. Common deep learning network training functions include:

(i) SGD-M: The traditional stochastic gradient descent method will oscillate on the steepest descent path. The introduction of momentum can accelerate convergence and suppress oscillation behavior; to minimize the loss function $E(\theta_t)$, the solver makes the iteration move in the negative gradient direction of the loss and updates the weights and biases of the network parameter vector θ in real time, that is, $\theta_{t+1} = \theta_t - \alpha \nabla E\theta_t + \gamma(\theta_t - \theta_{t-1})$, where α and γ are the learning rate and momentum values.

(ii) Root mean square propagation (RMSrop): It performs exponential weighted averaging of the square of the gradient and uses a dynamic learning rate and dynamic loss function that match the gradient size to improve the problem of oscillation convergence of the previous gradient descent method on complex surfaces. It only stores the exponential value of the square of the gradient and is suitable for fast processing of non-stationary targets such as audio.

(iii) Adaptive moment estimation (Adam): It combines the advantages of momentum and RMSrop. It can balance the first-order and second-order moments of the gradient by adaptively adjusting the learning

rate, eliminating oscillations in the update process, converging quickly, and being insensitive to the learning rate. It is suitable for processing large-scale problems such as NLP and time series modeling.

4.4.2. Comparison of prediction effects of NSGAIII-1D-CNN model under different training functions

The experiment in this section is designed as a 20-round cyclic classification experiment. The model is still the NSGAIII-1D-CNN model proposed in this paper. The training set used is fixed to the CEEMDAN-MFE sample set of 1000×11. The parameters of the NSGAIII model, such as population size, maximum number of iterations, crossover percentage, mutation percentage, and mutation rate, are set to 30, 10, 0.5, 0.5, and 0.02, respectively. The parameters of the 1D-CNN model, such as Max Epochs and Learn Rate Drop Period, are set to 50 and 20, respectively. The experimental results are shown in Table 7 and Figure 6.

Table 7 is a statistical table of the calculation results of multiple rounds of earthquake and blasting classification under different network training functions (Net Training Function). It uses the expected mean (Mean) and STD to statistically analyze the error trend and regression effect of multiple rounds of classification results. The specific indicators are accuracy (%), MAE, MBE, R-square, and RMSE. It can be seen from Table 7 that:

(i) From the performance of the STD indicator, the NSGAIII-1D-CNN model using Adam as the training function has stronger classification stability and consistency of prediction results. The STD of its accuracy (%), MAE, MBE, R-square, and RMSE are 1.1391e-16, 0.0109, 0.0105, 0.0272, and 0.0118, respectively; the classification result consistency of the NSGAIII-1D-CNN model with RMSrop as the training function is slightly better than the statistical results of the model using the SGD-M function. The only difference is that the STD value of the MBE indicator is slightly larger. However, considering that the positive and negative deviations of the MBE indicator may offset each other, it is not as accurate as the MAE indicator in reflecting the degree of network prediction error. The performance of the MBE indicator can be ignored here.

(ii) From the perspective of expected mean (Mean), the average prediction accuracy of the NSGAIII-1D-CNN model of the three network training functions is ranked as follows: Adam > SGD-M > RMSrop, among which the performance of each indicator of SGD-M and RMSrop is not much different, that is, the mean deviations of accuracy, MAE, MBE, R-square, and RMSE are 0.625%, 0.0145, 0.0141, 0.1552, and 0.0101, respectively. It is worth noting that the MBE of the RMSrop training function is negative, indicating that the model has a negative bias and underestimation trend.

Figures 6,8-11 are box-plots of the prediction results of multiple rounds of NSGAIII-1D-CNN models under different training functions, which can be used to simultaneously reflect the data discreteness and mathematical statistical information of multiple groups of earthquake and blasting classification results. The upper and lower boundary line indicators of the box in the figure represent the upper quartile (Q3) and lower quartile (Q1) of the positioning results, respectively. The solid line in the box represents the median of the positioning results. The "+" marked data is judged as an abnormal point by the box plot. The horizontal solid lines distributed above and below the box represent the maximum and minimum values, respectively.

Figure 8 reveals the prediction accuracy results of 20 rounds of NSGAIII-1D-CNN model for three training functions. Among them, the classification performance of earthquake and explosion of the training function "Adam" is relatively good, without obvious outliers and calculation divergence; the classification result of the training function "RMSprop" has one outlier, and its accuracy value is below 88%, which is almost 10 percentage points lower than the classification average of 97.8750%, indicating that there is a large room for improvement in the stability of its model;

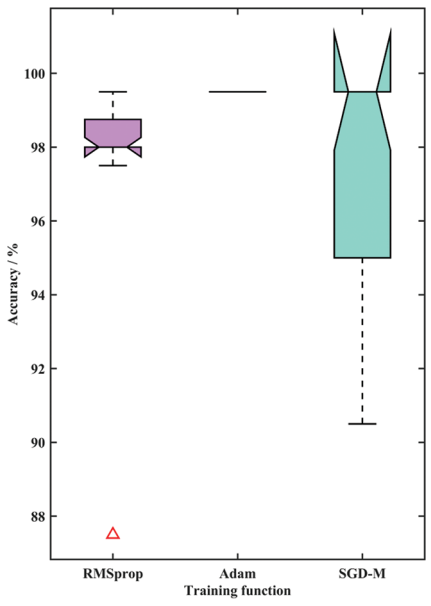

Figure 8. Box plot of prediction accuracy results of the multi-round NSGAIII-1D-CNN model with different training functions
Abbreviations: 1D-CNN: One-dimensional convolutional neural network; NSGAIII: Non-dominated sorting genetic algorithm III

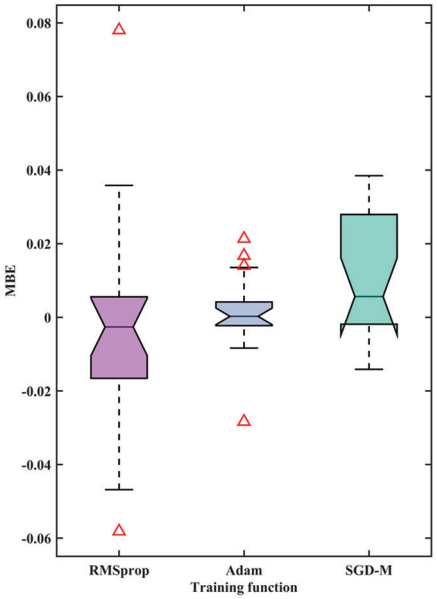

Figure 9. Box plot of predicted MBE results of the multi-round NSGAIII-1D-CNN model with different training functions
Abbreviations: 1D-CNN: One-dimensional convolutional neural network; Adam: Adaptive moment estimation; MBE: Mean squared error; NSGAIII: Non-dominated sorting genetic algorithm III; RMSrop: Root mean square propagation; SGD-M: Stochastic gradient descent with momentum

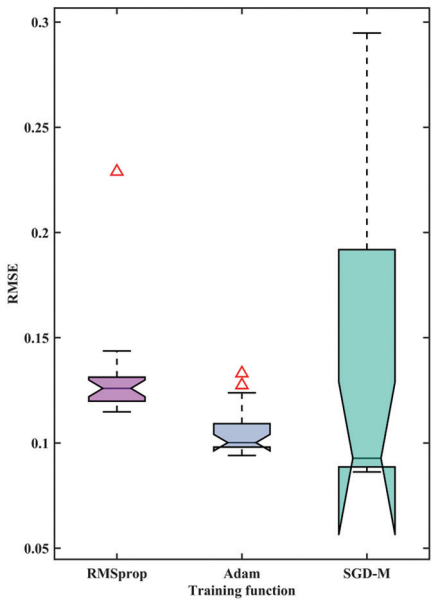

Figure 10. Box plot of predicted RMSE results of multi-round NSGAIII–1D-CNN model with different training functions
Abbreviations: 1D-CNN: One-dimensional convolutional neural network; Adam: Adaptive moment estimation; NSGAIII: Non-dominated sorting genetic algorithm III; RMSE: Root mean squared error; RMSrop: Root mean square propagation; SGD-M: Stochastic gradient descent with momentum

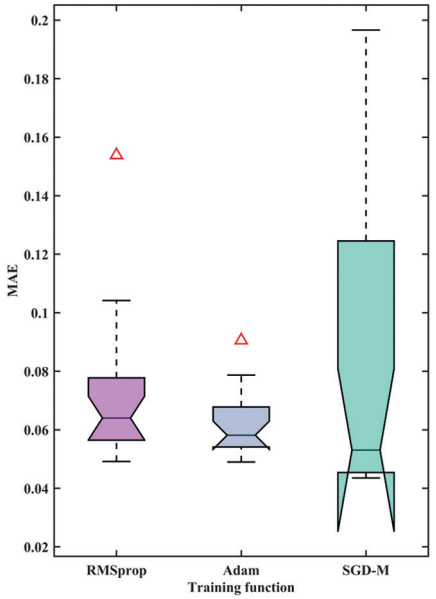

Figure 11. Box plot of predicted MAE results of the multi-round NSGAIII-1D-CNN model with different training functions
Abbreviations: 1D-CNN: One-dimensional convolutional neural network; Adam: Adaptive moment estimation; MAE: Mean absolute error; NSGAIII: Non-dominated sorting genetic algorithm III; RMSrop: Root mean square propagation; SGD-M: Stochastic gradient descent with

the classification result of the training function "SGD-M" has no outliers, but its IQR exceeds 4%, and its minimum value is very close to 90%, indicating that there is still room for improvement to a certain extent.

Figure 9 reveals the MBE results predicted by the NSGAIII-1D-CNN model for 20 rounds of three training functions. The classification results of the training function "Adam" tend to be biased and balanced, with the median of its box plot close to 0 and the IQR value within 0.01, indicating that the model has no significant positive or negative error bias. The classification results of the training function "RMSprop" have two MBE outliers, and the IQR value exceeds 0.02, showing a certain degree of negative bias. The IQR value of the box plot of the training function "SGD-M" reaches 0.03, and the position of the median shows that the model prediction shows an obvious positive bias.

Figure 6 reveals the R-square results predicted by the NSGAIII-1D-CNN model for 20 rounds of three training functions. The median and IQR values in the box plots of the training function "Adam" and the training function "RMSprop" are slightly different, and both the median and mean are greater than 0.8, indicating that both have strong model regression explanatory power in terms of the R-squared indicator. The IQR value of the box plot

of the training function "SGD-M" exceeds 0.4, and the minimum value is close to 0, reflecting that the calculation performance of this function is highly unstable.

Figure 10 reveals the RMSE results of 20 rounds of NSGAIII-1D-CNN model predictions for three training functions. The RMSE values of the prediction results of the training functions "Adam" and "RMSprop" both showed abnormal outliers, and the IQR value and the median of the box plot of the former were slightly smaller than those of the latter. The IQR value of the box plot of the training function "SGD-M" exceeded 0.1, and the maximum RMSE tended to 0.3, revealing that the prediction results of the NSGAIII-1D-CNN model using this function as the training function generally had large errors and unstable performance.

Figure 11 reveals the MAE results of 20 rounds of NSGAIII-1D-CNN model predictions for three training functions. The median MAE of the multi-round prediction results of the training function "Adam" tends to 0.06, its IQR value is also less than 0.02, and the only outlier is also less than 0.1, which proves that the training function can better minimize the deviation between the network prediction value and the theoretical value; the classification result of the training function "RMSprop" has a slightly larger MAE outlier, and its IQR value and the median of the box plot are slightly larger than "Adam"; the IQR value and maximum value of the box plot of the training function "SGD-M" are close to 0.08 and 0.2, respectively. Although the median is slightly smaller than that of the other two training functions, it is not enough to make up for the defect of the large prediction error of this training function.

5. Discussion

This study achieved an average recognition accuracy of 97.82% on 1000 sets of measured data (883 earthquakes and 117 explosions) through the innovative combination of CEEMDAN-MFE and NSGAIII-1D-CNN. This achievement is mainly due to three key technical breakthroughs:

CEEMDAN decomposition uses an optimized parameter combination of noise STD 0.2 and 24 noise additions, combined with a dynamically decreasing noise coefficient, to effectively solve the modal aliasing problem of traditional EMD. This method successfully decomposes earthquake and explosion signals into 11 IMF components with clear physical meanings, laying a solid foundation for subsequent feature extraction.

MFE feature extraction selects the optimal parameter combination of $m = 2$, $r = 0.2$, and $n = 2$, and constructs a highly discriminative feature matrix by calculating the entropy values of the first 8 IMF components (excluding the last three low-frequency noise-dominated components). The data in Table 2 shows that this feature set makes the NSGAIII-1D-CNN model have an MAE as low as 0.0795 and an R^2 of 0.7361 in 100 rounds of random experiments, which is significantly better than the comparison model.

The NSGAIII optimization stage sets the population size to 50 and the maximum iteration to 50 generations, and optimizes the hyperparameters of 1D-CNN through dual objectives (minimizing MBE and maximizing R^2). This strategy enables the model to control the RMSE to 0.1302 whereas maintaining an average accuracy of 97.82%. When the Adam optimizer is used, the peak performance of the model can reach 99.5%, which has obvious advantages over SGD-M and RMSprop.

The end-to-end delay of the current model for completing a single recognition on standard hardware (Intel i7) is 200 ms, of which CEEMDAN-MFE feature extraction accounts for 60%. Through technologies such as model quantization, the memory usage has been compressed to 8.7 MB, meeting the deployment requirements of edge devices. In terms of practical applications, the current system has two main limitations: first, the recognition accuracy of signals with a signal-to-noise ratio below 5 dB will drop by about 15%, which is mainly due to the interference of noise on the MFE calculation; second, although the window of 4000 sampling points can maintain feature integrity during real-time processing, it increases the delay by about 200 ms. However, the system still maintains an accuracy rate of more than 90% in tests in different regions such as Qinghai and Sichuan, proving that it has strong environmental adaptability.

The comparison with existing technologies highlights the value of this study: compared with traditional 1D-CNN (89.82% accuracy) and GRNN (88.15%), the accuracy of this model is improved by 8–10 percentage points; in terms of regression indicators, MAE (0.0795) is reduced by more than 60% compared with the comparison model. These improvements are reflected in more reliable recognition performance in actual monitoring, such as successfully distinguishing 97.3% of blasting interference events in the 2023 Luding aftershock sequence.

Future research will be deepened in three directions: first, develop a dynamic adjustment mechanism for CEEMDAN parameters with adaptive signal-to-noise ratio to improve stability under extremely low signal-to-noise ratio; second, deploy a chip-level online learning system to achieve continuous optimization of model parameters; third, integrate multimodal data of geological environment to build a more interpretable intelligent discrimination

system. These improvements will further enhance the applicability and reliability of this technology in actual earthquake monitoring scenarios.

6. Conclusion

This study proposes a hybrid prediction model that integrates CEEMDAN-MFE feature extraction and NSGAIII-optimized 1D-CNN. Through theoretical innovation and technological breakthroughs, the recognition accuracy and model stability of earthquake and explosion events are significantly improved. Experimental verification based on 1000 measured signals shows that the proposed CEEMDAN-MFE feature extraction method can effectively capture the essential differences in the non-linear dynamic characteristics of earthquake and explosion signals, and the constructed feature matrix significantly enhances the pattern separability of the signal. The 1D-CNN model optimized by NSGAIII multi-objective achieved an average accuracy of 97.82% in 100 rounds of random experiments. All performance indicators were significantly better than those of the traditional neural network model, verifying the synergistic advantages of the network structure and automatic optimization of hyperparameters. Despite the remarkable research results, this study still has limitations such as limited data coverage, the need to improve the accuracy of microseismic signal recognition, and the need to optimize edge computing efficiency. Based on the current research foundation, future work will focus on in-depth research on cross-regional generalization verification, model lightweight design, and multimodal data fusion. By constructing a larger-scale multi-tectonic belt data set, developing a compression algorithm based on knowledge distillation, and integrating waveform data with geological environment parameters, the practicality and generalization ability of the model will be further improved. This study not only provides a new technical solution for the field of earthquake monitoring, but its innovative research methodology also provides a useful reference for other time-varying signal processing fields, which has important theoretical value and practical significance.

Acknowledgments

None.

Funding

This research was financially supported by Mahasarakham University; Open Fund of Wuhan Gravitation and Solid Earth Tides, National Observation and Research Station, (No.WHYWZ202406, WHYWZ202208); Scientific Research Fund of Institute of Seismology, China Earthquake Administration and National Institute of Natural Hazards, MEM, (No. IS202236328, IS202436357); The Spark Program of Earthquake Technology of CEA, (No. XH24025YC); Earthquake Monitoring and Forecasting and Early Warning Tasks for 2025, (No. CEA-JCYJ-202502015); Chengdu Jincheng College Green Data Integration Intelligence Research and Innovation Project (No. 2025-2027); and the High-Quality Development Research Center Project in the Tuojiang River Basin (No. TJGZL2024-07).

Conflict of interest

The authors declare they have no competing interests.

Author contributions

Conceptualization: Cong Pang, Tianwen Zhao, Pornntiwa Pawara

Formal analysis: Cong Pang, Guoqing Chen, Piyapatr Busababodhin, Pornntiwa Pawara

Investigation: Piyapatr Busababodhin, Chawei Li, Zhongya Li, Pornntiwa Pawara

Methodology: Cong Pang, Tianwen Zhao, Guoqing Chen, Chawei Li, Zhongya Li

Writing–original draft: Cong Pang, Tianwen Zhao, Guoqing Chen, Pornntiwa Pawara

Writing–review & editing: Cong Pang, Tianwen Zhao, Guoqing Chen, Pornntiwa Pawara

Availability of data

This study integrates 1000 sets of strong earthquake observation data and explosion data from various regions in and around China, mainly from earthquake case data publicly shared by the National Earthquake Data Center (NEDC, data.earthquake.cn), the Institute of Engineering Mechanics of the China Earthquake Administration (IEM, CEA) and China Institute of Water Resources and Hydropower Research (CIWHR).

References

1. Johnson JA, Mutchnick AB. Identification of wall tension fractures caused by earthquakes, blasting, and pile driving. *Environ Eng Geosci*. 2016;22(2):131-139.

   doi: 10.2113/gseegeosci.22.2.131

2. Dong LJ, Wesseloo J, Potvin Y. Discriminant models of blasts and seismic events in mine seismology. *Int J Rock Mech Min Sci*. 2016;86:282-291.

   doi: 10.1016/j.ijrmms.2016.04.021

3. Lythgoe K, Loasby A, Hidayat D, Wei S. Seismic event detection in urban Singapore using a nodal array and frequency domain array detector: Earthquakes, blasts, and thunder quakes. *Geophys J Int*. 2021;226(3):1542-1557.

doi: 10.1093/gji/ggab135

4. Saad M, Soliman MS, Chen Y, Amin AA, Abdelhafiez HE. Discriminating earthquakes from quarry blasts using capsule neural network. *IEEE Geosci Remote Sens Lett*. 2022;19:1-5.

   doi: 10.1109/LGRS.2022.3207238

5. Wang S, Hu Y, Chen H, Chen X. An energy-concentrated transform for improved time-frequency representation of seismic signals. *IEEE Signal Process Lett*. 2025;32:2084-2088.

   doi: 10.1109/LSP.2025.3565164

6. Rivera E, Ruiz S, Madariaga R. Spectrum of strong-motion records for large magnitude Chilean earthquakes. *Geophys J Int*. 2021;226(2):1045-1057.

   doi: 10.1093/gji/ggab128

7. Mei W, Li M, Pan PZ, Pan J, Liu K. Blasting induced dynamic response analysis in a rock tunnel based on combined inversion of Laplace transform with elasto-plastic cellular automaton. *Geophys J Int*. 2020;225(1):699-710.

   doi: 10.1093/gji/ggaa615

8. Matsushima M, Honkura Y, Kuriki M, Ogawa Y. Circularly polarized electric fields associated with seismic waves generated by blasting. *Geophys J Int*. 2013;194(1):200-211.

   doi: 10.1093/gji/ggt110

9. Xiao Y, Guo J, Chen S, Liu L, Chen B. Digitalization of rock fracture signal identification from tunnel microseismic data. *IEEE Geosci Remote Sens Lett*. 2024;21:1-5.

   doi: 10.1109/LGRS.2024.3399271

10. Zhou J, Ba J, Castagna JP, Guo Q, Yu C, Jiang R. Application of an STFT-based seismic even and odd decomposition method for thin-layer property estimation. *IEEE Geosci Remote Sens Lett*. 2019;16(9):1348-1352.

    doi: 10.1109/LGRS.2019.2901261

11. Geetha K, Hota MK. Seismic random noise attenuation using optimal empirical wavelet transform with a new wavelet thresholding technique. *IEEE Sens J*. 2024;24(1):596-606.

    doi: 10.1109/JSEN.2023.3334819

12. Alvanitopoulos PF, Papavasileiou M, Andreadis I, Elenas A. Seismic intensity feature construction based on the Hilbert-Huang transform. *IEEE Trans Instrum Meas*. 2012;61(2):326-337.

    doi: 10.1109/tim.2011.2161934

13. Chen CH, Wang CH, Liu JY, Liu C, Liang WT, Yen HY. Identification of earthquake signals from groundwater level records using the HHT method. *Geophys J Int*. 2010;180(3):1231-1241.

    doi: 10.1111/j.1365-246X.2009.04473.x

14. Küperkoch L, Meier T, Lee J, Friederich W. Automated determination of P-phase arrival times at regional and local distances using higher order statistics. *Geophys J Int*. 2010;181(2):1159-1170.

    doi: 10.1111/j.1365-246X.2010.04570.x

15. Zhu J, Zhou Y, Liu H, *et al*. Rapid earthquake magnitude classification using single station data based on machine learning. *IEEE Geosci Remote Sens Lett*. 2024;21:1-5.

    doi: 10.1109/lgrs.2023.3346655

16. Samal P, Hashmi MF. Ensemble median empirical mode decomposition for emotion recognition using EEG signal. *IEEE Sens Lett*. 2023;7(5):1-4.

    doi: 10.1109/lsens.2023.3265682

17. Chen J, Heincke B, Jegen M, Moorkamp M. Using empirical mode decomposition to process marine magnetotelluric data. *Geophys J Int*. 2012;190(1):293-309.

    doi: 10.1111/j.1365-246X.2012.05470.x

18. Li B, Huang H, Wang T, Wang M, Wang P. Research on Seismic Signal Classification and Recognition Based on EEMD and CNN. Presented at: *2020 IEEE 3rd International Conference on Electronics and Communication Engineering (ICECE)*. Shenzhen, China; 2020. p. 83-88.

    doi: 10.1109/ICECE51594.2020.9353037

19. Zhang D, Wang Y, Zhu T, Ma GW. Mode identification method of long span steel bridge based on CEEMDAN and SSI algorithm. *Earthquake Eng Resil*. 2024;3(3):388.

    doi: 10.1002/eer2.89

20. Wu S, Guo H, Zhang X, Wang F. Short-term photovoltaic power prediction based on CEEMDAN and hybrid neural networks. *IEEE J Photovolt*. 2024;14(6):960-969.

    doi: 10.1109/jphotov.2024.3453651

21. Wang J, Dai B, Zhang T, Qi L. A novel hybrid model of CEEMDAN-CNN-SAGU for Shanghai copper price prediction. *IEEE Access*. 2024;12:25176-25187.

    doi: 10.1109/access.2024.3365558

22. Tian S, Bian X, Tang Z, Yang K, Li L. Fault diagnosis of gas pressure regulators based on CEEMDAN and feature clustering. *IEEE Access*. 2019;7:132492-132502.

    doi: 10.1109/ACCESS.2019.2941497

23. Li J, Yao R. Field deployment of natural gas pipeline pre-warning system with CEEMDAN denoising method. *IEEE Photon J*. 2024;16(4):1-8.

    doi: 10.1109/JPHOT.2024.3421275

24. Pan L, Liu M, Chen R, Ma S. Research on Seismic Signal Identification and Magnitude Prediction Model Based on Sample Entropy and Machine Learning. Presented at: 2024 *IEEE 2nd International Conference on Sensors, Electronics and Computer Engineering (ICSECE)*. Beijing, China; 2024. p. 1586-1592.

    doi: 10.1109/icsece61636.2024.10729556

25. Aggarwal M. Bridging the gap between probabilistic and fuzzy entropy. *IEEE Trans Fuzzy Syst*. 2020;28(9):2175-2184.

doi: 10.1109/TFUZZ.2019.2931232

26. Ali M, Nathwani K. Exploiting wavelet scattering transform and 1D-CNN for unmanned aerial vehicle detection. *IEEE Signal Process Lett*. 2024;31:1790-1794.

doi: 10.1109/LSP.2024.3421961

27. Kail R, Burnaev E, Zaytsev A. Recurrent convolutional neural networks help to predict location of earthquakes. *IEEE Geosci Remote Sens Lett*. 2022;19:1-5.

doi: 10.1109/lgrs.2021.3107998

28. Sivanjaneyulu Y, Manikandan MS, Boppu S, Cenkeramaddi LR. Resource-efficient derivative PPG-based signal quality assessment using one-dimensional CNN with optimal hyperparameters for quality-aware PPG analysis. *IEEE Access*. 2024;12:141251-141267.

doi: 10.1109/access.2024.3464231

29. Perera S, Witharana C, Manos E, Liljedahl AK. Hyperparameter optimization for large-scale remote sensing image analysis tasks: A case study based on permafrost landform detection using deep learning. *IEEE Access*. 2024;12:43062-43077.

doi: 10.1109/ACCESS.2024.3379142

30. Wang Y, Wang Y, Jiang K, Zheng W, Song M. Adaptive grid search-based pulse phase and Doppler frequency estimation for XNAV. *IEEE Trans Aerosp Electron Syst*. 2024;60(3):3707-3717.

doi: 10.1109/TAES.2024.3361431

31. Ren L, Li Y, Zhou S. An improved NSGA-III algorithm for scheduling ships arrival and departure at the main channel of Tianjin Port. *IEEE Access*. 2024;12:131442-131457.

doi: 10.1109/access.2024.3457526

32. Srinivas N, Deb K. Muiltiobjective optimization using nondominated sorting in genetic algorithms. *Evol Comput.* 1994;2(3):221-248.

doi: 10.1162/evco.1994.2.3.221

33. Deb K, Pratap A, Agarwal S, Meyarivan TAMT. A fast and elitist multiobjective genetic algorithm: NSGA-II. *IEEE Trans Evol Comput.* 2002;6(2):182-197.

doi: 10.1109/4235.996017

34. Deb K, Jain H. An evolutionary many-objective optimization algorithm using reference-point-based nondominated sorting approach, part I: solving problems with box constraints. *IEEE Trans Evol Comput*. 2013;18(4):577-601.

doi: 10.1109/TEVC.2013.2281535

ACCSCIENCE PUBLISHING

Journal of Seismic Exploration

ARTICLE

Multi-stage progressive network for seismic random noise suppression

Guanghui Li*, Huiwei Li, Shoufeng He, and Li Wang

Department of Electronic Information Engineering, College of Physics and Electronic Engineering, Shanxi University, Taiyuan, Shanxi, China

Abstract

Seismic data quality frequently deteriorates due to random noise contamination, substantially impeding subsequent processing and geological interpretation. While deep learning approaches have emerged as powerful tools for noise suppression, conventional single-stage architectures exhibit inherent limitations in handling complex seismic features while preserving subtle geological details. These challenges motivate the development of advanced multi-stage neural networks for seismic data enhancement. The proposed multi-stage progressive U-shaped convolutional network (MPU-Net) architecture addresses these limitations through supervised cross-stage attention mechanisms that maintain feature connectivity throughout the network. Building upon this foundation, group enhanced convolutional blocks (GEB)-MPU-Net introduces GEB to specifically counteract the progressive attenuation of shallow features in deep networks. This dual-stage enhancement strategy combines hierarchical feature preservation, adaptive information fusion, and stable gradient propagation. Comprehensive evaluation using both synthetic and field datasets demonstrates GEB-MPU-Net's superior performance compared to conventional time-frequency analysis methods and established networks, such as U-Net, residual dense network, residual dense block U-Net, and MPU-Net. The architecture consistently achieves enhanced reflection continuity, improved geological feature resolution, and robust noise suppression. These advancements provide more reliable input for seismic interpretation, better preservation of subtle stratigraphic features, and increased applicability to challenging field conditions.

Keywords: Noise suppression; Deep learning; Multi-stage networks; Seismic exploration

***Corresponding author:**
Guanghui Li
(ligh1986@sxu.edu.cn)

Citation: Li G, Li H, He S, Wang L. Multi-stage progressive network for seismic random noise suppressing. *J Seismic Explor.* 2025;34(1): 43-59. doi: 10.36922/JSE025240011

Received: June 10, 2025

1st revised: July 22, 2025

2nd revised: July 26, 2025

Accepted: August 6, 2025

Published online: August 14, 2025

1. Introduction

The focus of seismic exploration has progressively transitioned to complex structural traps, deep-buried reservoirs, and unconventional hydrocarbon systems as conventional resources become increasingly depleted. This evolution demands seismic data of substantially improved quality. Nevertheless, field-acquired seismic records are invariably contaminated by ambient noise originating from diverse environmental and operational factors, significantly compromising both subsurface imaging resolution and geological interpretation accuracy. Consequently, noise suppression and signal-to-noise ratio (SNR) enhancement remain fundamental challenges in modern seismic data processing.

Traditional seismic denoising approaches primarily rely on mathematical transformations and filtering techniques, including Fourier transforms,[1] wavelet transforms,[2] Curvelet transforms,[3,4] Seislet transforms,[5] empirical mode decomposition,[6] variational mode decomposition,[7,8] low-rank approximation,[9] compressed sensing,[10] and dictionary learning.[11] Although these methods have proven effective for certain types of noise, they exhibit several inherent limitations. A primary challenge lies in their limited adaptability to handle diverse noise distributions, particularly in complex geological settings or unconventional reservoirs. Furthermore, their performance typically depends on manual parameter tuning, which may lead to suboptimal results when processing conditions vary.

Recent advances in artificial intelligence have established neural networks as powerful tools for seismic data denoising, offering substantial improvements over conventional approaches. In particular, deep convolutional neural networks[12,13] and their numerous enhanced algorithms demonstrate superior performance in both seismic noise suppression and signal preservation, exhibiting enhanced robustness to noise variability and improved generalization across diverse geological settings compared to traditional transform-based methods, such as the self-supervised framework,[14] the modular convolutional neural network that incorporates multi-scale attention mechanisms,[15] the singular value decomposition combined with deep learning,[16] the residual dense blocks integrated with time-frequency analysis,[17] and the advanced U-shaped convolutional network (U-Net) architectures through Atropos convolutions and dense connections.[18,19]

However, these single-stage architectures frequently exhibit suboptimal trade-offs between multi-scale representation and spatial precision when processing field seismic data, particularly in scenarios involving complex noise distributions, low SNR, and subtle geological features. Recent developments in seismic denoising have seen the emergence of multi-stage unsupervised and self-supervised deep learning approaches. For instance, the multi-stage progressive U-Net (MPU-Net),[20] the self-supervised multi-stage network,[21] and the two-step deep image prior model.[22] These methods significantly reduce reliance on annotated training data while demonstrating robust performance across varied noise conditions. Nevertheless, the lack of explicit supervisory signals presents inherent limitations, particularly in reliably differentiating subtle seismic reflections from background noise and maintaining stable performance under diverse geological settings.

Based on this, we present a novel group enhanced convolutional blocks (GEB) MPU-Net (GEB-MPU-Net) architecture for seismic data denoising, which innovatively integrates GEB[23] within the MPU-Net framework. This synthesis enhances feature representation while maintaining the structural advantages of progressive processing. GEB significantly improves multi-scale feature integration through its unique combination of residual learning and grouped feature extraction. By incorporating channel attention blocks (CABs), the architecture further enhances long-range feature propagation and representation, leading to more stable and effective seismic denoising. This design achieves comprehensive feature fusion through systematic GEB-CAB integration at each processing stage. The framework strengthens low-frequency feature representation through inter-channel correlation analysis while implementing signal enhancement mechanisms to maintain critical long-range dependencies. Importantly, this approach successfully resolves the persistent shallow information loss problem inherent in conventional MPU-Net architectures.

Compared to other multi-stage unsupervised and self-supervised deep learning approaches,[22-25] first, GEB-MPU-Net's tight integration with multi-stage supervised learning enables precise feature optimization through explicit signal-noise differentiation. This coupled framework systematically enhances discriminative feature extraction while preserving structural relationships across processing stages. Second, the GEB module incorporates a specialized channel attention mechanism designed to optimize shallow-deep feature integration and enhance low-frequency representation. This tailored architecture enables GEB-MPU-Net to surpass conventional unsupervised approaches employing standard attention modules, demonstrating superior denoising robustness and generalization capacity. The processing results of synthetic and field seismic data both demonstrate their superior performance and signal fidelity, particularly in complex and challenging environments. Overall, GEB-MPU-Net represents a dual advancement in seismic denoising methodology, introducing both architectural innovations and demonstrable improvements in signal preservation. The framework surpasses existing approaches through its integrated design, achieving superior noise suppression while maintaining critical geological features.

2. Algorithm principle

2.1. U-shaped convolutional network structure

U-shaped convolutional network's symmetric encoder-decoder framework utilizes cross-connection pathways to maintain its characteristic U-topology while enabling multi-scale feature integration. Figure 1 presents the standard implementation of this architecture. The first

half of the network focuses on feature extraction, while the latter half emphasizes up-sampling. Specifically, the encoding section employs a series of 3 × 3 convolutional layers, rectified linear unit (ReLU) activation functions, and 2 × 2 max pooling layers to extract features from the input image. With each down-sampling operation, the dimensions of the feature maps are halved, while the number of channels is doubled. The primary function of the decoding section is to utilize transposed convolutional layers to reconstruct high-resolution representations from the encoded low-resolution features. Skip connections between the contracting and expanding channels facilitate the fusion of low-resolution and high-resolution features, enabling a more effective capture of both local and global characteristics of the image.

2.2. MPU-Net structure

As shown in Figure 2, the network employs a multi-patch hierarchical decomposition strategy, where input seismic data undergoes non-overlapping patch segmentation. This preprocessing stage enables localized feature extraction while maintaining structural relationships across spatial domains. It implements the strategy across three progressive stages: initial coarse segmentation into

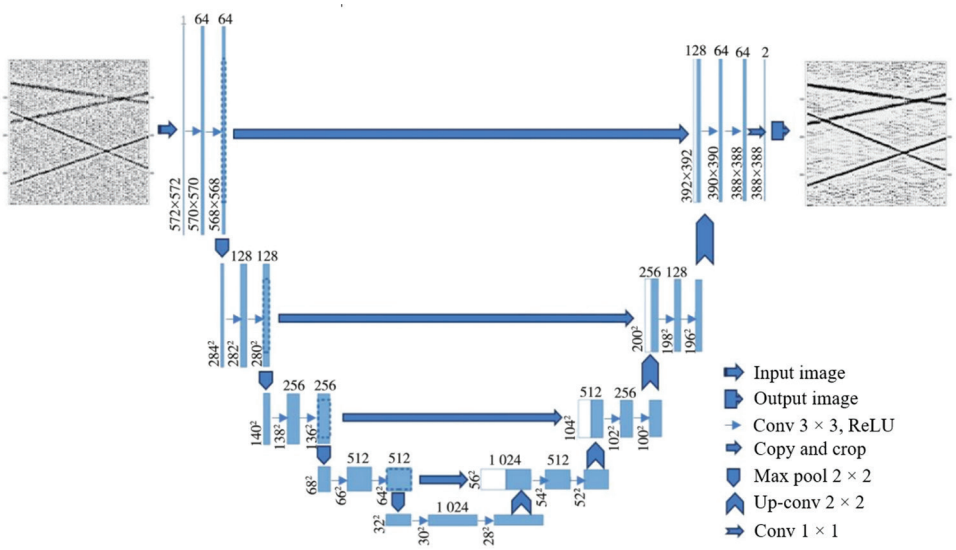

Figure 1. Structure of a U-shaped convolutional network
Abbreviations: conv: Convolution; ReLU: Rectified linear unit

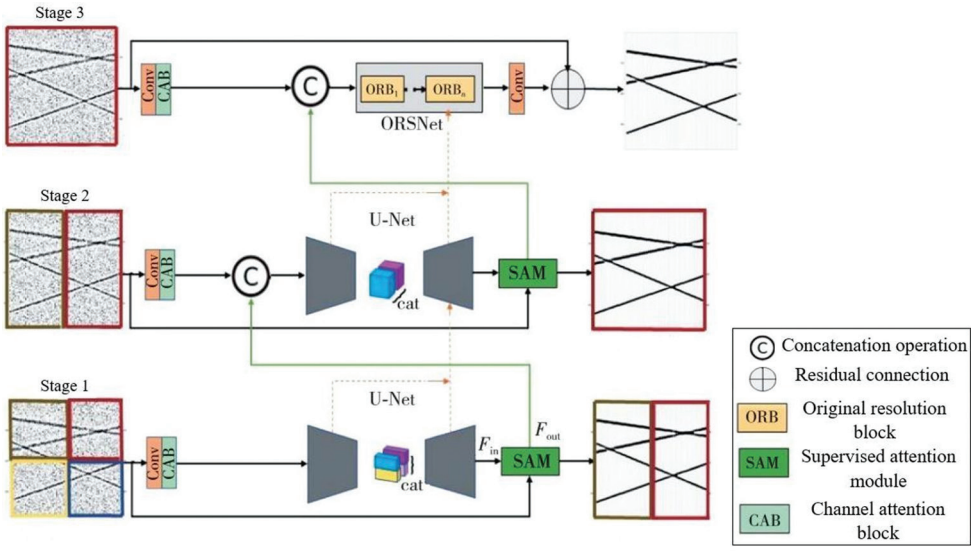

Figure 2. Multi-stage progressive U-Net structure
Abbreviations: cat: Concatenate; Conv: Convolution; ORSNet: Original resolution subnetwork; U-Net: U-shaped convolutional network

four patches, intermediate division into two patches, and final processing of the full-resolution input. The initial processing stages implement an enhanced U-Net framework, where each encoder-decoder level incorporates dual CABs. This design enables efficient multi-scale feature extraction while maintaining spatial relationships across different resolution levels. The attention mechanisms selectively emphasize informative channels, optimizing feature representation throughout the network hierarchy. Conventional transposed convolution operations in U-Net decoders frequently generate checkerboard artifacts due to uneven kernel overlap patterns. These artifacts manifest as spurious seismic events in processed records, particularly adjacent to genuine reflections, potentially compromising interpretation accuracy. This phenomenon motivates the development of more stable up-sampling alternatives for seismic data restoration. To mitigate this limitation, MPU-Net modifies the conventional U-Net architecture by implementing bilinear interpolation for up-sampling, coupled with subsequent convolutional layers for spatial feature restoration. This adaptation reduces artifacts while maintaining resolution fidelity during the decoding phase. The original resolution subnetwork (ORSNet) consists of three original resolution blocks, which are connected to the input in the third stage.

Figure 3 illustrates the original resolution block module's composition, featuring eight CABs integrated with a final convolutional layer. The CAB consists of four 3×3 convolutional layers, one global average pooling layer, and three activation functions designed to enhance the representational capability of valuable features. Since ORSNet does not perform down-sampling, it retains high-resolution spatial details. As indicated by the dashed lines in Figure 2, the three stages are not independent; rather, a supervised attention module (SAM) is incorporated between each pair of stages to weigh the significant features. These features are then closely cascaded through a cross-stage feature fusion (CSFF) process. While all other convolutional layers in the MPU-Net architecture are 3×3, the convolutional layers in the SAM and CSFF are 1×1.

Cross-stage feature fusion mechanisms are introduced between the U-Net of the first and second stages, as well as between the U-Net of the second stage and the ORSNet of the third stage, as illustrated separately in Figure 4.

The architecture processes encoder and decoder outputs through parallel 1×1 convolutional layers for dimensional refinement and feature conditioning. These optimized feature maps subsequently undergo cross-level fusion, creating an enriched representation for stage-transition processing. This dual-path approach maintains feature integrity while enabling information exchange across network depths. The CSFF mechanism enables systematic integration of multi-scale features throughout the network hierarchy. This architecture provides three key advantages: (i) Preservation of critical information across processing stages, (ii) enhanced model robustness through diversified feature representation, and (iii) flexible network optimization via adjustable stage connectivity. The improved inter-stage information flow additionally facilitates architectural diagnostics and stage-number optimization during network development.

A SAM, illustrated in Figure 5, is integrated at the end of each encoder-decoder sub-network during the first two stages.

The SAM module processes incoming features through a 1×1 convolutional operation to produce residual representations. The network utilizes the learned residual representations to systematically attenuate noise components in the input seismic data. The processed seismic data undergoes feature optimization through a 1×1 convolutional layer with sigmoidal activation.

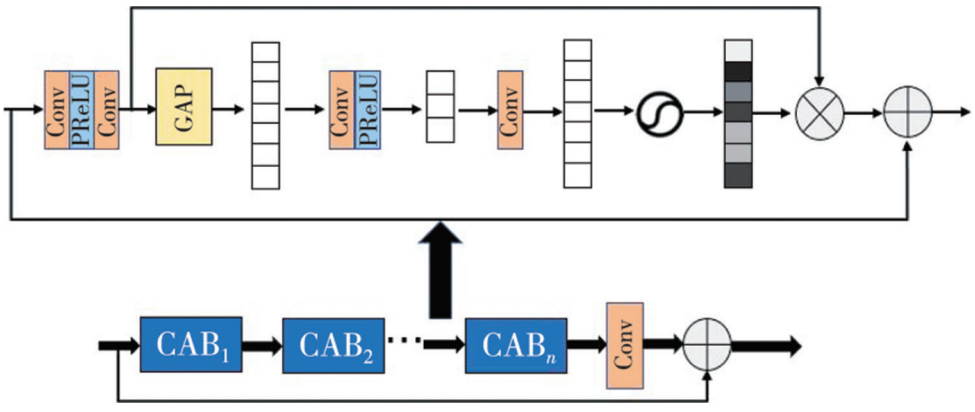

Figure 3. Structure of the original resolution block
Abbreviations: CAB: Channel attention block; Conv: Convolution; GAP: Global average pooling; PReLU: Parametric rectified linear unit

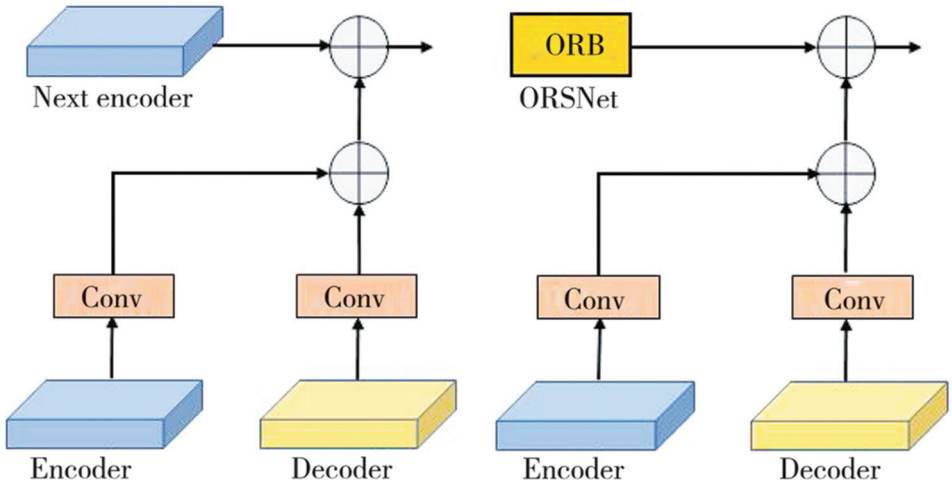

Figure 4. Structure of CSFF. (A) CSFF between stage 1 and 2; (B) CSFF between stage 2 and 3
Abbreviations: Conv: Convolution; CSFF: Cross-stage feature fusion; ORB: Original resolution block; ORSNet: Original resolution subnetwork

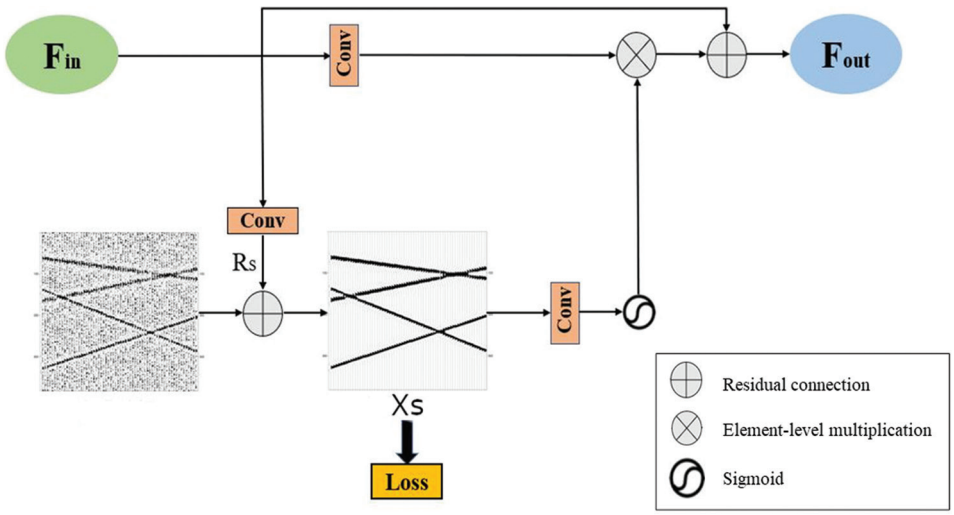

Figure 5. Structure of a supervised attention module
Abbreviations: Conv: Convolution; F_{in}: Input feature; F_{out}: Output feature; Rs: Residual representation; Xs: Input seismic feature

This operation performs channel-wise feature rescaling, suppression of non-informative components, and selective propagation of geophysically valid features. This gating mechanism ensures only the most salient signal characteristics propagate through the network hierarchy, substantially improving the denoising efficacy while maintaining geological plausibility. The three stages are tightly integrated through the SAM and CSFF, leveraging feature information extracted from each stage to achieve improved learning outcomes.

2.3. GEBs module structure

Figure 6 illustrates the structure of the GEB. The block comprises two components: the known extraction portion (GConv1), which encompasses one-fifth of the feature channels from the current convolutional layer, and the remaining portion (GConv2), which includes four-fifths of the feature channels from the same layer. In each GEB, GConv1 serves as a convolutional layer with 16 input channels, 16 output channels, and a filter size of 3 × 3, whereas GConv2 has an input and output channel count of 60, also utilizing a 3 × 3 filter size. The remaining portion is utilized as the input for the subsequent convolutional layer in the main network, facilitating the extraction of additional deep features.

To enhance the expressiveness of low-frequency features, the GEB module employs a fusion mechanism between every two adjacent GConv2 layers. Specifically,

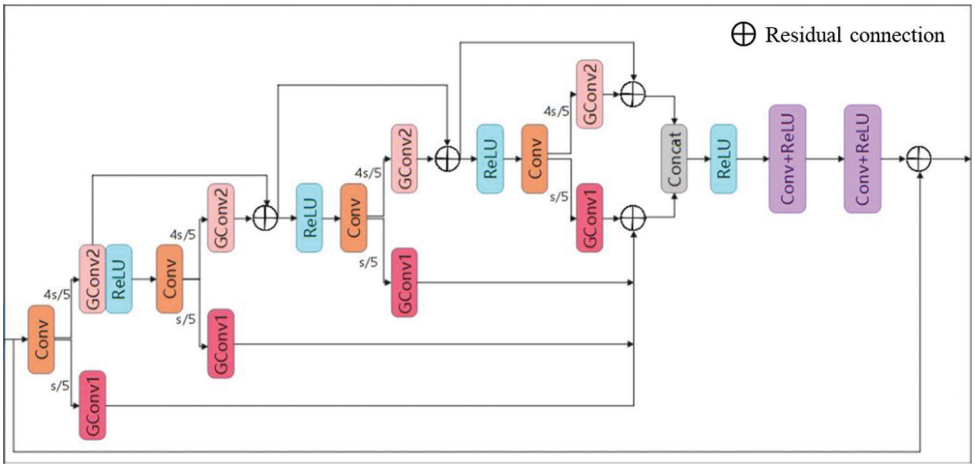

Figure 6. Structure of the group enhanced convolutional blocks
Abbreviations: Concat: Concatenation operation; Conv: Convolution; GConv1: Known extraction portion; GConv2: Remaining portion; ReLU: Rectified linear unit

for each pair of consecutive GConv2 layers within the GEB, their outputs are combined using a residual connection (Figure 6). This process enables the network to effectively aggregate deep neighborhood information across layers, thereby capturing broader contextual dependencies and improving the representation of low-frequency features. The network architecture establishes progressive feature interdependence, where each subsequent extraction module builds upon transformed representations from preceding stages. It provides two key advantages, including cascading information refinement through the network depth and complementary broad-context supplementation to deep features. The resulting multi-scale integration enhances denoising performance by simultaneously preserving both local details and global seismic characteristics. The feature processing within the GEB can be categorized into the following four steps[21]:

(i) Step 1. To enhance the features of neighboring layers and improve the accuracy of deep features across various channels, the features from two adjacent GConv2 layers are fused using a residual learning strategy. This combined information is subsequently fed into the next convolutional layer. While the outputs of the later GConv1 layers are derived from the preceding GConv2 layers, the output of the first GConv1 is derived from one-fifth of the output channels of the initial convolutional layer. Specifically, linear features are transformed into non-linear ones through the connection of the upper GConv2 to a ReLU activation function. These non-linear characteristics then act as a convolutional layer that learns additional low-frequency features; GConv1 receives the output data from the final one-fifth of the channels.

(ii) Step 2. By employing the residual learning technique, the features extracted from all GConv1 layers are integrated to enhance the connections among the various extraction segments.

(iii) Step 3. To obtain additional complementary features, the outputs from the final GConv1 and GConv2 are integrated along the channel dimension using a concatenation operation, as indicated by "Concat" in Figure 6.

(iv) Step 4. To address the limitation of shallow feature memory capacity across the network, we employ the concept of signal augmentation to preserve long-distance features. This approach entails superimposing shallow features, obtained through the residual learning technique, onto the deep features acquired, thereby enhancing the significance of the shallow features.

2.4. GEB-MPU-Net structure

The progressive depth of MPU-Net may compromise shallow feature retention, potentially limiting its contribution to final representations. To mitigate this limitation, GEBs are systematically integrated following each CAB module across three critical processing stages, as detailed in Figure 7. This architecture optimizes shallow feature integration while effectively attenuating noise through enhanced low-frequency representation. It strengthens inter-channel correlations, thereby improving feature discrimination across multiple scales without compromising signal integrity.

An ablation experiment was conducted on the network architecture to justify the choice of architecture and demonstrate its optimality. Figure 7 depicts Strategy 1's organizational framework, in which the GEB module is placed after the CAB modules in the three stages of

MPU-Net. Figure 8 illustrates Strategy 2's organizational structure. The GEB module is placed respectively after the encoder-decoder modules of the first and second stages, as well as the ORSNet + Conv of the third stage. Figure 9 shows the construction of Strategy 3, in which the CSFF module is followed by the GEB module.

The synthetic records with varying noise levels were denoised using the three different GEB-MPU-Net network structures. Figures 10 and 11 display the denoising and residual results, respectively. Figure 10 reveals characteristic waveform distortion at the intersection of Strategy 2 and Strategy 3's in-phase axes, as highlighted by the red annotation box. The residual data presented in Figure 11 indicate superior amplitude retention in Strategy 1, as evidenced by reduced phase-coherent artifacts compared to Strategies 2 and 3. Table 1 presents the peak SNR and mean squared error (MSE) of the denoising outcomes. The results demonstrate Strategy 1's superior performance in both noise suppression and amplitude preservation across varying noise conditions,

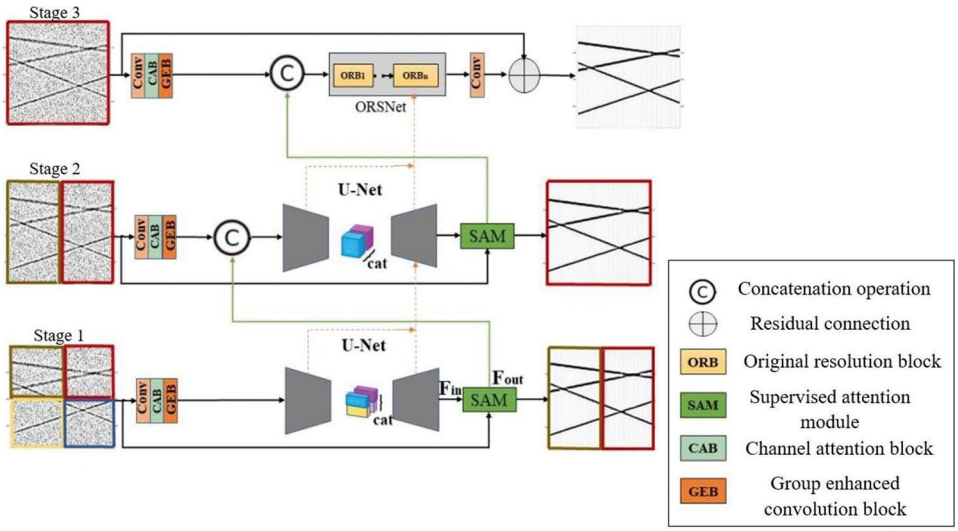

Figure 7. Structure of group enhanced convolution block, multi-stage progressive U-shaped convolutional network of Strategy 1
Abbreviations: cat: Concatenate; Conv: Convolution; U-Net: U-shaped convolutional network

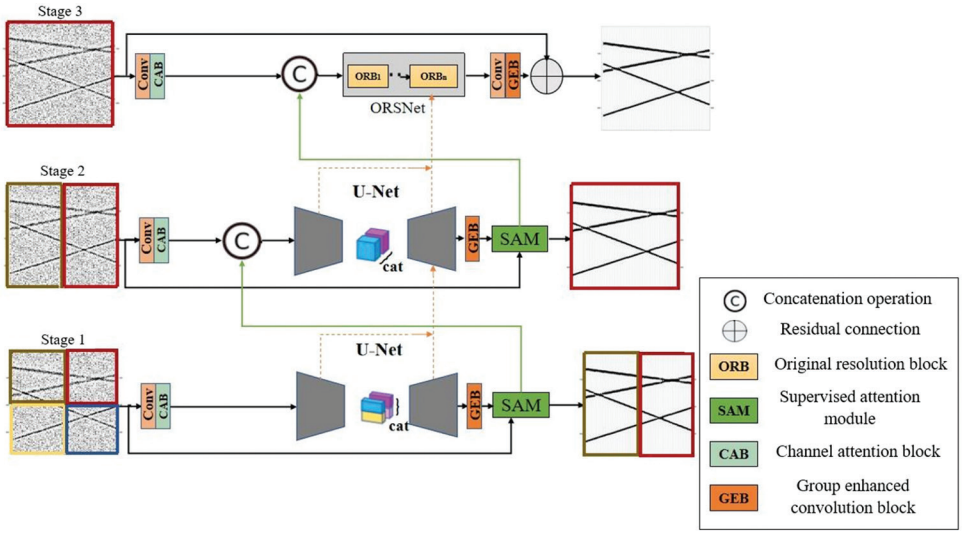

Figure 8. Structure of group enhanced convolution block, multi-stage progressive U-shaped convolutional network of Strategy 2
Abbreviations: cat: Concatenate; Conv: Convolution; U-Net: U-shaped convolutional network

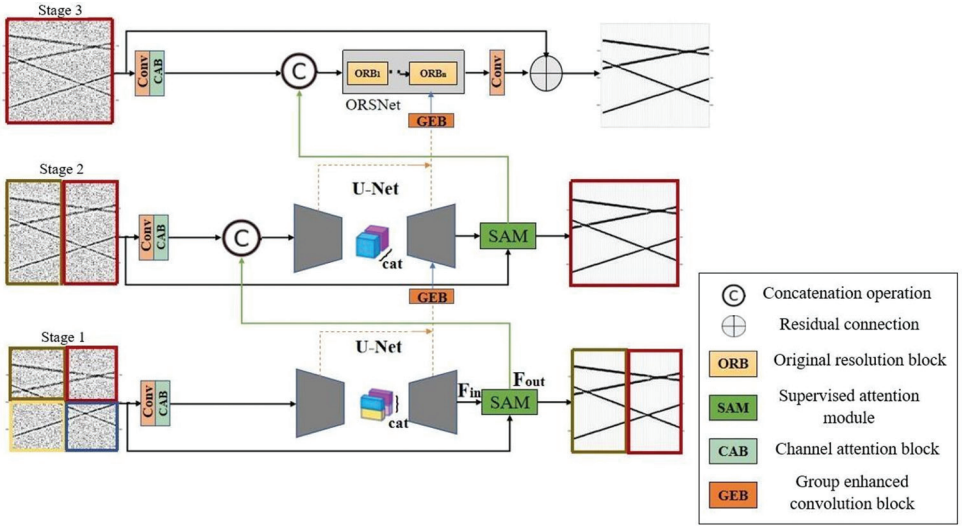

Figure 9. Structure of group enhanced convolution block, multi-stage progressive U-shaped convolutional network of Strategy 3
Abbreviations: cat: Concatenate; Conv: Convolution; U-Net: U-shaped convolutional network

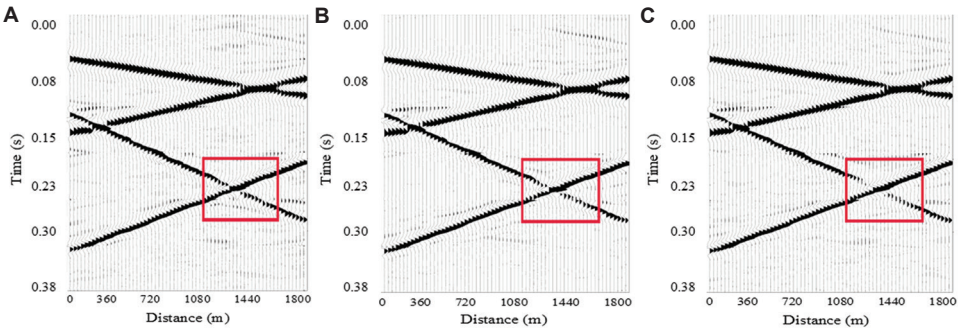

Figure 10. Denoising results of the three strategies. (A) Strategy 1. (B) Strategy 2. (C) Strategy 3

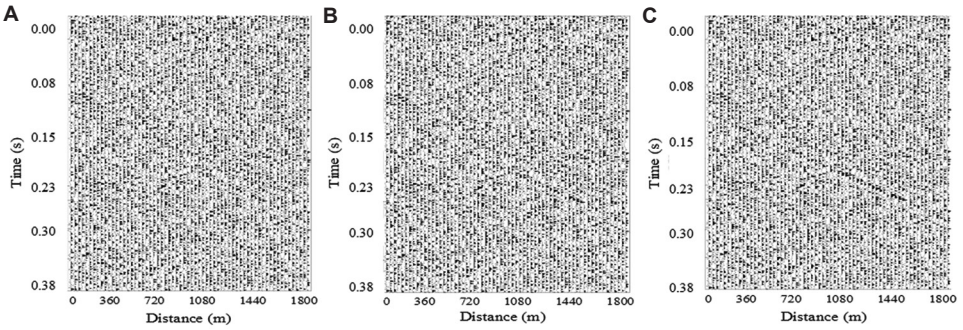

Figure 11. Residual results of the three strategies. (A) Strategy 1. (B) Strategy 2. (C) Strategy 3

exhibiting consistently favorable metric values compared to alternative approaches.

Figure 12A and B present the comparative evaluation metrics across the simulated dataset after completing training. The results reveal Strategy 1's consistent advantage in signal preservation, with both alternative strategies demonstrating relatively reduced performance across the measured parameters.

2.5. GEB-MPU-Net denoising principle

The process of removing noise from seismic recordings that contain a combination of signals and noise is referred

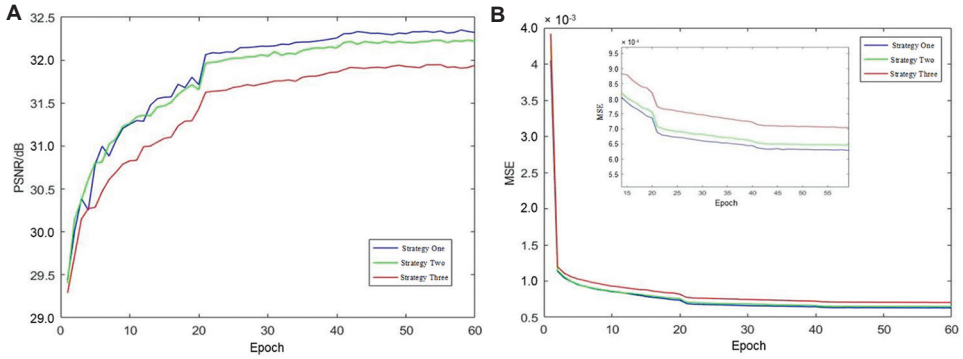

Figure 12. Influence of three strategies on denoising. (A) The PSNR performance curve on the test set. (B) The MSE performance curve on the test set
Abbreviations: MSE: Mean squared error; PSNR: Peak signal to noise ratio

Table 1. Comparison of parameters after denoising of three strategies

Strategies	Signal-to-noise ratio (dB)	Mean squared error
Noisy signal	−5.1753	0.0161
	−8.1856	0.0321
	−9.9465	0.0482
Strategy 1	11.8588	3.1806 e−04
	9.1082	5.9920 e−04
	7.2832	9.1215 e−04
Strategy 2	11.5535	3.4123 e−04
	8.6248	6.6975 e−04
	6.7186	0.0010
Strategy 3	11.5279	3.4324 e−04
	8.1443	7.4810 e−04
	6.0058	0.0012

to as random noise suppression in seismic data. Equation I represents the noisy seismic data.

$$d = x + n \quad \text{(I)}$$

where d denotes the noisy data, x represents the clean seismic signal, and n signifies the random noise. In this study, we employed a noise learning technique by inputting the noisy seismic data into the GEB-MPU-Net neural network. Through the process of residual learning, the network was trained to predict the noise, which was then subtracted from the input noisy seismic records to yield denoised seismic data. The specific procedure is outlined in Equations II and III.

$$Nt = R\,(d;\theta) \quad \text{(II)}$$

$$\hat{x} = d - Nt \quad \text{(III)}$$

where Nt represents the predicted noise output by the network, R denotes the residual mapping process, θ encompasses the parameters of the network, including weights ω and biases b, and $\hat{x}$ signifies the predicted seismic record. We utilized the MSE between the pure noise and the predicted noise as the loss function to optimize the parameters. The formulation for the loss function is shown in Equation IV.

$$L_{loss}(\theta) = \frac{1}{M}\sum_{i=1}^{M}\left\| R\,(d_i;\theta) - n_i \right\|^2_{GEB-MPU-Net} \quad \text{(IV)}$$

where M is the number of samples in the training set, $\|\cdot\|^2_{GEB-MPU-Net}$ denotes the Frobenius norm, d_i represents the noisy seismic data, and n_i is the pure noise. The objective of the network's continuous training is to minimize the loss function, a non-negative real-valued function. A smaller loss indicates a reduced error between the predicted noise and the actual noise, leading to denoised seismic records that closely approximate the ideal seismic records.

The comprehensive dataset from the 1994 Canadian reverse masking experiment, named Model94_shots.segy, served as the training data for the network. This dataset comprises 277 shots, each containing 480 recording channels, with a channel spacing of 15 m and a shot interval of 90 m. Following manual processing, the dataset demonstrated a high SNR and has been widely recognized as a representative clean record. Users can add varying levels of Gaussian white noise or real noise according to their requirements. After normalization, the data were segmented into 64 × 64 patches using a sliding window with a step size of 32, resulting in a total of 41,776 samples, with 31,656 samples designated for training and 10,120 samples for testing. The Adam optimization algorithm was utilized during training, with MSE as the loss function. The learning rate gradually decreased from 2×10^{-4} to 2×10^{-6}, the batch size was set to 8, and the number of training epochs was established at 60. The experiments were conducted within the PyTorch deep learning framework (version 2.2.0), operating on a Windows 11 system. The computations

were performed on a server equipped with an Intel(R) Core(TM) i5-12500H processor, 16 GB of RAM, CUDA 11.6, and an NVIDIA RTX 3050 Ti graphics card. The specific experimental steps were as follows:

(i) Step 1: Prepare the seismic signal dataset and conduct preprocessing
(ii) Step 2: Introduce noise into the clean seismic records and train the network using GEB-MPU-Net
(iii) Step 3: Adjust the network hyperparameters to ensure that the network output closely approximates the added noise
(iv) Step 4: Subtract the predicted noise output from the noisy records to obtain the denoised seismic records
(v) Step 5: Evaluate the trained network using both the noisy synthetic seismic records and actual seismic data
(vi) Step 6: Illustrate the frequency-wavenumber spectra of the denoised synthetic recordings and compare the time-frequency domain waveforms of the single-channel records
(vii) Step 7: Analyze the denoising performance in comparison to time-frequency analysis (TFPF), conventional U-Net, residual dense network (RDNet), residual dense block U-Net (RDBU-Net), and MPU-Net.

3. Experimental results

3.1. Synthetic records processing results

The clear synthetic seismic record comprises four distinct cross-seismic events distributed across 61 channels, with each trace containing 384 temporally sampled points at 1 ms intervals, as shown in Figure 13A. The Ricker wavelets exhibited characteristic dominant frequencies of 40 Hz and 60 Hz, representing typical exploration scenarios. The synthetic noisy record shown in Figure 13B was generated

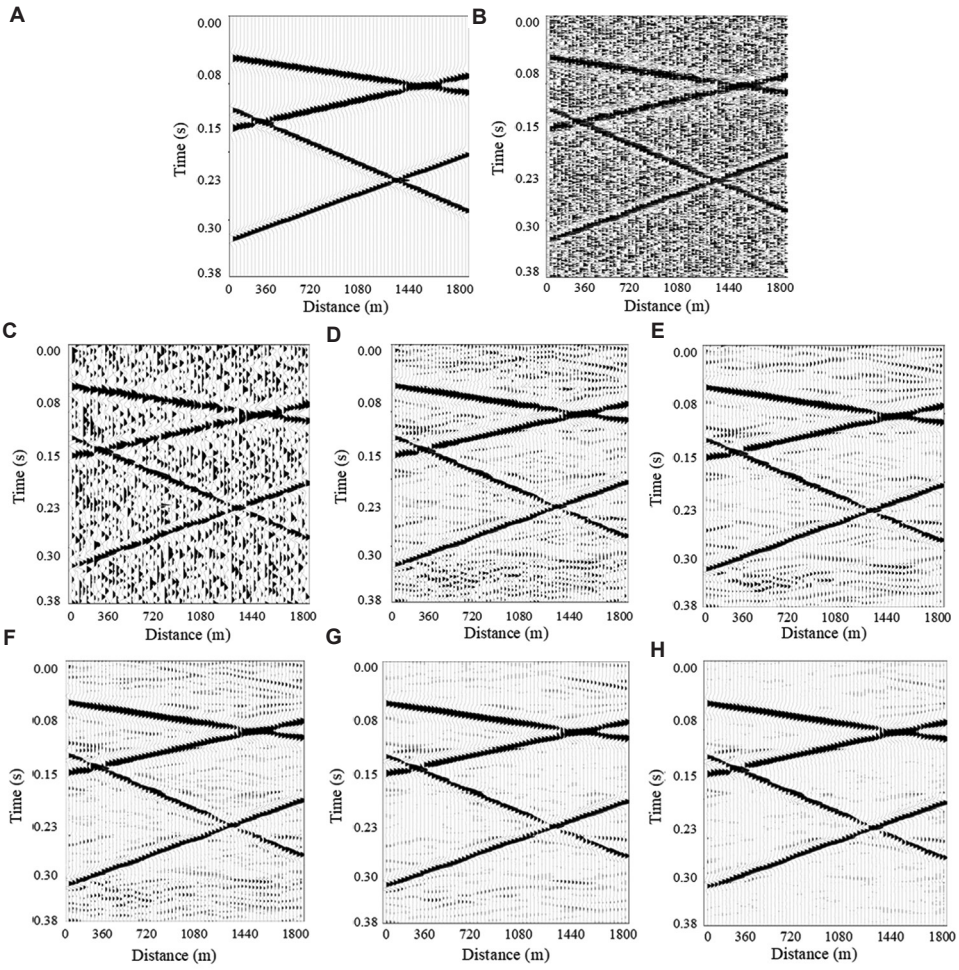

Figure 13. Denoising results of synthetic seismic records. (A) Pure record. (B) Noisy record. (C) TFPF. (D) U-Net. (E) RDNet. (F) RDBU-Net. (G) MPU-Net. (H) GEB-MPU-Net

Abbreviations: GEB-MPU-Net: Group enhanced convolutional blocks-multi-stage progressive U-Net; MPU-Net: Multi-stage progressive U-Net; RDBU-Net: Residual dense block U-Net; RDNet: Residual dense network; TFPF: Time-frequency analysis; U-Net: U-shaped convolutional network

through additive Gaussian white noise at a level of 85% contamination of the pristine dataset. The noisy record was processed through multiple denoising approaches, encompassing conventional TFPF, established neural networks (U-Net, RDNet), and advanced architectures (RDBU-Net, MPU-Net, GEB-MPU-Net). Figure 13C-H displays the processed outputs from each denoising method, with corresponding residual patterns shown in Figure 14. Figure 13C presents the results obtained by TFPF, demonstrating partial noise attenuation while retaining visible signal components in the corresponding residuals, as shown in Figure 14A. This outcome highlights the method's fundamental limitation in achieving complete signal-noise separation, with discernible seismic events persisting in the residual domain. Figures 13D and 14B present the U-Net processed results and the corresponding residual record, demonstrating significantly improved noise suppression capabilities compared to conventional approaches. The neural network output exhibits enhanced signal clarity while effectively attenuating both random and coherent noise components. Figure 13E and F present the processed outputs from RDNet and RDBU-Net, and Figure 14C and D show the corresponding residuals, respectively, demonstrating superior noise suppression compared to the baseline U-Net architecture. Both advanced networks showed progressively improved seismic event visibility, with enhanced signal-background differentiation by the processed records.

Figures 13G and 14E illustrate the denoising outcome and residuals of MPU-Net, where the seismic events are more distinct, and the noise is substantially suppressed, although some distortion occurs at the intersection points of the events. Figure 13H presents the GEB-MPU-Net processed results, demonstrating exceptional signal clarity and waveform coherence in the reconstructed seismic record. The corresponding residuals in Figure 14F show negligible seismic event remnants, indicating near-complete signal preservation and noise separation.

Figure 15A-H presents comparative frequency-wavenumber transformations of the pure record, noisy record, and all processed outputs. This comprehensive spectral analysis enables detailed evaluation of wavenumber-frequency characteristics across different denoising approaches. Figure 15C shows the frequency-wavenumber spectrum following TFPF, revealing characteristic spectral overlap between residual noise components and preserved signal energy. While the method demonstrated partial noise suppression in certain frequency-wavenumber bands, significant signal-noise ambiguity persisted across critical regions of the spectrum. Figure 15D-F demonstrates that U-Net, RDNet, and RDBU-Net achieve substantial random noise suppression in the wavenumber-frequency domain. However, these architectures showed limited effectiveness against persistent low-frequency noise components, revealing a common challenge in neural network-based seismic

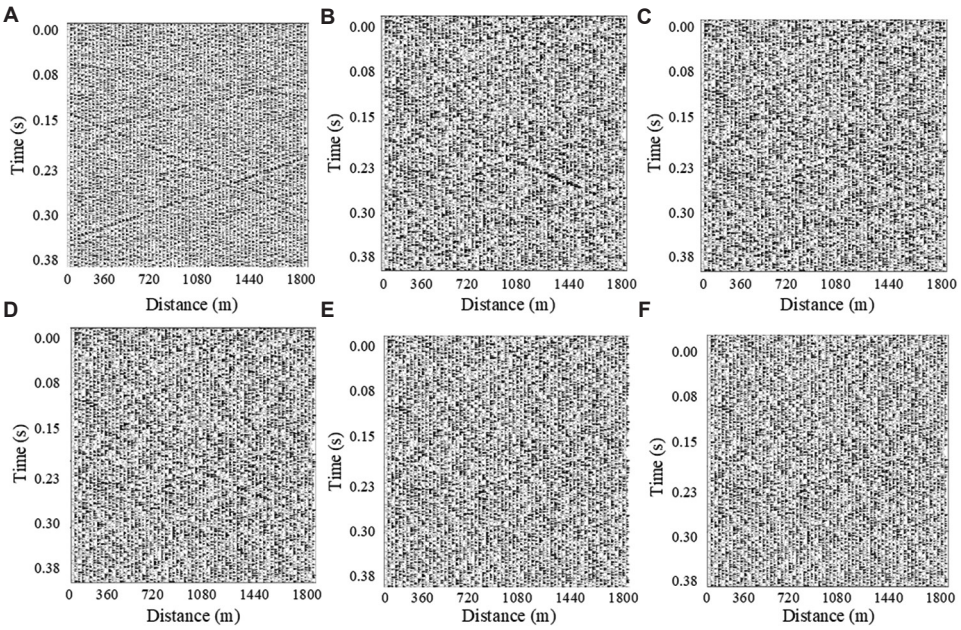

Figure 14. Residual results of synthetic seismic records. (A) TFPF. (B) U-Net. (C) RDNet. (D) RDBU-Net. (E) MPU-Net. (F) GEB-MPU-Net
Abbreviations: GEB-MPU-Net: Group enhanced convolutional blocks-multi-stage progressive U-Net; MPU-Net: Multi-stage progressive U-Net; RDBU-Net: Residual dense block U-Net; RDNet: Residual dense network; TFPF: Time-frequency analysis; U-Net: U-shaped convolutional network

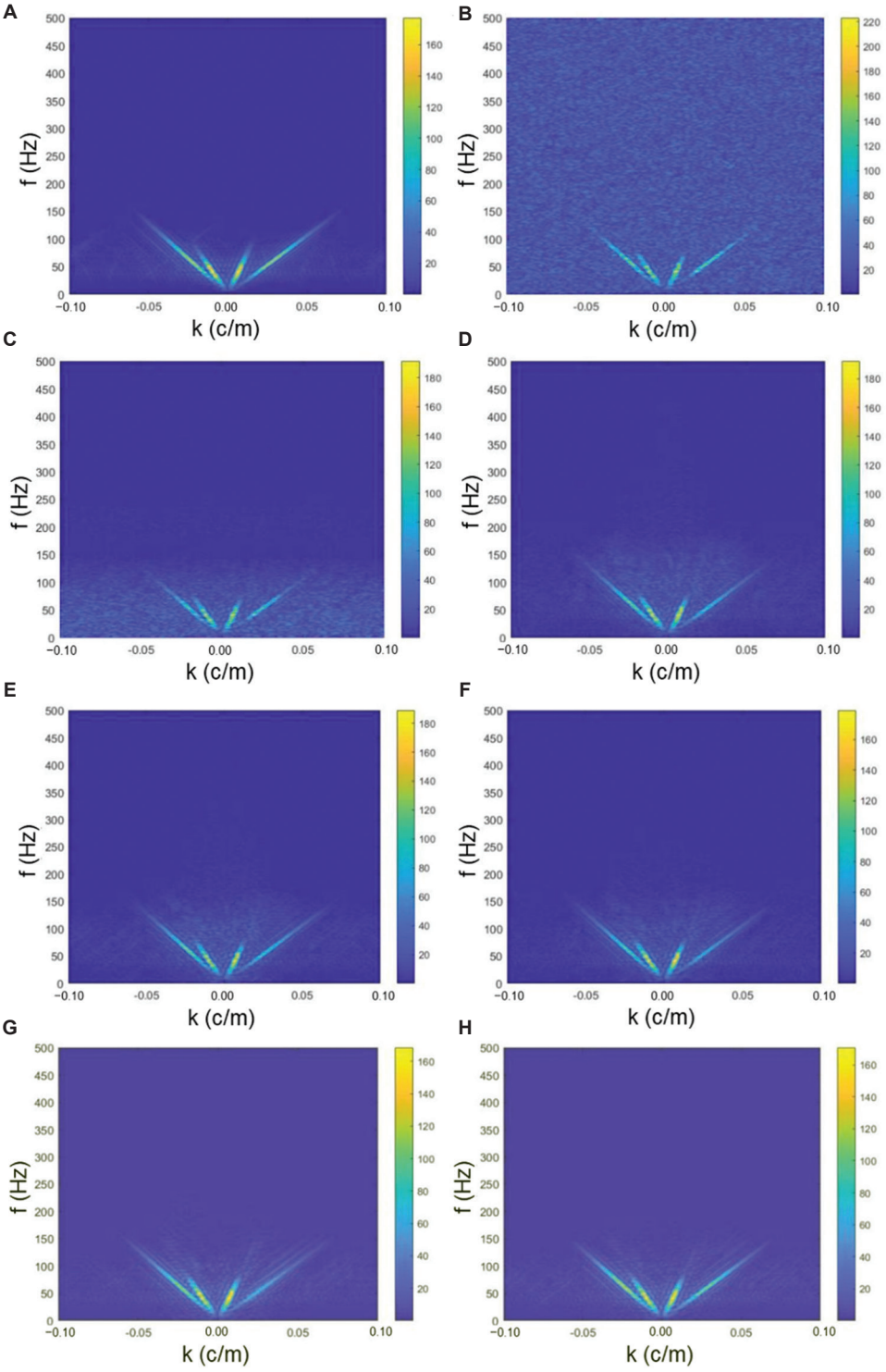

Figure 15. Frequency-wavenumber spectra of synthetic seismic records. (A) Pure record. (B) Noisy record. (C) TFPF. (D) U-Net. (E) RDNet. (F) RDBU-Net. (G) MPU-Net; (H) GEB-MPU-Net

Abbreviations: GEB-MPU-Net: Group enhanced convolutional blocks-multi-stage progressive U-Net; MPU-Net: Multi-stage progressive U-Net; RDBU-Net: Residual dense block U-Net; RDNet: Residual dense network; TFPF: Time-frequency analysis; U-Net: U-shaped convolutional network

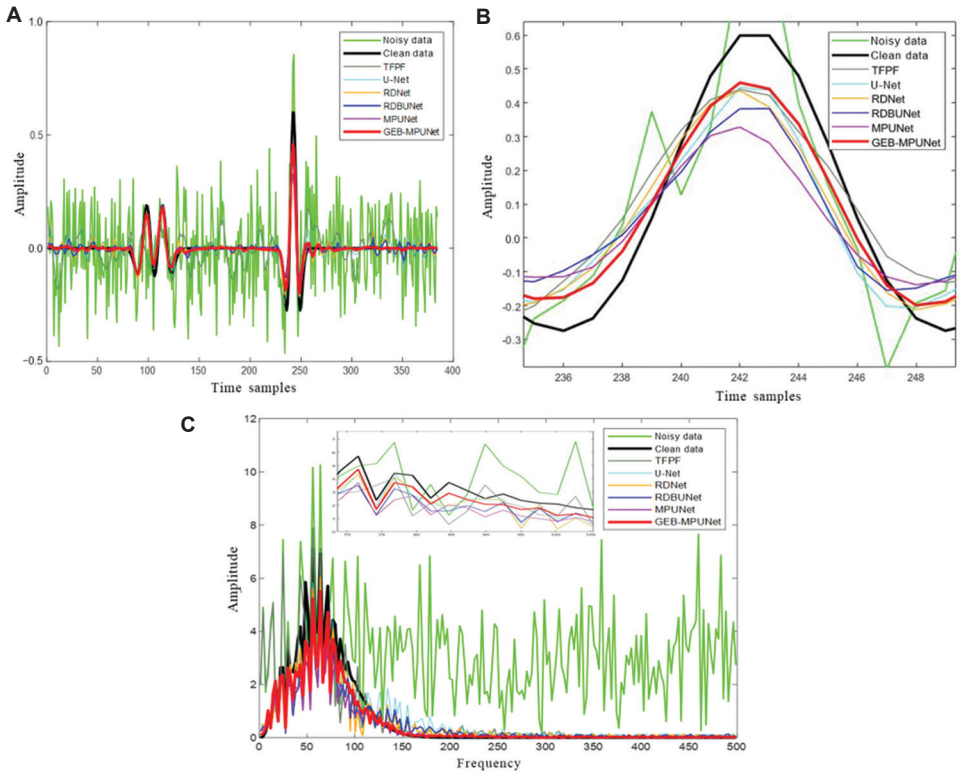

Figure 16. Single trace record comparison. (A) Time-domain waveform. (B) Enlarged view of the last peak in (A). (C) Frequency-domain waveform Abbreviations: GEB-MPU-Net: Group enhanced convolutional blocks-multi-stage progressive U-Net; MPU-Net: Multi-stage progressive U-Net; RDBU-Net: Residual dense block U-Net; RDNet: Residual dense network; TFPF: Time-frequency analysis; U-Net: U-shaped convolutional network

processing. Comparative analysis of Figure 15G and H reveals GEB-MPU-Net's enhanced spectral fidelity, with its frequency-wavenumber transform exhibiting closer alignment to the noise-free reference than MPU-Net's output. This improved spectral reconstruction demonstrates the architecture's advanced noise suppression while maintaining critical signal components across wavenumber-frequency domains.

To evaluate GEB-MPU-Net's performance, a random single trace (Trace 45) was selected from the noise-free reference dataset (Figure 13A) for detailed time-frequency analysis. The time-domain comparing waveforms are presented in Figure 16A. An enlarged view of the last peak of the time domain waveform is provided in Figure 16B. Lastly, the frequency domain comparing waveforms can be observed in Figure 16C. The results indicate that the waveform generated by GEB-MPU-Net closely resembles that of the pure signal, demonstrating that the seismic signal recovered through GEB-MPU-Net denoising is the most complete and cleanest, with a significant advantage in preserving effective signal amplitude.

The study employed standard quantitative metrics to assess denoising effectiveness and signal preservation across different methods. Comparative analysis reveals GEB-MPU-Net's superior performance in both noise suppression and amplitude retention relative to alternative approaches, as documented in Table 2.

Table 2. Comparison of parameters after denoising with different methods

Methods	Parameters	
	Signal-to-noise ratio (dB)	Mean squared error
Noisy signal	−8.1856	0.0321
TFPF	0.1597	0.0047
U-Net	5.4996	0.0014
RDNet	6.8447	0.001
RDBU-Net	7.4174	8.84 e−04
MPU-Net	8.3013	7.22 e−04
GEB-MPU-Net	9.1082	5.99 e−04

Abbreviations: GEB-MPU-Net: Group enhanced convolutional blocks-multi-stage progressive U-Net; MPU-Net: Multi-stage progressive U-Net; RDBU-Net: Residual dense block U-Net; RDNet: Residual dense network; TFPF: Time-frequency analysis; U-Net: U-shaped convolutional network.

3.2. Field data processing results

Figure 17A shows part of an acquired field seismic dataset collected under forested terrain conditions, comprising

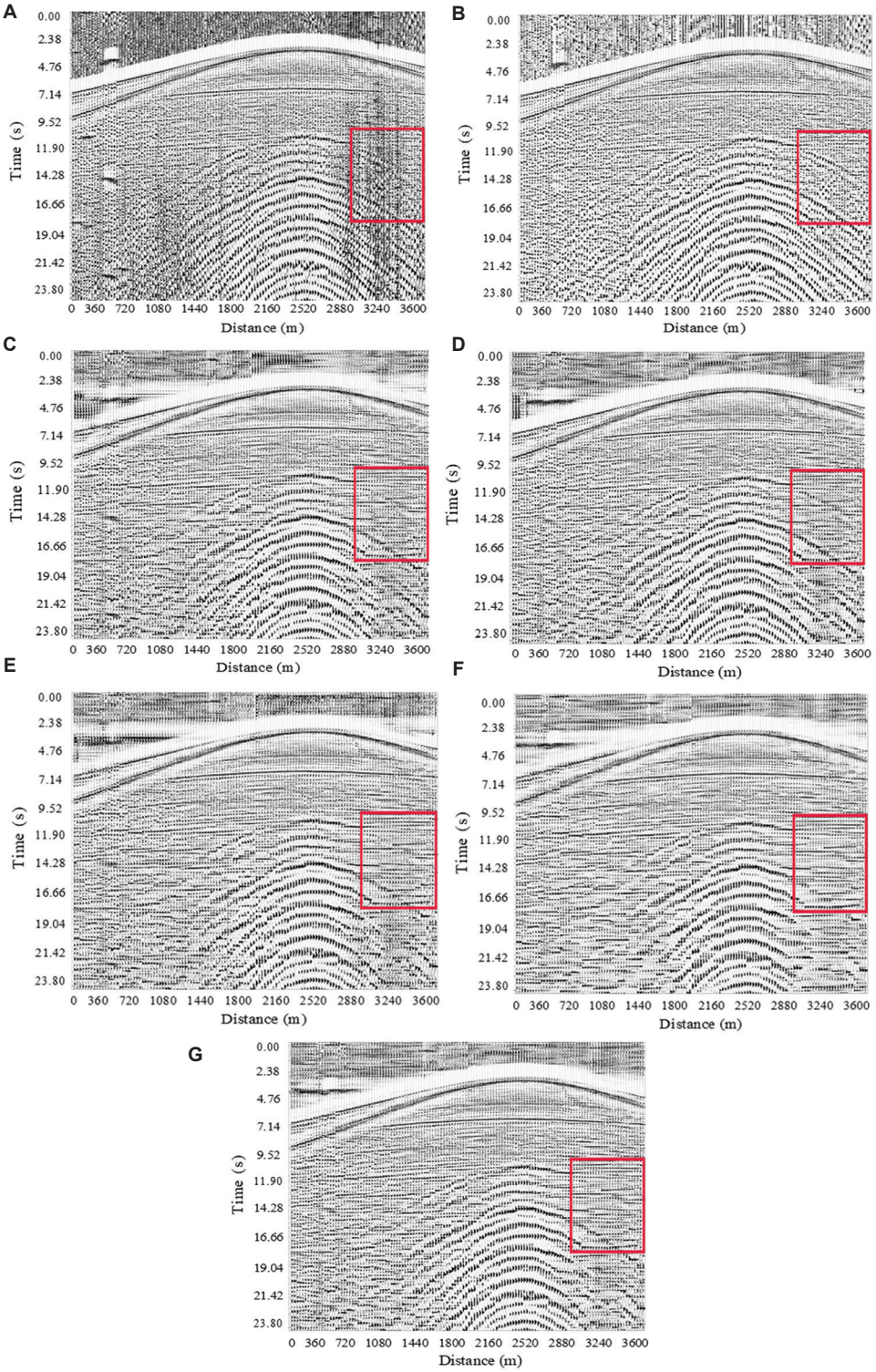

Figure 17. Denoising results of the field seismic record. (A) Field seismic data. (B) TFPF. (C) U-Net. (D) RDNet. (E) RDBU-Net. (F) MPU-Net. (G) GEB-MPU-Net

Abbreviations: GEB-MPU-Net: Group enhanced convolutional blocks-multi-stage progressive U-Net; MPU-Net: Multi-stage progressive U-Net; RDBU-Net: Residual dense block U-Net; RDNet: Residual dense network; TFPF: Time-frequency analysis; U-Net: U-shaped convolutional network

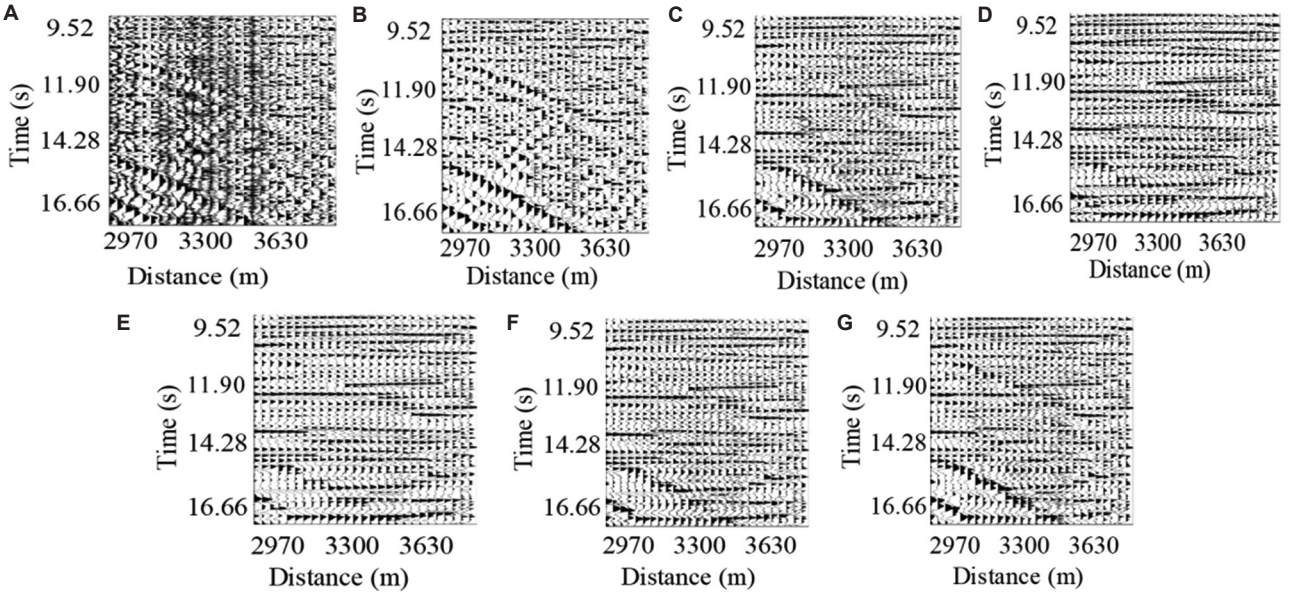

Figure 18. Enlarged comparison of red boxes in Figure 17. (A) Field seismic data. (B) TFPF. (C) U-Net. (D) RDNet (E) RDBU-Net. (F) MPU-Net. (G) GEB-MPU-Net
Abbreviations: GEB-MPU-Net: Group enhanced convolutional blocks-multi-stage progressive U-Net; MPU-Net: Multi-stage progressive U-Net; RDBU-Net: Residual dense block U-Net; RDNet: Residual dense network; TFPF: Time-frequency analysis; U-Net: U-shaped convolutional network

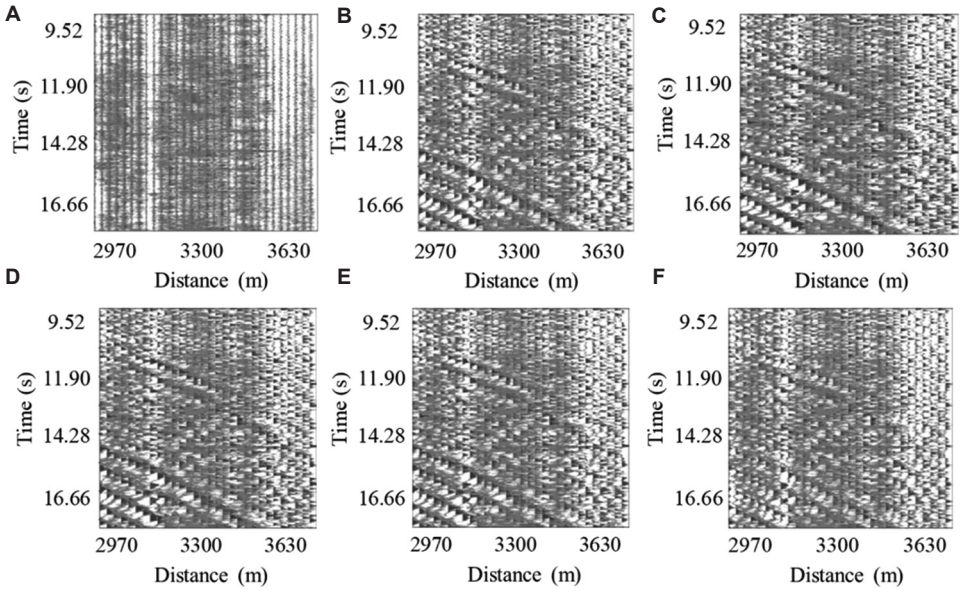

Figure 19. Corresponding residual record of Figure 18. (A) TFPF. (B) U-Net. (C) RDNet. (D) RDBU-Net. (E) MPU-Net. (F) GEB-MPU-Net
Abbreviations: GEB-MPU-Net: Group enhanced convolutional blocks-multi-stage progressive U-Net; MPU-Net: Multi-stage progressive U-Net; RDBU-Net: Residual dense block U-Net; RDNet: Residual dense network; TFPF: Time-frequency analysis; U-Net: U-shaped convolutional network

128 channels with temporal sampling characteristics suitable for detailed subsurface analysis. This record underwent comprehensive processing through multiple denoising approaches, including conventional and deep learning-based methods, with the outputs shown in Figure 17B-G.

The TFPF output in Figure 17B demonstrates partial background noise attenuation while exhibiting characteristic limitations in suppressing surface wave contamination and persistent low-frequency noise components. This performance pattern reflects fundamental constraints of traditional signal processing approaches in complex field environments.

Figure 17C-F presents the processed outputs from U-Net, RDNet, RDBU-Net, and MPU-Net, demonstrating progressive improvements in both noise suppression and signal recovery compared to conventional methods. While these architectures showed enhanced capability in revealing subsurface features, opportunities remain for further resolution enhancement in complex geological settings. Figure 17G demonstrates GEB-MPU-Net's superior processing results, exhibiting comprehensive noise suppression while significantly enhancing seismic reflection continuity and resolution. The output displayed markedly improved signal clarity compared to alternative methods, with well-preserved geological features throughout the profile.

The magnified views of the red boxes in Figure 17 and the corresponding residual records are shown in Figures 18 and 19, respectively. Figures 18B and 19A reveal severe low-frequency noise and surface wave interference that obscure underlying signals. While U-Net processing in Figures 18C and 19B enables initial event detection near surface waves, residual noise contamination remains substantial. As shown in Figures 18D-F and 19C-E, subsequent architectures demonstrate progressive improvements, with RDNet, RDBU-Net, and MPU-Net achieving measurable noise reduction and signal recovery. GEB-MPU-Net emerges as the most effective solution, delivering superior noise suppression and event clarity, as shown in Figure 18G and Figure 19F.

4. Conclusion

Building upon the MPU-Net framework, this study developed GEB-MPU-Net through the systematic integration of GEB following each CAB within the three-stage processing hierarchy. This enhancement establishes a more robust feature learning pipeline while preserving the original network's multi-scale analysis capabilities. The GEB significantly enhanced low-frequency feature representation through three coordinated mechanisms: (i) Strategic channel segmentation enabling specialized frequency processing, (ii) adaptive channel width expansion for comprehensive feature capture, and (iii) intelligent integration of deep-wide channel correlations. This multi-faceted approach optimized information flow across network depths while preserving critical seismic signatures. The GEB module incorporated a novel signal augmentation mechanism to mitigate progressive attenuation of shallow features in deep networks. This design addresses a fundamental limitation in MPU-Net's architecture, where excessive network depth could compromise both denoising accuracy and output stability. The augmentation strategy actively maintains critical near-surface information throughout the processing hierarchy. The GEB module implements residual learning to create direct feature pathways between input and output layers. This architecture strategically combines shallow and deep representations through additive merging, ensuring preservation of critical near-surface features, stable gradient propagation across network depths, and enhanced overall denoising robustness. Experimental results across synthetic and field datasets demonstrated GEB-MPU-Net's consistent advantages over the baseline MPU-Net architecture. The enhanced network exhibited superior signal fidelity through improved amplitude preservation and more effective noise suppression, particularly for random noise components. In addition, the advanced framework yielded clearer seismic reflections with enhanced continuity, enabling more reliable geological interpretation.

Acknowledgments

This research was supported by the Shanxi Key Laboratory of Wireless Communication and Detection, which provided the necessary equipment for this work.

Funding

This work was supported in part by the Natural Science Foundation of Shanxi Province (202103021224012).

Conflict of interest

The authors declare they have no competing interests.

Author contributions

Conceptualization: Guanghui Li
Data curation: Li Wang
Methodology: Guanghui Li, Huiwei Li, Shoufeng He
Software: Huiwei Li, Shoufeng He
Visualization: Guanghui Li, Huiwei Li, Shoufeng He
Writing–original draft: Guanghui Li, Huiwei Li
Writing–review & editing: Guanghui Li, Huiwei Li

Availability of data

Data are available upon request via liguanghui0352@163.com.

References

1. Lee D, Shin RS, Yeo ME. Denoising sparker seismic data with deep BiLSTM in fractional Fourier transform. *Comput Geosci*. 2024;184:105519.

   doi: 10.1016/j.cageo.2024.105519

2. Geetha K, Kumar MH, Ajitha DK. A novel approach for seismic signal denoising using optimized discrete wavelet transform via honey badger optimization algorithm. *J Appl Geophys*. 2023;219:105236.

   doi: 10.1016/j.jappgeo.2023.105236

3. Zhang S, Zhang D, Yang X, Xu S, Sun Z, Liu Y. Noise reduction method based on curvelet theory of seismic data.

Pet Sci Technol. 2023;41(24):2344-2361.

doi: 10.1080/10916466.2022.2118771

4. Li M, Li Y, Wu N, Wu J, Ma Y, Liu Q. Desert seismic data denoising based on energy spectrum analysis in empirical curvelet domain. *Stud Geophys Geod*. 2020;64(2):373-390.

doi: 10.1007/s11200-019-0476-4

5. Dalai B, Kumar P, Yuan X. De-noising receiver function data using the Seislet transform. *Geophys J Int*. 2019;217(3):2047-2055.

doi: 10.1093/gji/ggz135

6. Hasan MDA, Ahmad ZAB, Leong MS, Hee LM. Automated denoising technique for random input signals using empirical mode decomposition (EMD)-stabilization diagram. *MATEC Web Conf*. 2019;255:01004.

doi: 10.1051/matecconf/201925501004

7. Liu W, Liu Y, Li S, Chen Y. A review of variational mode decomposition in seismic data analysis. *Surv Geophys*. 2023;44(2):323-355.

doi: 10.1007/s10712-022-09742-z

8. Zhao YX, Li Y, Yang BJ. Denoising of seismic data in desert environment based on a variational mode decomposition and a convolutional neural network. *Geophys J Int*. 2020;221(2):1211-1225.

doi: 10.1093/gji/ggaa071

9. Li J, Fan W, Li Y, Li W, Zhang Y, Zeng M. Desert seismic noise suppression based on an improved low-rank matrix approximation method. *J Appl Geophys*. 2020;173:103926.

doi: 10.1016/j.jappgeo.2019.103926

10. Sun F, Zhang Q, Wang Z, Li Y. Compressed sensing with logsum heuristic recover for seismic denoising. *Front Earth Sci*. 2023;11:1285622.

doi: 10.3389/feart.2023.1285622

11. Liu L, Ma J. Structured graph dictionary learning and application on the seismic denoising. *IEEE Trans Geosci Remote Sens*. 2019;57(4):1883-1893.

doi: 10.1109/TGRS.2018.2870087

12. Liu Q, Fu L, Zhang M. Deep-seismic-prior-based reconstruction of seismic data using convolutional neural networks. *Geophysics*. 2021;86(2):V131-V142.

doi: 10.1190/geo2019-0570.1

13. Li X, Hawari KG, Huang F, Liu J, Zhang Y. Review of CNN in aerial image processing. *Imaging Sci J*. 2023;71(1):1-13.

doi: 10.1080/13682199.2023.2174651

14. Wei D, Chen G, Chen J, Li C, Wu S, Zhang Y. Seismic data denoising using a self-supervised deep learning network. *Math Geosci*. 2023;56(3):487-510.

doi: 10.1007/s11004-023-10089-3

15. Li J, Qu R, Lu C. Multiple attention mechanisms-based convolutional neural network for desert seismic denoising. *Pure Appl Geophys*. 2023;180(6):2135-2155.

doi: 10.1007/s00024-023-03255-5

16. Ji G, Wang C. A denoising method for seismic data based on SVD and deep learning. *Appl Sci*. 2022;12(24):12840.

doi: 10.3390/app122412840

17. Guo Z, Zhu S, Chen J, Zhu W. Research on deep convolutional neural network time-frequency domain seismic signal denoising combined with residual dense blocks. *Front Earth Sci*. 2021;9:770748.

doi: 10.3389/feart.2021.681869

18. Cai J, Wang L, Zheng J, Duan Z, Li L, Chen N. Denoising method for seismic co-band noise based on a U-Net network combined with a residual dense block. *Appl Sci*. 2023;13(3):1324.

doi: 10.3390/app13031324

19. Ding M, Zhou Y, Chi Y. Seismic signal denoising using Swin-Conv-UNet. *J Appl Geophys*. 2024;223:105355.

doi: 10.1016/j.jappgeo.2024.105355

20. Zamir SW, Arora A, Khan S, Hayat M, Khan F, Shah M. Multi-stage progressive image restoration. In: *Proceedings of the IEEE/CVF Conference on Computer Vision and Pattern Recognition*. Nashville, TN, USA, 2021. p. 14821-14831.

doi: 10.1109/CVPR46437.2021.01458

21. Saad MO, Ravasi M, Alkhalifah T. Self-supervised multistage deep learning network for seismic data denoising. *Artif Intell Geophysics*. 2025;6(1):100123.

doi: 10.1016/j.aiig.2025.100123

22. Obou.1016/j.aiig.2025.100123123ing. learning network for seismic data denoising. enoising. ng. sing. ing. ng. l denoising*Geophysics*. 2025;90(3):V205-V219.

doi: 10.1190/geo2024-0456.1

23. Tian C, Yuan Y, Zhang S, Wang X, Li H. Image super-resolution with an enhanced group convolutional neural network. *Neural Netw*. 2022;153:373-385.

doi: 10.1016/j.neunet.2022.06.009

24. Saad OM, Ravasi M, Alkhalifah T. Noise attenuation in distributed acoustic sensing data using a guided unsupervised deep learning network. *Geophysics*. 2024;89(6):V573-V587.

doi: 10.1190/geo2024-0109.1

25. Saad OM, Obou23-0642Bai M, Alkhalifah T, Wang Y, Liu J. Self-attention deep image prior network for unsupervised 3-D seismic data enhancement. *IEEE Trans Geosci Remote Sens*. 2021;60(5):1-14.

doi: 10.1109/TGRS.2021.3108515

ACCSCIENCE PUBLISHING

Journal of Seismic Exploration

ARTICLE

Seismic prediction methods for evaluating *in situ* stress in tilted transversely isotropic and monoclinic media

Jun Cheng[1], Yaojie Chen[2]*, and Zhensen Sun[3]

[1]Petroleum Development Center, Shengli Oilfield, Sinopec, Dongying, Shandong, China

[2]Department of Geophysical Exploration, School of Geoscience and Technology, Southwest Petroleum University, Chengdu, Sichuan, China

[3]Nanhai East Petroleum Research Institute, Shenzhen Branch, China National Offshore Oil Corporation Ltd., Shenzhen, Guangdong, China

Abstract

The formation of tectonic fractures is primarily influenced by stress distribution during the tectonic period. Therefore, *in situ* stress plays a crucial role in predicting fracture development zones. It significantly impacts the effectiveness of fractures by determining the size, orientation, and distribution pattern of fractures, thereby affecting stimulation results. Existing seismic methods for *in situ* stress prediction utilize seismic data to estimate stress parameters and calculate the horizontal stress difference ratio or the orthorhombic horizontal stress difference ratio (DHSR). These methods are based on the horizontal transverse isotropy or the orthorhombic anisotropy medium models. However, shale formations are often subject to tectonic movements that can rotate the symmetry axis of a transversely isotropic medium, leading to the formation of a tilted transversely isotropic (TTI) medium or a monoclinic medium with an inclined symmetry plane. Based on the TTI and monoclinic medium assumptions, this paper proposes new formulas for calculating the DHSRs (tilted transverse isotropy DHSR and monoclinic DHSR). The formulas are further validated through sensitivity analyses. Finally, this study demonstrates the effectiveness of the *in situ* stress seismic prediction method, grounded in TTI, and monoclinic medium theory through model-based examples.

Keywords: *In situ* stress; Tilted transverse isotropy differential horizontal stress ratio; Monoclinic differential horizontal stress ratio

***Corresponding author:**
Yaojie Chen
(202311000091@stu.swpu.edu.cn)

Citation: Cheng J, Chen Y, Sun Z. Seismic prediction methods for evaluating *in situ* stress in tilted transversely isotropic and monoclinic media. *J Seismic Explor.* 2025;34(1): 60-80.
doi: 10.36922/JSE025190002

Received: May 9, 2025

1st revised: July 3, 2025

2nd revised: July 22, 2025

3rd revised: August 1, 2025

Accepted: August 1, 2025

Published online: August 15, 2025

1. Introduction

With the growing global demand for energy, shale gas has garnered significant attention as a clean and efficient energy resource. In the exploration and development of shale gas reservoirs, *in situ* stress prediction plays a critical role. *In situ* stress, carried by underground rocks and pore fluids, is crucial for effective oil and gas exploration. The influence of tectonic stress drives the formation and evolution of geological structures. Furthermore, the *in situ* stress state of an oilfield governs the shape and distribution of faults. Therefore, studying *in situ* stress is essential for understanding geological structure formation and fault distribution. In-depth research on *in situ* stress prediction methods

for shale formations is vital for advancing the sustainable development of the shale gas industry.

Since the 1970s, both domestic and international scholars have conducted extensive research on methods for predicting *in situ* stress. Traditional methods, such as core testing, logging data analysis, and numerical simulations, have certain limitations, including small prediction ranges, high costs, and cumbersome processes. To better understand the nature and changes of *in situ* stress, researchers have proposed using seismic data for prediction.[1-4] In this context, Gray *et al.*[5] combined Iverson's hypothesis with linear slip theory to derive a horizontally transversely isotropic (HTI) medium *in situ* stress formula, which incorporates parameters such as Young's modulus, Poisson's ratio, and fracture compliance.[5-8] Given that these parameters can be directly obtained through pre-stack seismic inversion, this approach has become a promising direction for seismic *in situ* stress prediction.[9,10] In addition, Gray[7] introduced the horizontal stress difference ratio (DHSR) as the ratio of the difference between the maximum and minimum horizontal principal stresses to the maximum principal stress, providing a new way to describe ground stress. Unlike traditional methods, this approach is simple and practical. It addresses the challenge of inaccurate vertical stress prediction caused by the low accuracy of density inversion using DHSR as a sensitive *in situ* stress parameter. Compared to traditional logging-based methods, which are limited to drilling locations and suffer from low lateral resolution, this seismic method can provide *in situ* stress distributions across large areas, offering a more comprehensive understanding of underground stress and better guidance for petroleum engineering. Gray's method thus introduces a novel approach and practical tool to *in situ* stress research, greatly supporting fields such as petroleum exploration and development.

Building on Gray's work, Ma *et al.*[11,12] incorporated vertical fractures into the vertically transversely isotropic (VTI) medium for horizontal layered strata, treating fractured shale formations as orthotropic media. Using anisotropic media theory, they derived an orthotropic *in situ* stress formula. Following Gray's concept of the DHSR, they introduced the orthorhombic DHSR for the orthorhombic anisotropy (OA) medium. Wang[13] used azimuth-pre-stack seismic data combined with orthogonal anisotropy theory to predict ground stress, while also calculating the DHSR from the orthogonal anisotropy model combined with pre-stack elastic impedance inversion, focusing on tight sandstone formations.[14] Li *et al.*[15] utilized seismic inversion to estimate intercept, gradient, and curvature impedances to predict ground stress.[15] In addition, Wang *et al.*[16] proposed an inversion algorithm for the earth stress field based on the Tikhonov regularization and least squares methods.[16] Geophysical prediction methods are subject to significant uncertainty. This is primarily because seismic inversion is a typical ill-posed problem, and seismic data are often affected by noise, which leads to considerable uncertainty in *in situ* stress prediction. Researchers have conducted studies to reduce the uncertainty associated with these prediction methods.[17-22] However, as geophysical theories advance and our understanding of underground rock conditions deepens, there is a shift from modeling simple media to more complex media. Given the increasing complexity of real-world factors, it is essential to explore *in situ* stress characterization methods for these more complex media.

Formations comprising inclined fractures are widely distributed underground and can be effectively represented as tilted transversely isotropic (TTI) media. Vertically transversely isotropic (VTI) symmetry is most commonly found in shale formations, which account for approximately 75% of clastic infill in sedimentary basins worldwide. However, in tectonically active regions such as fold-and-thrust belts or areas near salt bodies, these anisotropic shale layers are often tilted due to structural deformation, resulting in TTI media. For example, up-dipping shale layers near salt domes are expected to form an effective TTI medium with a relatively large tilt of the symmetry axis. TTI models are also typically applicable to thrust fault zones, such as the Canadian Foothills or the Himalayan Foothills. TI shale layers are frequently bent by tectonic processes, often resulting in significant tilting.[23,24] In 1997, Tsvankin[25] studied typical TI models with tilted symmetry axes, such as sediments near the flanks of salt domes, and found that dipping layers significantly affect the imaging of salt bodies. When imaging steeply dipping structures such as salt domes or volcanic intrusions, the tilt of the symmetry axis in TI media should be taken into account.[25] In 2004, Isaac and Lawton[26] proposed an independent method for estimating effective anisotropic parameters from surface P-wave reflection seismic data. They tested this approach using a two-dimensional physical model of seismic data from a stepped target beneath a tilted TTI overburden. The experimental results showed that assuming isotropy in an equivalent TTI medium led to significant errors, thereby demonstrating the impact of anisotropy.[26] In 2008, Charles *et al.*[27] studied seismic imaging in the Canadian Foothills thrust belt. In the study area, the shallow overburden was composed of tilted, shale-dominated clastic rocks, which exhibited weak TTI properties. The experimental results showed that anisotropic depth imaging based on data-driven tomography produced better results than isotropic depth imaging using the same tomography approach.[27] In many

cases, formations subjected to either single-phase shear stress or multiple tectonic events tend to develop two sets of mutually oblique vertical fractures. Such formations can be abstracted in seismology as a special case of monoclinic anisotropic media. Reservoirs with monoclinic symmetry are quite common in oil and gas exploration. Examples include the Ordovician formations in the Tofutai area of the Tarim Basin in China,[28] the carbonate formations of the Clair Group in the Clair Field, United Kingdom,[29] and the Marcellus Shale in Bradford County, Pennsylvania, United States of America,[30] all of which represent monoclinic reservoirs with hydrocarbon potential. In 2023, Li[31] conducted a seismic response analysis and parameter inversion for a monoclinic medium model induced by two sets of mutually oblique vertical fractures. The study area was located in the Sichuan Basin in southwestern China, where the reservoir belongs to the Lower Triassic and is characterized by well-developed tectonic fractures due to the influence of the Himalayan orogeny. During the Triassic compressional period, one set of extensional fractures formed concurrently with folding. Subsequently, during the Himalayan orogenic phase, renewed compressional stress acted on the pre-existing folds, resulting in the development of a second set of fractures. This led to the formation of an equivalent monoclinic anisotropic medium. The inversion method was ultimately applied to the study area, improving the accuracy of the inversion results.[31] These cases clearly demonstrate the necessity of incorporating the effects of TTI and monoclinic anisotropy in seismic stress field prediction for geologically complex regions. Neglecting such anisotropy may lead to misinterpretations of fracture orientation, stress magnitude, and the geomechanical behavior of the reservoir. Therefore, research on stress field prediction based on TTI and monoclinic media is of critical importance.

Considering that inclined fractures influence actual shale formations, this study proposes *in situ* stress formulas based on the TTI and monoclinic media, along with the corresponding DHSRs, including the tilted transverse isotropy DHSR (TDHSR) and the monoclinic DHSR (MDHSR). By fully accounting for the effects of horizontal bedding and inclined fractures on DHSRs, the derived expressions offer higher applicability than the HTI and OA media, allowing for more accurate application to complex TTI and monoclinic media. This provides a more robust theoretical foundation for related research and applications.

First, the *in situ* stress formulas for the HTI and OA media are introduced. Then, based on the anisotropy theory, the formulas for the DHSRs in TTI and monoclinic media are derived. The correctness of these formulas is verified through formula degradation and model trial calculations. Finally, the relationship between the DHSRs of TTI and monoclinic media and factors such as elastic parameters, anisotropy parameters, and the dip angles of formations and fractures is analyzed and summarized. Model-based analysis further demonstrates the validity of the *in situ* stress seismic prediction method based on the TTI and monoclinic medium theories.

2. Materials and methods

2.1. Introduction to the basic theory

The constitutive equation of an elastic medium is an equation that describes the linear relationship between stress and strain using the stiffness tensor, also known as the generalized Hooke's law. For any anisotropic linear elastic medium, the stress and strain have the following linear relationship in **Equation I**:

$$\sigma_{ij} = C_{ijkl}\varepsilon_{kl}(\mathrm{i,j,k,l} \in 1,2,3) \tag{I}$$

where σ_{ij} is the stress tensor, ε_{kl} is the strain tensor, and C_{ijkl} is the stiffness tensor. Conversely, strain can also be expressed as a linear combination of stresses (**Equation II**):

$$\varepsilon_{ij} = S_{ijkl}\sigma_{kl}(\mathrm{i,j,k,l} \in 1,2,3) \tag{II}$$

where S_{ijkl} is the elastic compliance tensor (compliance matrix). The compliance matrix S and the stiffness matrix C have an inverse matrix relationship, and the expression of their mutual conversion is as follows (**Equation III**):

$$S = C^{-1} \tag{III}$$

The subscript i,j,k,l = 1,2,3 of the elastic stiffness tensor C_{ijkl} or the elastic compliance tensor S_{ijkl} corresponds to the x, y, and z axes. Combining the number of subscripts and the number of symmetry axes subscripts, it can be seen that the fourth-order stiffness tensor and the compliance tensor contain 81 elements, and the second-order stress tensor σ_{ij} and strain tensor C_{ijkl} contain nine elements. The inherent symmetry of stress tensor and strain tensor causes the stiffness matrix to exhibit symmetric characteristics (**Equation IV**),

$$C_{ijkl} = C_{jikl} = C_{jilk} = C_{jilk} \tag{IV}$$

According to the symmetry of the stiffness matrix in Equation V:

$$C_{ijkl} = C_{klij} \tag{V}$$

Therefore, by combining Equations IV and V, the anisotropic stiffness matrix can be represented by 21 independent elastic coefficients. The stiffness matrix C_{ijkl} (i,j,k,l=1,2,3) can be transformed into the stiffness matrix of i,j = 1,2,3,4,5,6, and the stress and strain tensors can be transformed into σ_i and ε_j by using the Voigt notation. Table 1 lists the Voight conversion rules.

Equations I and **II** then transform into **Equations VI** and **VII**:

$$\sigma_i = C_{ij}\varepsilon_j (i,j \in 1,2,\cdots,6) \quad \text{(VI)}$$

$$\varepsilon_i = S_{ij}\sigma_j (i,j \in 1,2,\cdots,6) \quad \text{(VII)}$$

The elastic matrix describing the relationship between stress and strain changes from 81 components to 21 independent components. Hence, the constitutive equation of the elastic matrix can be written as follows (**Equation VIII**):

$$\begin{bmatrix}\sigma_1\\ \sigma_2\\ \sigma_3\\ \sigma_4\\ \sigma_5\\ \sigma_6\end{bmatrix} = \begin{bmatrix}C_{11} & C_{12} & C_{13} & C_{14} & C_{15} & C_{16}\\ C_{12} & C_{22} & C_{23} & C_{24} & C_{25} & C_{26}\\ C_{13} & C_{23} & C_{33} & C_{34} & C_{35} & C_{36}\\ C_{14} & C_{24} & C_{34} & C_{44} & C_{45} & C_{46}\\ C_{15} & C_{25} & C_{35} & C_{45} & C_{55} & C_{56}\\ C_{16} & C_{26} & C_{36} & C_{46} & C_{56} & C_{66}\end{bmatrix}\begin{bmatrix}\varepsilon_1\\ \varepsilon_2\\ \varepsilon_3\\ \varepsilon_4\\ \varepsilon_5\\ \varepsilon_6\end{bmatrix} \quad \text{(VIII)}$$

The stiffness matrix in Equation VIII contains 21 elastic constants, which are generally considered independent in fully anisotropic media. However, in many cases, several elements of the stiffness matrix are either zero or constrained by symmetry. Moreover, not all nonzero stiffness elements are necessarily independent—for example, in transversely isotropic media. Typically, the greater the number of zero or constrained elements, the higher the degree of inherent symmetry in the elastic system of the medium.

The study of the elastic matrix in anisotropic media is typically conducted within the context of a constitutive coordinate system. However, due to the actual stratigraphic conditions, the constitutive coordinate system used for simulating complex anisotropic media may not align with the observed coordinate system. Therefore, a coordinate transformation is needed to unify elastic matrices across different coordinate systems. In the anisotropic media theory, the classification of anisotropic media is based on the angle between the medium's symmetry axis and the observation coordinate system.

Table 1. Voigt symbol conversion rules

Values for *ij* or *kl*	Values for *i* or *j*
11	1
22	2
33	3
23 or 32	4
31 or 13	5
12 or 21	6

Two steps are typically required to transform a complex anisotropic medium into the observation coordinate system. First, the stiffness tensor is constructed in the material (constitutive) coordinate system. Then, a Bond transformation is applied to rotate the stiffness tensor into the observation coordinate system. It is important to note that the Bond transformation strictly applies to the fourth-rank stiffness tensor, not to the 6 × 6 stiffness matrix obtained using Voigt's notation. This coordinate transformation process is essential for accurately representing anisotropic media in complex stratigraphic settings.

Assuming that the observation coordinate system and the constitutive coordinate system are *Oxyz* and *Ox'y'z'*, respectively, the direction cosine relationship between the observation coordinate system and the constitutive coordinate system (coordinate axis) in the Bond transformation is shown in Table 2.

Assuming that the stress tensor, strain tensor, stiffness matrix, and compliance matrix under the observation coordinate system and the constitutive coordinate system are σ, ε, C, and S and σ', ε', C', and S', respectively, according to the Bond coordinate transformation, the stress and strain transformation under different coordinate systems can be expressed as **Equations IX–XI**:

$$\sigma = M \cdot \sigma' \quad \text{(IX)}$$

$$\varepsilon = M^T \cdot \varepsilon' \quad \text{(X)}$$

$$M = \begin{bmatrix}\alpha_1^2 & \beta_1^2 & \gamma_1^2 & 2\beta_1\gamma_1 & 2\alpha_1\gamma_1 & 2\alpha_1\beta_1\\ \alpha_2^2 & \beta_2^2 & \gamma_2^2 & 2\beta_2\gamma_2 & 2\alpha_2\gamma_2 & 2\alpha_2\beta_2\\ \alpha_3^2 & \beta_3^2 & \gamma_3^2 & 2\beta_3\gamma_3 & 2\alpha_3\gamma_3 & 2\alpha_3\beta_3\\ \alpha_2\alpha_3 & \beta_2\beta_3 & \gamma_2\gamma_3 & \beta_2\gamma_3+\beta_3\gamma_2 & \gamma_2\alpha_3+\gamma_3\alpha_2 & \alpha_2\beta_3+\alpha_3\beta_2\\ \alpha_1\alpha_3 & \beta_1\beta_3 & \gamma_1\gamma_3 & \beta_1\gamma_3+\beta_3\gamma_1 & \gamma_1\alpha_3+\gamma_3\alpha_1 & \alpha_1\beta_3+\alpha_3\beta_1\\ \alpha_1\alpha_2 & \beta_1\beta_2 & \gamma_1\gamma_2 & \beta_1\gamma_2+\beta_2\gamma_1 & \gamma_1\alpha_2+\gamma_2\alpha_1 & \alpha_1\beta_2+\alpha_2\beta_1\end{bmatrix} \quad \text{(XI)}$$

Through derivation, we can get **Equation XII**:

$$\sigma = M \cdot C' \cdot M^T \cdot \varepsilon \quad \text{(XII)}$$

The stiffness matrix constitutive equation can be used to obtain **Equation XIII**:

$$C = M \cdot C' \cdot M^T \quad \text{(XIII)}$$

Table 2. The direction cosine relationship between the observation and the constitutive coordinate system (axis)

Axis	*x'*	*y'*	*z'*
x	α_1	β_1	γ_1
y	α_2	β_2	γ_2
z	α_3	β_3	γ_3

Similarly, the relationship between strain and stress is as follows (**Equations XIV–XVI**):

$$\sigma = N^T \cdot \sigma' \qquad \text{(XIV)}$$

$$\varepsilon = N \cdot \varepsilon' \qquad \text{(XV)}$$

$$N = \begin{bmatrix} \alpha_1^2 & \beta_1^2 & \gamma_1^2 & \beta_1\gamma_1 & \alpha_1\gamma_1 & \alpha_1\beta_1 \\ \alpha_2^2 & \beta_2^2 & \gamma_2^2 & \beta_2\gamma_2 & \alpha_2\gamma_2 & \alpha_2\beta_2 \\ \alpha_3^2 & \beta_3^2 & \gamma_3^2 & \beta_3\gamma_3 & \alpha_3\gamma_3 & \alpha_3\beta_3 \\ 2\alpha_2\alpha_3 & 2\beta_2\beta_3 & 2\gamma_2\gamma_3 & \beta_2\gamma_3+\beta_3\gamma_2 & \gamma_2\alpha_3+\gamma_3\alpha_2 & \alpha_2\beta_3+\alpha_3\beta_2 \\ 2\alpha_1\alpha_3 & 2\beta_1\beta_3 & 2\gamma_1\gamma_3 & \beta_1\gamma_3+\beta_3\gamma_1 & \gamma_1\alpha_3+\gamma_3\alpha_1 & \alpha_1\beta_3+\alpha_3\beta_1 \\ 2\alpha_1\alpha_2 & 2\beta_1\beta_2 & 2\gamma_1\gamma_2 & \beta_1\gamma_2+\beta_2\gamma_1 & \gamma_1\alpha_2+\gamma_2\alpha_1 & \alpha_1\beta_2+\alpha_2\beta_1 \end{bmatrix} \qquad \text{(XVI)}$$

Through derivation, we can get **Equation XVII**:

$$\varepsilon = N \cdot S^{'} \cdot N^T \cdot \sigma \qquad \text{(XVII)}$$

The stiffness matrix constitutive equation can be used to obtain **Equation XVIII**:

$$S = N \cdot S^{'} \cdot N^T \qquad \text{(XVIII)}$$

The matrices M and N are the Bond transformation matrices of the stiffness matrix and the compliance matrix, respectively, and T represents the transpose.

2.2. Derivation of the *in situ* stress formula for the TTI medium

In 1989, Crampin[1] classified various anisotropic media by analyzing their stiffness matrices and the number of independent elastic parameters, based on the symmetry of the medium. Isotropy refers to a medium whose elastic properties are the same in all directions and do not change with the direction of wave propagation. It is the simplest type of medium and can be considered a special case of anisotropy. While the complete isotropic medium is a simplification for geophysical research, real underground media are composed of superimposed lithologic strata, where the same strata exhibit uniform geophysical properties, thus behaving isotropically.

In anisotropic media theory, a TI medium exhibits rotational symmetry about a single axis. In such media, the material properties are isotropic within the plane perpendicular to the symmetry axis—known as the isotropy plane—and vary only with the angle between the wave propagation direction and the symmetry axis.[32,33] TI media can be further classified based on the direction of the symmetry axis into VTI media (vertical symmetry axis), HTI media (horizontal symmetry axis), and TTI media (tilted symmetry axis). Figure 1 illustrates a schematic of TI media, which have different symmetry axes and can be transformed into one another through rotation.

Although most natural fractures are vertical or subvertical, tectonic processes can result in fractures that are inclined at an angle to the stratigraphy. Monoclinic media are typically used to describe scenarios involving two sets of intersecting vertical fractures embedded in a VTI or isotropic background (Figure 2A and B), or a VTI background containing a single set of inclined fractures (Figure 2C).

In a TTI medium, the anisotropy can be regarded as a result of the rotation of either a VTI or an HTI medium by a certain angle. The stiffness (or compliance) properties of a TTI medium are obtained by applying the Bond transformation to the fourth-rank stiffness (or compliance) tensor of the corresponding VTI or HTI medium. It should be noted that

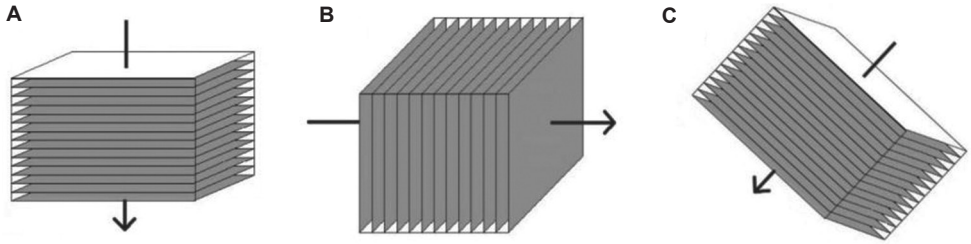

Figure 1. Diagram of the transversely isotropic media. (A) Vertically transversely isotropic medium, (B) horizontally transversely isotropic medium, and (C) tilted transversely isotropic medium

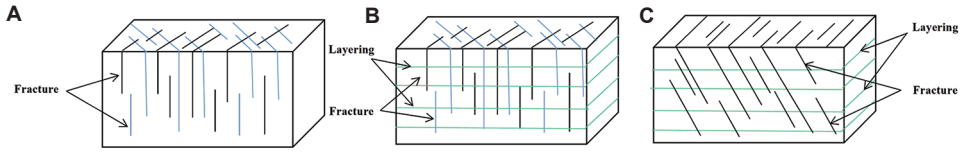

Figure 2. Diagram of monoclinic media. (A) Two groups of intersecting vertical fracture groups developed in an isotropic background medium. (B) Two groups of intersecting vertical fracture groups developed in a vertically transversely isotropic (VTI) background medium. (C) A group of inclined fractures developed in the VTI background media

the Bond transformation applies to the full tensor, not to the 6×6 matrix representation used in Voigt's notation.

In the subsequent derivation of this paper, the TTI medium is assumed to be formed by rotating a VTI medium. According to the definition of the linear slip model, when fractures develop horizontally (i.e., when the symmetry axis is vertical), the compliance tensor of the surrounding rock S_b can be expressed in terms of Young's modulus E and Poisson's ratio v as follows (**Equation XIX**):

$$S_b = \begin{pmatrix} \frac{1}{E} & \frac{-v}{E} & \frac{-v}{E} & 0 & 0 & 0 \\ \frac{-v}{E} & \frac{1}{E} & \frac{-v}{E} & 0 & 0 & 0 \\ \frac{-v}{E} & \frac{-v}{E} & \frac{1}{E} & 0 & 0 & 0 \\ 0 & 0 & 0 & \frac{1}{\mu} & 0 & 0 \\ 0 & 0 & 0 & 0 & \frac{1}{\mu} & 0 \\ 0 & 0 & 0 & 0 & 0 & \frac{1}{\mu} \end{pmatrix}_{6\times6} \quad \text{(XIX)}$$

where μ is the Lamé coefficient, which characterizes the rock's resistance to shear deformation. The additional compliance tensor S_f caused by fractures can be expressed as **Equation XX**:

$$S_f = \begin{pmatrix} 0 & 0 & 0 & 0 & 0 & 0 \\ 0 & 0 & 0 & 0 & 0 & 0 \\ 0 & 0 & Z_N & 0 & 0 & 0 \\ 0 & 0 & 0 & Z_T & 0 & 0 \\ 0 & 0 & 0 & 0 & Z_T & 0 \\ 0 & 0 & 0 & 0 & 0 & 0 \end{pmatrix}_{6\times6} \quad \text{(XX)}$$

where, Z_N is the normal compliance tensor of the fracture surface, representing the unit normal displacement (deformation) caused by a unit normal stress. Z_T is the tangential compliance tensor of the fracture surface, representing the unit tangential displacement caused by a unit tangential stress (parallel to the contact surface). By incorporating the linear slip theory and the Bond transformation, the effective compliance tensor of the TTI medium, S_T, can be expressed as the sum of the compliance tensor of the rock skeleton, S_b, and the compliance tensor of microcracks in the rock, S_f, after applying the Bond transformation. Thus, the effective compliance tensor of the TTI medium, S_T, can be written as **Equations XXI** and **XXII (see page no 20)**:

$$S_T = S_b + N_\theta S_f N_\theta^T \quad \text{(XXI)}$$

Substituting the compliance matrix of TTI medium into Hooke's law can result in **Equation XXIII**:

$$\begin{bmatrix} \varepsilon_1 \\ \varepsilon_2 \\ \varepsilon_3 \\ \varepsilon_4 \\ \varepsilon_5 \\ \varepsilon_6 \end{bmatrix} = \begin{bmatrix} S_{11t} & S_{12t} & S_{13t} & 0 & S_{15t} & 0 \\ S_{21t} & S_{22t} & S_{23t} & 0 & S_{25t} & 0 \\ S_{31t} & S_{32t} & S_{33t} & 0 & S_{35t} & 0 \\ 0 & 0 & 0 & S_{44t} & 0 & S_{46t} \\ S_{51t} & S_{52t} & S_{53t} & 0 & S_{55t} & 0 \\ 0 & 0 & 0 & S_{64t} & 0 & S_{66t} \end{bmatrix} \begin{bmatrix} \sigma_1 \\ \sigma_2 \\ \sigma_3 \\ \sigma_4 \\ \sigma_5 \\ \sigma_6 \end{bmatrix} \quad \text{(XXIII)}$$

Among them, S_{ijt} is the elastic compliance tensor of the TTI medium. σ_1, σ_2, and σ_3 the principal stresses are in the three principal directions. σ_4, σ_5, and σ_6 are shear stresses.

Iverson's theory states that there are vertical principal stress and two horizontal stresses in anisotropic rocks.[34] Assuming that the horizontal stresses are not equal and assuming that the underground rocks are constrained, that is, they are immobile, then the horizontal strain (ε_x, ε_y) is equal to zero. According to **Equation XXIII**, the expression of strain and stress in the horizontal direction is expressed in **Equations XXIV** and **XXV**:

$$\varepsilon_x = \varepsilon_1 = S_{11t}\sigma_x + S_{12t}\sigma_y + S_{13t}\sigma_z + S_{15t}\sigma_{zx} = 0 \quad \text{(XXIV)}$$

$$\varepsilon_y = \varepsilon_2 = S_{21t}\sigma_x + S_{22t}\sigma_y + S_{23t}\sigma_z + S_{25t}\sigma_{zx} = 0 \quad \text{(XXV)}$$

In *in situ* stress prediction, researchers typically consider only the three principal stresses: vertical stress, minimum horizontal principal stress, and maximum horizontal principal stress. Therefore, this paper disregards the influence of tangential stress σ_5 and focuses solely on the relationship among these three principal stresses. The final expressions for strain and stress in the horizontal direction are expressed in **Equations XXVI** and **XXVII**:

$$\varepsilon_x = \varepsilon_1 = S_{11t}\sigma_x + S_{12t}\sigma_y + S_{13t}\sigma_z = 0 \quad \text{(XXVI)}$$

$$\varepsilon_y = \varepsilon_2 = S_{21t}\sigma_x + S_{22t}\sigma_y + S_{23t}\sigma_z = 0 \quad \text{(XXVII)}$$

By solving equations through simultaneous equations, the expressions for the horizontal minimum principal stress σ_{xt} and horizontal maximum principal stress σ_{yt} of TTI medium can be obtained (**Equations XXVIII** and **XXIX**):

$$\sigma_{xt} = \sigma_z \frac{S_{12t}S_{23t} - S_{13t}S_{22t}}{S_{11t}S_{22t} - S_{12t}^2} \quad \text{(XXVIII)}$$

$$\sigma_{yt} = \sigma_z \frac{S_{12t}S_{13t} - S_{11t}S_{23t}}{S_{11t}S_{22t} - S_{12t}^2} \quad \text{(XXIX)}$$

The vertical stress σ_z is obtained by integrating the density. The expression for vertical stress σ_z is expressed in **Equation XXX**:

$$\sigma_z = \int_0^H g\rho(\mathrm{h})\,\mathrm{d}(\mathrm{h}) \quad \text{(XXX)}$$

In the formula, h is the depth, g is the gravitational acceleration, and p (h) is the density at depth.

Bringing the constant term of the compliance matrix into it yields the corresponding stress expressions in **Equations XXXI** and **XXXII**:

$$\sigma_{xt} = \sigma_z \left(\frac{\upsilon + \upsilon^2 + \frac{1}{4}E\left(Z_T - Z_N\right)\sin^2(2\theta)}{1 - \upsilon^2 + EZ_N \sin^4(\theta) + \frac{1}{4}EZ_T \sin^2(2\theta)} \right) \quad \text{(XXXI)}$$

$$\sigma_{yt} = \sigma_z \upsilon \left(\frac{1 + \upsilon - EZ_N(\frac{1}{4}\sin^2(2\theta) - \sin^4(\theta)) + \frac{1}{2}EZ_T \sin^2(2\theta)}{1 - \upsilon^2 + EZ_N \sin^4(\theta) + \frac{1}{4}EZ_T \sin^2(2\theta)} \right) \quad \text{(XXXII)}$$

The vertical stress σ_z can be estimated using seismic or logging data. By integrating the pre-stack wide-azimuth seismic inversion to derive elastic and anisotropic parameters and then substituting them into **Equations XXXI** and **XXXII**, the horizontal minimum principal stress and horizontal maximum principal stress of the TTI medium can be predicted. Furthermore, using **Equations XXXI** and **XXXII**, the TDHSR can be calculated as follows (**Equation XXXIII**):

$$TDHSR = \frac{\sigma_{yt} - \sigma_{xt}}{\sigma_{yt}} = \frac{E(4\nu Z_N \sin^4(\theta) + ((1-\nu)Z_N + (2\nu - 1)Z_T)\sin^2(2\theta))}{\nu(4 + 4\nu + EZ_N(4\sin^4(\theta) - \sin^2(2\theta)) + 2EZ_T \sin^2(2\theta))} \quad \text{(XXXIII)}$$

The tilted transverse isotropy DHSR represents the difference in ratio between the maximum and minimum horizontal principal stresses in a TTI medium. It is a crucial parameter for evaluating shale fracturability and the potential to form a fracture network. When TDHSR is high, hydraulic fracturing tends to generate parallel fractures aligned with the direction of the maximum horizontal principal stress, resulting in non-intersecting fracture planes that hinder shale oil and gas flow. Conversely, when TDHSR is low, hydraulic fracturing can induce fractures in multiple directions, forming an interlaced fracture network that enhances oil and gas migration. Therefore, during fracturing operations, targeting areas with low TDHSR values can help achieve a more effective shale reservoir stimulation.

2.3. Parameter correlation analysis: derivation of the *in situ* stress formula for monoclinic medium

Compared to an HTI medium, which accounts only for the influence of vertical fractures, an OA medium considers both the effect of vertical fractures and the intrinsic anisotropy of the host rock. This intrinsic anisotropy may result not only from the horizontal bedding but also from the inherent anisotropic nature of shale layers or other types of VTI formations. Building on the OA medium, a monoclinic medium further accounts for the fact that fractures are not strictly vertical but are often inclined due to geological structural influences, making it a more realistic representation of actual shale formations. It can be regarded as a result of the combined effects of inclined fractures (which can be considered a TTI medium) and the horizontal bedding of a VTI medium. Therefore, by integrating the linear slip theory and the Bond transformation, the effective compliance tensor, S_m, of the monoclinic medium can be expressed as the sum of the compliance tensor, S_{VTI}, of the VTI medium, which represents the horizontal bedding background, and the compliance tensor, S_f, of inclined fractures after applying the Bond transformation.

The compliance matrix of VTI medium is presented in **Equation XXXIV (see page no 20)**:

The compliance matrix of inclined fractures after Bond transformation $N_\theta S_f N_\theta^T$ is expressed in

Equation XXXV (see page no 20):

According to the Bond transformation, the compliance matrix of a background VTI medium is transformed accordingly. The effective compliance tensor of the monoclinic medium, S_M, can be written as **Equation XXXVI**:

$$S_M = S_{VTI} + N_\theta S_f N_\theta^T \quad \text{(XXXVI)}$$

Substituting the compliance matrix of the monoclinic medium into Hooke's law can result in the matrix presented in **Equation XXXVII**:

$$\begin{bmatrix}\varepsilon_1\\ \varepsilon_2\\ \varepsilon_3\\ \varepsilon_4\\ \varepsilon_5\\ \varepsilon_6\end{bmatrix}=\begin{bmatrix}S_{11m} & S_{12m} & S_{13m} & 0 & S_{15m} & 0\\ S_{21m} & S_{22m} & S_{23m} & 0 & S_{25m} & 0\\ S_{31m} & S_{32m} & S_{33m} & 0 & S_{35m} & 0\\ 0 & 0 & 0 & S_{44m} & 0 & S_{46m}\\ S_{51m} & S_{52m} & S_{53m} & 0 & S_{55m} & 0\\ 0 & 0 & 0 & S_{64m} & 0 & S_{66m}\end{bmatrix}\begin{bmatrix}\sigma_1\\ \sigma_2\\ \sigma_3\\ \sigma_4\\ \sigma_5\\ \sigma_6\end{bmatrix} \quad \text{(XXXVII)}$$

The elements in **Equation XXXVII** are explained in **Equations AI–AXII** in the Appendix A. As in the derivation of the TTI medium formula in the previous text, assuming that there are three principal stresses, the horizontal stresses are not equal, the rock is constrained and cannot move, and the influence of shear stress is ignored. At this time, both the shear stress and the horizontal strain are 0 (**Equations XXXVIII** and **XXXIX**):[34]

$$\varepsilon_x=\varepsilon_1=S_{11m}\sigma_x+S_{12m}\sigma_y+S_{13m}\sigma_z=0 \quad \text{(XXXVIII)}$$

$$\varepsilon_y=\varepsilon_2=S_{21m}\sigma_x+S_{22m}\sigma_y+S_{23m}\sigma_z=0 \quad \text{(XXXIX)}$$

By solving equations through simultaneous equations, the expressions for the horizontal minimum principal stress σ_{xm} and horizontal maximum principal stress σ_{ym} of the monoclinic medium can be obtained through **Equations XL** and **XLI**:

$$\sigma_{xm}=\sigma_z\frac{S_{12m}S_{23m}-S_{13m}S_{22m}}{S_{11m}S_{22m}-S_{12m}^2} \quad \text{(XL)}$$

$$\sigma_{ym}=\sigma_z\frac{S_{12m}S_{13m}-S_{11m}S_{23m}}{S_{11m}S_{22m}-S_{12m}^2} \quad \text{(XLI)}$$

The vertical stress is obtained by integrating the density. Bringing the constant term of the compliance matrix into it yields the corresponding stress expression in **Equations XLII** and **XLIII**:

$$\sigma_{xm}=\sigma_z\left(\begin{array}{l}\left(\begin{array}{l}\sin^2(2\theta)(Z_N-Z_T)\\ \left(\begin{array}{l}M^2(\delta-\varepsilon)-(\delta+1)\mu M+\\ \mu\left(\mu-\sqrt{(M-\mu)(-\mu+2\delta M+M)}\right)\end{array}\right)\\ +2\left(\sqrt{(M-\mu)(-\mu+2\delta M+M)}-\mu\right)\end{array}\right)\\ \hline 2M-\left(\begin{array}{l}M^2(\delta-\varepsilon)-(\delta+1)\mu M+\\ \mu\left(\mu-\sqrt{(M-\mu)(-\mu+2\delta M+M)}\right)\end{array}\right)\\ \left(4Z_N\sin(\theta)^4+Z_T\sin^2(2\theta)\right)\end{array}\right) \quad \text{(XLII)}$$

$$\sigma_{ym}=\sigma_z\frac{\left(\begin{array}{l}\sin^2(2\theta)\left(\begin{array}{l}M^2(\delta-\varepsilon)(Z_N-Z_T)\\ +\mu M(2\gamma-\delta)(Z_N-Z_T)\\ -\mu\left(\sqrt{(M-\mu)(-\mu+2\delta M+M)}-\mu\right)\\ (Z_N-2(\gamma+1)Z_T)\end{array}\right)\\ +2\left(\sqrt{(M-\mu)(-\mu+2\delta M+M)}-\mu\right)\\ +4(2\gamma+1)\mu Z_N\sin(\theta)^4\\ \left(\sqrt{(M-\mu)(-\mu+2\delta M+M)}-\mu\right)\end{array}\right)}{\left(\begin{array}{l}(\delta+1)\mu M-M^2(\delta-\varepsilon)\\ -\mu\left(\mu-\sqrt{(M-\mu)(-\mu+2\delta M+M)}\right)\end{array}\right)\\ \left(4Z_N\sin(\theta)^4+Z_T\sin^2(2\theta)\right)+2M} \quad \text{(XLIII)}$$

The vertical stress can be estimated using seismic or logging data. By integrating the pre-stack wide-azimuth seismic inversion to obtain elastic and anisotropic parameters and then substituting them into **Equations XLII** and **XLIII**, the horizontal minimum principal stress and horizontal maximum principal stress of the monoclinic medium can be predicted. Furthermore, using **Equations XLII** and **XLIII**, the MDHSR can be calculated as follows through **Equation XLIV**:

$$MDHSR=\frac{\sigma_{ym}-\sigma_{xm}}{\sigma_{ym}}$$

$$(2\gamma+1)\mu\left(\begin{array}{l}4Z_N\sin(\theta)^4\\ \left(\mu-\sqrt{(M-\mu)(-\mu+2\delta M+M)}\right)\\ +\sin^2(2\theta)\left(\begin{array}{l}M(Z_T-Z_N)+\\ Z_T\left(\mu-\sqrt{(M-\mu)(-\mu+2\delta M+M)}\right)\end{array}\right)\end{array}\right)$$

$$=\frac{\left(\begin{array}{l}-M^2(\delta-\varepsilon)(Z_N-Z_T)+\mu M(2\gamma-\delta)\\ (-(Z_N-Z_T))+\mu\left(\sqrt{(M-\mu)(-\mu+2\delta M+M)}-\mu\right)\\ (Z_N-2(\gamma+1)Z_T)\end{array}\right)}{2\mu+\sin^2(2\theta)}$$

$$-2\sqrt{(M-\mu)(-\mu+2\delta M+M)}$$

$$-4(2\gamma+1)\mu Z_N\sin(\theta)^4\left(\sqrt{(M-\mu)(-\mu+2\delta M+M)}-\mu\right) \quad \text{(XLIV)}$$

2.4. Verification of the tilted transverse isotropy DHSR

The *in situ* stress formulas for the TTI medium and monoclinic medium derived above must be verified

for their correctness. Therefore, the DHSR formula derived in this paper was compared with the DHSR for the HTI medium and the DHSR for the OA medium. This comparison involved degenerate cases to verify the accuracy of the formulas. Further analysis and verification of the DHSR for the HTI medium, as derived by Gray,[7] are given by the following formula in **Equation XLV**:

$$DHSR = \frac{\sigma_y - \sigma_x}{\sigma_y} = \frac{EZ_N}{1 + EZ_N + \nu} \tag{XLV}$$

The formula for the DHSR of the OA medium derived by Ma *et al.*[11] is presented in **Equation XLVI**:

$$ODHSR = \frac{2V_{S0}^2 \rho (2\gamma + 1) Z_N}{1 + 2V_{S0}^2 \rho (2\gamma + 1) Z_N} \tag{XLVI}$$

Among them, $Z_N = \frac{\delta_N}{M(1-\delta_N)}$, M = λ + 2μ is the P-wave modulus.

The *in situ* stress formula derived for the TTI medium is based on the anisotropic media theory and establishes the relationship between stress and strain in TTI media through Hooke's law. By applying the assumptions of Iverson's theorem, the *in situ* stress formula expressed in terms of anisotropic and elastic parameters was obtained. Furthermore, the TDHSR was given by **Equation XXXIII**. The TTI medium can be considered as a complex medium obtained by rotating the VTI medium. The elastic matrix of the TTI medium consists of two parts: the isotropic background medium and the anisotropic component caused by fractures. When the inclination angle reached 90°, the strata were considered as an HTI medium. Therefore, by substituting the inclination angle of 90° into the principal stress formula and TDHSR formula derived in this paper, the results matched perfectly with the principal stress formula and DHSR formula of the HTI medium as derived by Gray (**Equation XLVII**). The workflow is illustrated in Figure 3. This comparison fully supports the validity of the *in situ* stress formula for the TTI medium, considering the influence of inclined fractures, as proposed in this paper.

$$\begin{aligned} TDHSR(\theta = 90^\circ) &= \frac{E(4\nu Z_N \sin^4(\theta) + ((1-\nu)Z_N + (2\nu - 1)Z_T)\sin^2(2\theta))}{\nu(4 + 4\nu + EZ_N(4\sin^4(\theta) - \sin^2(2\theta)) + 2EZ_T \sin^2(2\theta))} \\ &= \frac{EZ_N}{1 + EZ_N + \nu} = DHSR \end{aligned} \tag{XLVII}$$

2.5. Verification of the monoclinic DHSR

Following a similar approach to deriving the *in situ* stress formula for the TTI medium, the *in situ* stress formula for the monoclinic medium was derived from the theory of anisotropic media. Using Hooke's law, the relationship between stress and strain in the monoclinic medium was established. According to Iverson's theorem, the *in situ* stress formula, expressed in terms of anisotropic and elastic parameters, was obtained, along with the MDHSR for the monoclinic medium, given by **Equation XLIV**. For the monoclinic medium, it can be regarded as a result of the rotation of the vertical fractures assumed in the OA medium. The elastic matrix of the monoclinic medium consisted of a VTI medium component, representing horizontal strata, and a TTI medium component, representing inclined fractures. As the inclination angle increased, rotation occurred. When the inclination angle θ reached 90°, the medium was regarded as an OA medium. Therefore, by substituting an inclination angle of θ = 90° into the principal stress formula and MDHSR formula of the monoclinic medium derived in this paper, the formula degraded completely, yielding results that matched precisely with the principal stress formula and DHSR formula for the OA medium derived by Ma *et al.*[11] This fully supports the validity of the *in situ* stress formula for the monoclinic medium, considering the combined influence of inclined fractures and horizontal bedding.

Compared to the TTI medium, the monoclinic medium further incorporates the influence of horizontal bedding in strata, in addition to considering the effect of inclined fractures. In the *in situ* stress formula and the MDHSR, both the compliance parameters of the TTI medium (representing fractures) and the anisotropic parameters of the VTI medium (representing horizontal bedding) were present. It can be considered that when the influence of horizontal bedding was ignored in the monoclinic medium, the shale strata degenerated from the monoclinic medium to the TTI medium. To verify the rationality of the formula derived in this paper, we further simplified it by removing the anisotropic parameters from the *in situ* stress and MDHSR formulas of the monoclinic medium. Specifically, the parameters ε, δ and γ were set to zero. This step allowed for a more intuitive assessment of the formula's validity and ensured its broader applicability in practical scenarios. The resulting *in situ* stress and TDHSR formula, obtained after eliminating the anisotropic parameters, are presented in **Equations XLVIII–L**:

$$\sigma_x = \sigma_z \left(\frac{M - 2\mu + (Z_N - Z_T)(\mu - M)\mu \sin^2(2\theta)}{M(M-\mu)\mu\left(4Z_N \sin^4(\theta) + Z_T \sin^2(2\theta)\right)} \right) \quad \text{(XLVIII)}$$

$$\sigma_y = \sigma_z \left(\frac{(M-2\mu)\begin{pmatrix} 2 + 4Z_N \mu \sin^4(\theta) - (Z_N - 2Z_T) \\ \mu \sin^2(2\theta) \end{pmatrix}}{2\left(M + (M-\mu)\mu\left(4Z_N \sin^4(\theta) + Z_N \sin^2(2\theta)\right)\right)} \right) \quad \text{(XLIX)}$$

$$TDHSR = \frac{\mu\begin{pmatrix} 4Z_N \sin(\theta)^4 (M-2\mu) + \sin^2(2\theta) \\ (MZ_N - 2\mu Z_T) \end{pmatrix}}{(M-2\mu)\begin{pmatrix} 4\mu Z_N \sin(\theta)^4 - \mu \sin^2(2\theta) \\ (Z_N - 2Z_T) + 2 \end{pmatrix}} \quad \text{(L)}$$

In the transversely isotropic media, the relationship between the P-wave modulus, the S-wave modulus, the Young's modulus, and the Poisson's ratio can be expressed as follows (**Equations LI** & **LII**):

$$M = \frac{E(1-\nu)}{(1+\nu)(1-2\nu)} \quad \text{(LI)}$$

$$\mu = \frac{E}{2(1+\nu)} \quad \text{(LII)}$$

Substituting this relationship into **Equations XLVIII–L**, with transformations, we obtained **Equations LIII–LV**:

$$\sigma_x = \sigma_z \left(\frac{\upsilon + \upsilon^2 + \frac{1}{4}E(Z_T - Z_N)\sin^2(2\theta)}{1 - \upsilon^2 + EZ_N \sin^4(\theta) + \frac{1}{4}EZ_T \sin^2(2\theta)} \right) \quad \text{(LIII)}$$

$$\sigma_y = \sigma_z \upsilon \left(\frac{\begin{matrix} 1 + \upsilon - EZ_N\left(\frac{1}{4}\sin^2(2\theta) - \sin^4(\theta)\right) \\ + \frac{1}{2}EZ_T \sin^2(2\theta) \end{matrix}}{\begin{matrix} 1 - \upsilon^2 + EZ_N \sin^4(\theta) \\ + \frac{1}{4}EZ_T \sin^2(2\theta) \end{matrix}} \right) \quad \text{(LIV)}$$

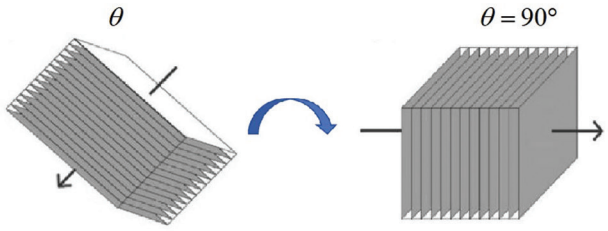

Step 1. $\theta = 90°$ ⟹ $\sin^2(2\theta) = 0 \quad \sin^4(\theta) = 1$

Step 2.

$$\sigma_{xt} = \sigma_z \left(\frac{\upsilon + \upsilon^2 + \frac{1}{4}E(Z_T - Z_N)\sin^2(2\theta(\theta = 90°))}{1 - \upsilon^2 + EZ_N \sin^4(\theta(\theta = 90°)) + \frac{1}{4}EZ_T \sin^2(2\theta(\theta = 90°))} \right) = \sigma_z \upsilon \left(\frac{1+\upsilon}{1-\upsilon^2 + EZ_N} \right)$$

$$\sigma_{yt} = \sigma_z \upsilon \left(\frac{1 + \upsilon - EZ_N\left(\frac{1}{4}\sin^2(2\theta(\theta = 90°)) - \sin^4(\theta(\theta = 90°))\right) + \frac{1}{2}EZ_T \sin^2(2\theta(\theta = 90°))}{1 - \upsilon^2 + EZ_N \sin^4(\theta(\theta = 90°)) + \frac{1}{4}EZ_T \sin^2(2\theta(\theta = 90°))} \right) = \sigma_z \upsilon \left(\frac{1 + \upsilon + EZ_N}{1 - \upsilon^2 + EZ_N} \right)$$

Step 3.

$$\frac{\sigma_{yt} - \sigma_{xt}}{\sigma_{yt}} = \frac{\sigma_z \upsilon \left(\frac{1+\upsilon+EZ_N}{1-\upsilon^2+EZ_N} \right) - \sigma_z \upsilon \left(\frac{1+\upsilon}{1-\upsilon^2+EZ_N} \right)}{\sigma_z \upsilon \left(\frac{1+\upsilon+EZ_N}{1-\upsilon^2+EZ_N} \right)} = \frac{EZ_N}{1 + EZ_N + \nu} = DHSR$$

Figure 3. Workflow for converting the tilted transverse isotropy differential horizontal stress ratio to the differential horizontal stress ratio (DHSR)
Note: θ represents the fracture dip angle, E represents the Young's modulus, and v represents the Poisson's ratio. Z_N is the normal compliance tensor of the fracture surface, representing the unit normal displacement (deformation) caused by a unit normal stress. Z_T is the tangential compliance tensor of the fracture surface, representing the unit tangential displacement caused by a unit tangential stress (parallel to the contact surface). Z_N increases with increasing θ. Z_T depends only on 2θ, when $\theta = 90°$, $\sin 2\theta = 0$. Therefore, DHSR is independent of Z_T
Abbreviations: HTI: Horizontally transversely isotropic medium; TTI: Tilted transversely isotropic medium

$$TDHSR = \frac{E(4\nu Z_N \sin^4(\theta) + ((1-\nu)Z_N + (2\nu - 1)Z_T) \sin^2(2\theta))}{\nu(4 + 4\nu + EZ_N(4\sin^4(\theta) - \sin^2(2\theta)) + 2EZ_T \sin^2(2\theta))} \quad \text{(LV)}$$

Equations LIII–LV are consistent with the *in situ* stress and TDHSR formulas (**Equations XXXI–XXXIII**) of the TTI medium derived previously. The consistency of the two was mutually verified through formula degradation, thus proving the correctness of the *in situ* stress formulas of the two complex media derived in this paper.

3. Complex medium *in situ* stress sensitivity analysis

From the research and derivation of the complex medium *in situ* stress formulas presented earlier, it can be concluded that, compared to the DHSR of the HTI and OA media, which are controlled by a limited number of parameters, the TDHSR and MDHSR derived in this paper are influenced by a greater number of factors. To gain a deeper understanding of the *in situ* stress formula, the influence of individual parameters on the TDHSR and MDHSR formulas derived above was further studied through a controlled variable approach.

3.1. Influence of elastic parameters and anisotropic parameters on the tilted transverse isotropy DHSR

Taking the study of the influence of Young's modulus on the TDHSR as an example, assume that the Poisson's ratio of the TTI background medium is ν = 0.35. The Young's modulus increases by 2 GPa at each step, with the range spanning from 20 GPa to 40 GPa. The normal compliance and tangential compliance of fractures are given as Z_N = 2.5×10^{-12} and Z_T = 2.5×10^{-12}, respectively. The fracture dip angle starts at 0° and increases by 10° at each step, with a maximum dip angle of 90°. As the fracture dip angle changes, the influence of Young's modulus on the TDHSR is shown in Figure 4. When the fracture dip angle is 0°, the TTI medium degenerates into a VTI medium. According to Gray's assumption, TDHSR is zero at this point. For a fixed fracture dip angle, as Young's modulus increases, TDHSR shows a positive correlation. In other words, the greater the Young's modulus, the higher the TDHSR. Furthermore, with other parameters held constant, TDHSR exhibited a linear increase as the fracture inclination angle increased.

Following the same approach to study the influence of different parameters on TDHSR, it can be observed that as various parameters increase, TDHSR exhibits either an increasing or decreasing trend. When the stratum dip angle is 0°, TDHSR is zero. As the stratum dip angle increases, TDHSR shows an increasing trend. In particular, for tangential compliance, when the fracture dip angle reaches 90°, TDHSR remains unchanged with variations in tangential compliance. Through the derivation and analysis of the above formula, it can be concluded that when the TTI medium is rotated by 90° to become an HTI medium, the DHSR formula is given by **Equation XLV.** At this point, the tangential compliance term in the formula is eliminated, and the DHSR becomes independent of tangential compliance, resulting in a constant value.

Figure 5 shows the variation of TDHSR under the combined influence of anisotropic and elastic parameters. Taking Figure 5A as an example, TDHSR increased with both normal compliance and Young's modulus. TDHSR is more sensitive to normal compliance. From all the subplots in Figure 5, it can be observed that TDHSR is more sensitive to anisotropic parameters compared to elastic parameters. Consistent with the conclusions of the single-parameter sensitivity analysis, TDHSR increased linearly with the dip angle.

3.2. Influence of elastic parameters and anisotropic parameters on the monoclinic DHSR

Similarly, considering the study of the influence of the P-wave modulus on the MDHSR, assume that the shear wave modulus of the monoclinic background medium is μ = 10 GPa. The P-wave modulus M increases by 5 GPa at each step, with the range spanning from 25 GPa to 45 GPa. The anisotropic parameters are set as ε = 0, δ = 0 and γ = 0, while the normal weakness and tangential weakness of fractures are Δ_N = 0.35 and Δ_T = 0.1, respectively. The fracture dip angle starts at 0° and increases by 10° at each step, with a maximum dip angle of 90°. As the fracture dip angle changes, the influence of the P-wave modulus M on the MDHSR is shown in Figure 6. When the fracture dip angle is 0°, the monoclinic medium degenerates into a VTI medium. According to Gray's assumption, MDHSR is zero at this point. For a fixed fracture dip angle, as the P-wave modulus increases, MDHSR shows a negative correlation, indicating that a greater P-wave modulus results in a smaller MDHSR. With other parameters held constant, MDHSR exhibited a linear increase as the fracture dip angle increased. When the fracture dip angle reached 90°, MDHSR remained unchanged with variations in the P-wave modulus. Through the derivation and analysis of the above formula, it can be concluded that when the monoclinic medium is rotated by 90° to become an OA medium, the DHSR formula is given as **Equation XLVI**. At this point, the P-wave modulus M is eliminated from the formula, and the DHSR becomes independent of the P-wave modulus, resulting in a constant value.

When the dip angle of the ground layer or fracture is 0°, the monoclinic medium simplifies to a VTI medium. According to Gray's assumption, the MDHSR is 0 in this case. When the fracture dip angle remains fixed, the MDHSR exhibits a positive correlation with the anisotropy parameter ε, a negative correlation with the anisotropy parameter δ, and a positive correlation with the anisotropy parameter γ. However, when the fracture dip angle reaches 90°, the MDHSR remains unaffected by the anisotropy parameters.

Following the same approach to studying the influence of different parameters on MDHSR, it can be observed that as various parameters increase, MDHSR exhibits either an increasing or decreasing trend. When the stratum dip angle is 0°, MDHSR remains 0. As the stratum dip angle increases, MDHSR shows an increasing trend. Notably, for P-wave modulus, tangential compliance, and anisotropic parameters, when the fracture dip angle reaches 90°, MDHSR remains unchanged despite variations in these parameters. Through the derivation and analysis of the above formula, it can be concluded that when the monoclinic medium is rotated by 90° to become an OA medium, the DHSR is given in **Equation XLVI**. At this point, the parameter terms in the formula are eliminated, indicating that the DHSR is unaffected by these values and remains a constant.

Figure 7 illustrates the variation of MDHSR under the combined influence of anisotropic and elastic parameters. Taking Figure 7C as an example, MDHSR increases with both normal compliance and S-wave modulus. MDHSR is more sensitive to normal compliance. From all the subplots in Figure 7, it can be observed that MDHSR is more sensitive to anisotropic parameters compared to elastic parameters. Consistent with the conclusions of the single-parameter sensitivity analysis, MDHSR increases linearly with the dip angle.

4. Model example analysis

4.1. Methodology and workflow for *in situ* stress prediction

Based on the previously discussed stress characterization methods for complex media, a stress inversion approach grounded in complex medium theory can ultimately be established. This method primarily consists of five steps.

4.1.1. Seismic data preparation

To invert for the anisotropic parameters used in stress prediction, at least six azimuthal elastic impedance

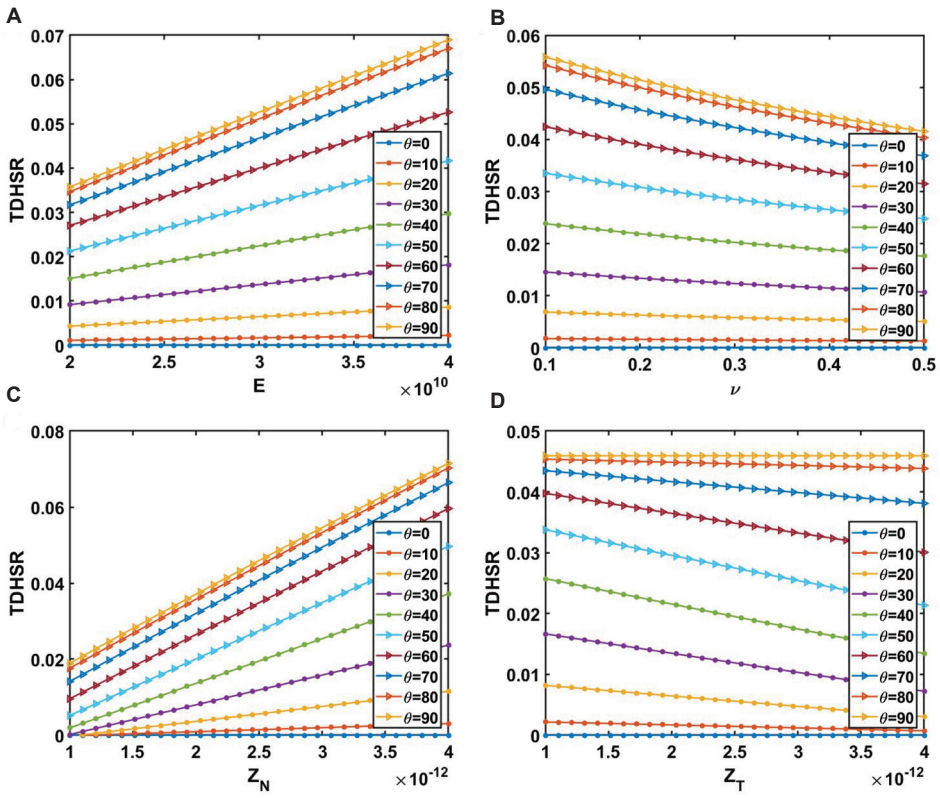

Figure 4. Influence of elastic parameters and anisotropic parameters on the tilted transverse isotropy differential horizontal stress ratio (TDHSR). (A) Young's modulus. (B) Poisson's ratio. (C) Normal compliance. (D) Tangential compliance

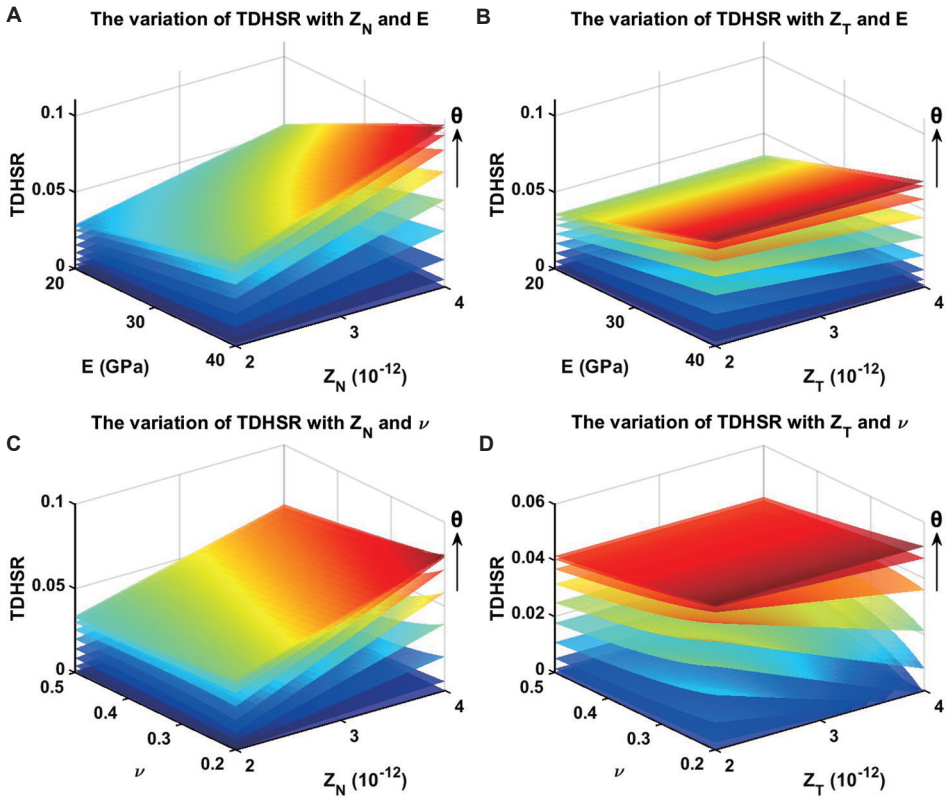

Figure 5. Influence of elastic parameters and anisotropic parameters on the tilted transverse isotropy differential horizontal stress ratio (TDHSR). (A) Normal compliance and Young's modulus. (B) Tangential compliance and Young's modulus. (C) Normal compliance and Poisson's ratio. (D) Tangential compliance and Poisson's ratio

(EI) data volumes are required. The wide-azimuth pre-stack seismic data are divided according to the azimuth rose diagram. Starting from zero degrees, six pre-stack seismic gathers are selected to ensure uniform azimuthal distribution and roughly equal fold coverage. The final selected data consist of six volumes—representing small, medium, and large incidence angles—at the two azimuths with the highest fold coverage.

4.1.2. Azimuthal elastic impedance inversion

Using the six partial-angle stacked seismic volumes, azimuthal EI inversion is performed individually for each volume. By incorporating rock physics information and constraints such as wavelets, well logs, seismic horizons, and low-frequency models, six azimuthal EI volumes are obtained through constrained elastic impedance inversion.

4.1.3. Elastic parameter inversion based on elastic impedance

The six-angle elastic impedance volumes are used as input to derive the complete volumes of P-wave velocity, S-wave velocity, density, and anisotropic parameters within the study area. Fracture compliance parameters can further be obtained through equation-based transformations.

4.1.4. Determination of formation and fracture dip angles

Given that this study focuses on stress prediction in shale formations with bedding or fracture dip (i.e., complex media), it is necessary to determine the dip angle. Due to its low cost and maturity, image logging is typically used to measure and determine the dip of formations and fractures.

4.1.5. Calculation of horizontal stress ratio and stress prediction

Once the elastic parameters, anisotropic parameters, and dip angles of formations and fractures required for stress calculation in complex media are obtained, the previously derived complex medium stress equations—based on linear slip theory, anisotropy theory, and Bond transformation—are used. Ultimately, the prediction of *in situ* stress is achieved by calculating the DHSR, either TDHSR or MDHSR, for complex media.

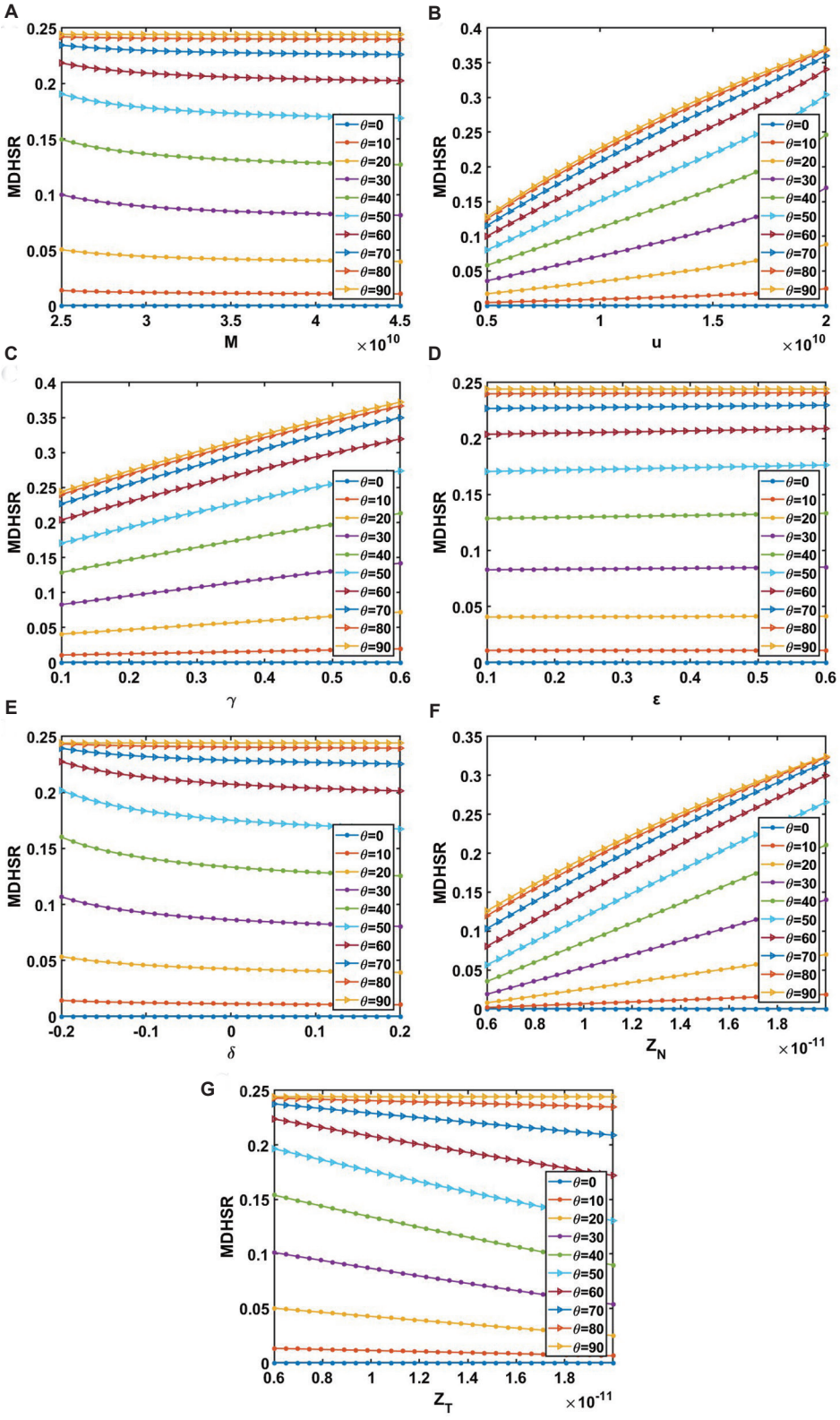

Figure 6. Influence of fracture compliance parameters on the monoclinic differential horizontal stress ratio (MDHSR). (A) P-wave modulus. (B) S-wave modulus. (C) Anisotropic parameter. (D) Anisotropic parameter. (E) Anisotropic parameter. (F) Normal compliance. (G) Tangential compliance

4.2. Field data experiment

To further validate the correctness of the *in situ* stress formula derived in this study, actual logging data must be used for trial calculations. The measured logging curve from Well A, located in the shale formation of the Sichuan Basin, China, was selected for this purpose. A fractured shale formation petrophysical model was constructed to perform the model trial calculations. By inputting measured parameters such as P-wave and S-wave velocities, rock mineral composition, as well as the bulk modulus, shear modulus, and density of each component, along with water saturation and porosity, the anisotropic parameters and fracture compliance parameters required for the *in situ* stress formula were obtained. Figure 8 presents the anisotropic parameters ε, δ, and γ, the fracture normal compliance Z_N, the tangential compliance Z_T, Young's modulus, Poisson's ratio, P-wave modulus M, and S-wave modulus μ for Well A.

The stress measurement point on Well A was selected for model trial calculations. By comparing the DHSR at the measurement point with TDHSR, derived from the TTI medium theory, and MDHSR, derived from the monoclinic medium theory, an error analysis was conducted. Figure 8 presents a comparison of the DHSR at the measured point with TDHSR based on the TTI medium theory, while Figure 9 shows a comparison with MDHSR based on the monoclinic medium theory. As observed in the figures, both TDHSR and MDHSR calculations aligned closely with the measured DHSR, demonstrating the practical applicability of the formula derived in this study. An error analysis was performed on the results, as shown in Table 3, which presents the error analysis of DHSRs at different measurement points. The table indicates that the errors of TDHSR and MDHSR obtained from the model trial calculations fall within a reasonable range. By comparing the errors, it is evident that MDHSR, based on the monoclinic medium theory—which accounts for both horizontal stratification and inclined fractures—exhibited smaller errors and aligned more closely with the measured results than TDHSR, which is based on the TTI medium theory and only considers a single inclined stratum or fracture.

5. Discussion

It is important to acknowledge that the current validation of the TDHSR and MDHSR methods was based on

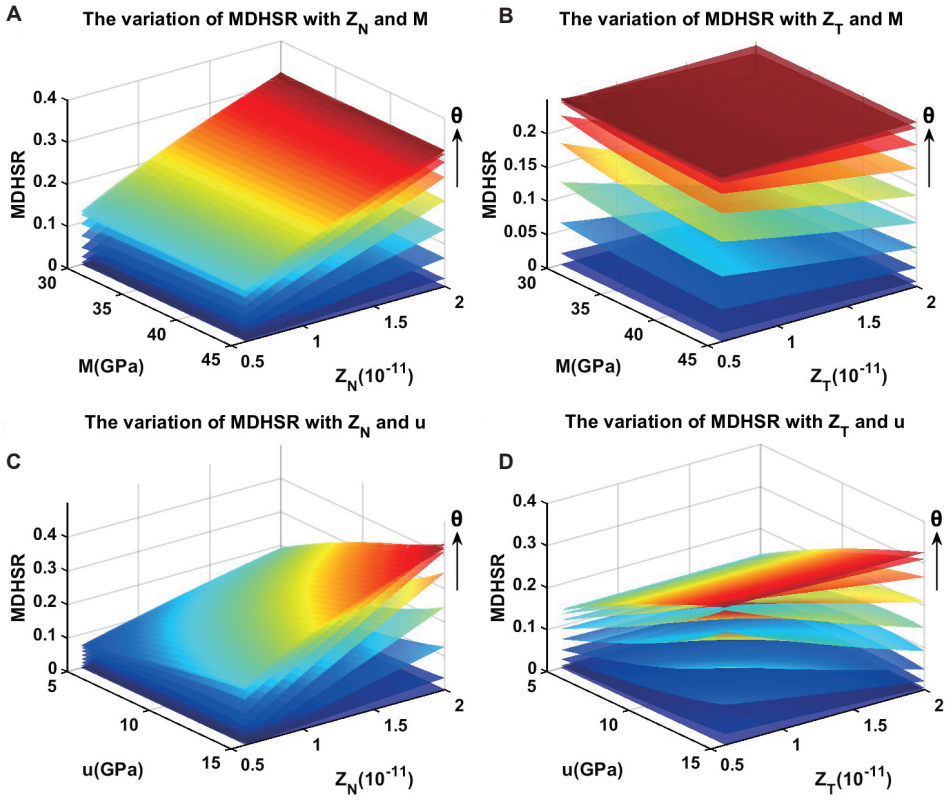

Figure 7. Influence of fracture compliance parameters on the monoclinic differential horizontal stress ratio (MDHSR). (A) Normal compliance and P-wave modulus. (B) Tangential compliance and P-wave modulus. (C) Normal compliance and S-wave modulus. (D) Tangential compliance and S-wave modulus

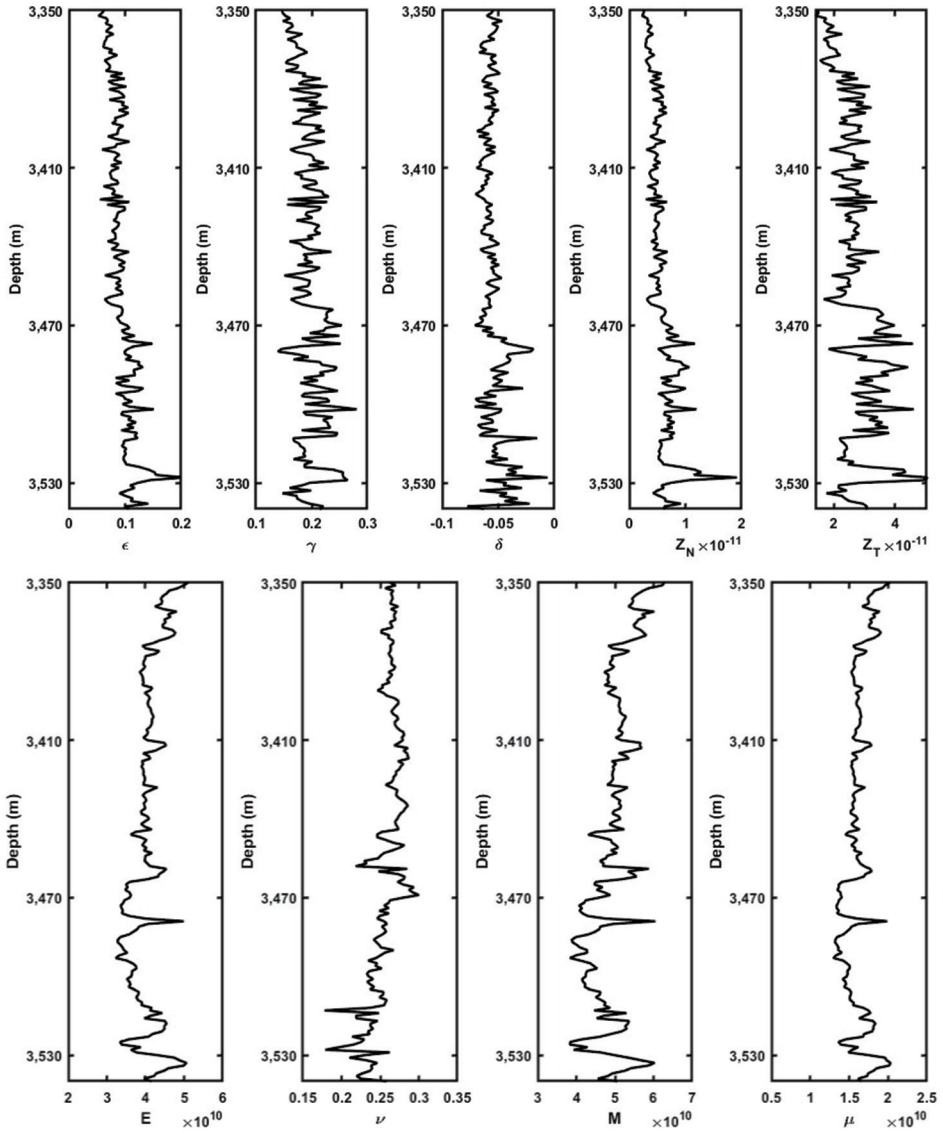

Figure 8. Elastic parameters and anisotropic parameters of Well A

data from a single well in the Sichuan Basin. While the method demonstrated promising accuracy for the studied well, its generalization to other geological settings requires caution. The Sichuan Basin's unique lithology and tectonic history may limit direct extrapolation to basins with differing diagenetic processes or structural complexities.

Future work should consider expanding the application and validation of the proposed methods using data from wells in other basins with diverse geological characteristics. This includes, for example, the Ordos Basin (characterized by stable cratonic settings), the Tarim Basin (with complex deep structures), and foreland basins with strong tectonic deformation. In addition, future work can explore formations with different structural types (e.g., anticlines, fault blocks) and lithologies (e.g., carbonate, sandstone, and tight shale formations). Furthermore, the use of synthetic seismic models and publicly available benchmark datasets should be considered to provide supplementary validation and to better isolate and understand the influence of specific parameters such as fracture dip, azimuthal anisotropy, and stratification. Multi-case verification will enhance the robustness and applicability of the TDHSR and MDHSR approaches, making them more adaptable to various exploration scenarios.

Table 3. Error analysis table of horizontal stress difference ratios at different measured points

Depth (m)	Measured horizontal maximum stress (Mpa)	Measured horizontal maximum stress (Mpa)	Horizontal stress difference ratio	TDHSR	Error	MDHSR	Error
3,483	101.4	86.3	0.149	0.135	9.4%	0.152	2.0%
3,490	102.3	90.5	0.115	0.105	8.7%	0.117	1.7%
3,501	104.6	88.5	0.153	0.141	7.8%	0.146	4.6%
3,508	103.2	88.9	0.139	0.126	9.4%	0.141	1.8%

Abbreviations: MDHSR: Monoclinic differential horizontal stress ratio; TDHSR: Tilted transverse isotropy differential horizontal stress ratio.

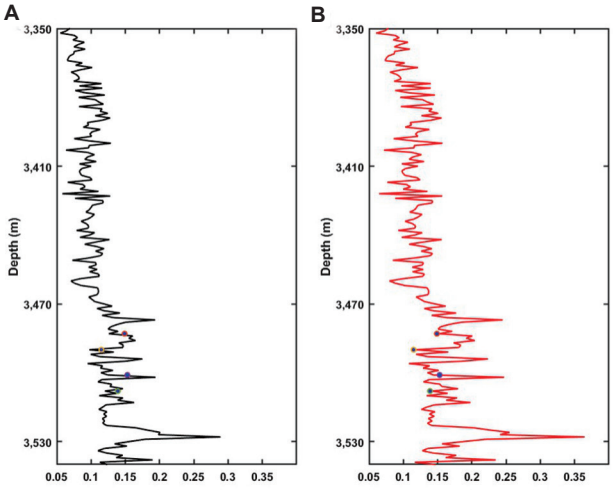

Figure 9. Comparison chart of horizontal stress difference ratio of measured points with the tilted transverse isotropy differential horizontal stress ratio (TDHSR) and the monoclinic differential horizontal stress ratio (MDHSR). (A) TDHSR based on TTI medium theory and (B) MDHSR based on monoclinic medium

6. Conclusion

In situ stress plays a crucial role in the formation and distribution of oil and gas reservoirs. The development and evolution of geological structures result from the action and variation of tectonic stress. The underground stress field influences rock layer deformation, fracture formation, and crack development. For instance, faults are formed due to the fracturing or sliding of strata under *in situ* stress. The type of faults can be assessed based on *in situ* stress prediction results. In addition, the variation of *in situ* stress differs across lithologies, allowing it to serve as an indicator of underground lithology. Therefore, predicting *in situ* stress holds significant research value. A thorough understanding of the *in situ* stress field enables the identification of potential oil and gas accumulation areas, providing essential guidance for exploration efforts.

This paper primarily investigated the seismic prediction method for *in situ* stress based on complex medium theory. It built upon existing seismic prediction methods derived from HTI and OA media while considering the impact of inclined fractures in actual shale formations. By incorporating the assumptions of Schoenberg and Iverson and utilizing the constitutive equation along with coordinate transformations of the elastic matrix, this study derived *in situ* stress formulas for both TTI and monoclinic media, leading to the corresponding DHSRs: TDHSR and MDHSR.

Finally, a model trial calculation was performed using actual logging data from a shale formation. The results demonstrated that the errors of TDHSR and MDHSR remained within a reasonable range. Compared to TDHSR, which was based on the TTI medium and considered only a single inclined stratum or fracture, MDHSR, derived from the monoclinic medium theory, accounted for both horizontal stratification and inclined fractures, leading to smaller errors and results that aligned more closely with the measured data. In conclusion, the TDHSR and MDHSR formulas derived in this study exhibited high accuracy and strong practical applicability.

Acknowledgments

None.

Funding

This research received no external funding.

Conflict of interest

The authors declare no conflicts of interest.

Author contributions

Conceptualization: Jun Cheng, Yaojie Chen
Data curation: Yaojie Chen
Formal analysis: Zhensen Sun
Investigation: Jun Cheng
Methodology: Zhensen Sun
Resources: Jun Cheng
Software: Yaojie Chen
Supervision: Jun Cheng
Validation: Jun Cheng, Zhensen Sun

Writing–original draft: Jun Cheng, Yaojie Chen
Writing–review & editing: Jun Cheng, Yaojie Chen

Availability of data

Due to confidentiality restrictions, the data analyzed in this study cannot be made available to readers.

References

1. Crampin S. The fracture criticality of crustal rocks. *Geophys J Int*. 1994;118(2):428-438.

   doi: 10.1111/j.1365-246X.1994.tb03974.x

2. Yin XY, Cao DP, Wang BL, Zong ZY. Research progress on fluid identification method based on pre-stack seismic inversion. *Oil Geophys Prospect*. 2014;49(1):22-34.

   doi: 10.13810/j.cnki.issn.1000-7210.2014.01.002

3. Du BY, Yang WY, Wang EL, Zhang GZ, Gao J. AVAZ inversion method for fracture media based on young's modulus, poisson's ratio and anisotropy gradient. *Oil Geophys Prospect*. 2015;54(2):218-225.

   doi: 10.3969/j.issn.1000-1441.2015.02.014

4. Zhang GZ, Chen JJ, Chen HZ, Ma GZ, Li CC, Yin XY. Study on *in-situ* stress prediction method based on shale rock physics equivalent model. *Chin J Geophys*. 2015;58(6):2112-2122.

5. Gray FD, Anderson PF, Logel J, Delbecq F, Schmidt D. Estimating *In-Situ*, Anisotropic, Principal Stresses from 3D Seismic. In: *EAGE Conference and Exhibition*; 2010.

6. Gray FD, Anderson PF, Corp A, Logel J, Delbecq F, Schmidt D. *Principle Stress Estimation in Shale Plays using 3D Seismic*. Boca Raton: GeoCanada; 2010.

7. Gray FD. *Methods and Systems for Estimating Stress using Seismic Data*. United States Patent Application no 20110182144A1; 2011.

8. Gray FD, Logel J, Delbecq F, Schmidt D, Schmid R. Estimation of stress and geomechanical properties using 3D seismic data. *First Break*. 2012;30(3):59-68.

   doi: 10.3997/1365-2397.2011042

9. Ruger A. Variation of P-wave reflectivity with offset and azimuth in anisotropic media. *Geophysics*. 1998;63(3):935-947.

   doi: 10.1190/1.1444405

10. Ge ZJ, Li JY, Chen XH, Yu X, Wu JL. TTI medium fracture parameter inversion based on bayesian linear AVAZ. *Chin J Geophys*. 2018;61(7):3008-3018.

    doi: 10.6038/cjg2018L0703

11. Ma N, Yin XY, Sun CY, Zong ZY. *In-situ* stress inversion method based on azimuthal seismic data. *Chin J Geophys*. 2018;61(2):697-706.

12. Ma N, Yin XY, Sun CY, Zong ZY. Seismic prediction method for *in-situ* stress based on orthotropic medium theory. *Chin J Geophys*. 2017;60(12):4766-4775.

13. Wang C. *Research on Pre-Stack Seismic Evaluation Method for Fracturability of Shale Gas Reservoirs*. Qingdao: China University of Petroleum (East China); 2018.

14. Wang C, Song WQ, Lin YH, Zhang YY, Gao QJ, Wei XW. The prediction method of *in-situ* stress based on pre-stack anisotropic parameter inversion. *Geophys Geochem Exploration*. 2020;44(1):141-148.

15. Li L, Zhang GZ. Estimation of fracture parameters and *in-situ* stress parameter based on extended azimuthal elastic impedance. *Chin J Geophys*. 2022;65(8):3172-3185.

16. Wang ZY, Zhang YP, Yang PK, Li SJ. *In situ* stress field inversion based on regularization theory and its applications. *Chin J Underground Space Eng*. 2023;19(2):751-757.

17. Bao T, Burghardt J. A Bayesian approach for *in-situ* stress prediction and uncertainty quantification for subsurface engineering. *Rock Mech Rock Eng*. 2022;55(8):4531-4548.

    doi: 10.1007/s00603-022-02857-0

18. Feng Y, Gao K, Lacasse S. Bayesian partial pooling to reduce uncertainty in overcoring rock stress estimation. *J Rock Mech Geotech Eng*. 2024;16(4):1192-1201.

    doi: 10.1016/j.jrmge.2023.05.003

19. Feng Y, Gao K, Mignan A, Li JW. Improving local mean stress estimation using Bayesian hierarchical modelling. *Int J Rock Mech Min Sci*. 2021;148:104924.

    doi: 10.1016/j.ijrmms.2021.104924

20. Feng Y, Bozorgzadeh N, Harrison JP. Bayesian analysis for uncertainty quantification of *in situ* stress data. *Int J Rock Mech Min Sci*. 2020;134:104381.

    doi: 10.1016/j.ijrmms.2020.104381

21. Moritz OZ, Oliver H. Bayesian quantification and reduction of uncertainties in 3D geomechanical-numerical models. *J Geophys Res Solid Earth*. 2023;128(1):1-23.

    doi: 10.1029/2022JB024855

22. Tonon F, Amadei B, Pan E. Bayesian estimation of rock mass boundary conditions with applications to the AECL underground research laboratory. *Int J Rock Mech Min Sci*. 2001;38(7):995-1027.

    doi: 10.1016/S1365-1609(01)00036-3

23. Leslie JM, Lawton DC. Structural Imaging Below Dipping Anisotropic Layers: Predictions from Seismic Modeling. In: *66th Annual International Meeting, Expanded Abstracts*. United States: SEG; 1996. p. 719-722.

24. Behera L, Tsvankin I. Migration velocity analysis for tilted transversely isotropic media. *Geophys Prospect*. 2009;57:13-26.

    doi: 10.1111/j.1365-2478.2008.00732.x

25. Tsvankin I. Moveout analysis for transversely isotropic media with a tilted symmetry axis. *Geophys Prospect*. 1997;45(3):479-512.

doi: 10.1046/j.1365-2478.1997.380278.x

26. Isaac JH, Lawton DC. A practical method for estimating effective parameters of anisotropy from reflection seismic data. *Geophysics*. 2004;69(3):681-689.

doi: 10.1190/1.1759454

27. Charles S, Mitchell DR, Holt RA, Lin JW, Mathewson J. Data-driven tomographic velocity analysis in tilted transversely isotropic media: A 3D case history from the Canadian foothills. *Geophysics*. 2008,73(5):261.

doi: 10.1190/1.2952915

28. Popov P, Qin G, Bi L, Kang Z, Li J. Multiphysics and multiscale methods for modeling fluid flow through naturally fractured carbonate karst reservoirs. *SPE Reserv Eval Eng*. 2009;12(02):218-231.

doi: 10.2118/105378-PA

29. Maultzsch S, Chapman M, Liu E, Li XY. Modelling and analysis of attenuation anisotropy in multi azimuth VSP data from the Clair field. *Geophys Prospect*. 2007;55:627-642.

doi: 10.1111/j.1365-2478.2007.00645.x

30. Far ME, Wagner D, Hardage B. Fracture parameter inversion for marcellus shale. *Geophysics*. 2014;79(3):55-63.

doi: 10.1190/geo2013-0236.1

31. Li MQ. *Seismic Response Analysis and Parameter Inversion of Monoclinic Media*. Beijing: China University of Geosciences; 2023.

32. Helbig K. *Foundations of Anisotropy for Exploration Seismics*. United Kingdom: Pergamon Press; 1994. p. 22.

33. Tsvankin I. *Seismic Signatures and Analysis of Reflection Data in Anisotropic Media. Society of Exploration Geophysicists*. Netherlands: Elsevier; 2012.

34. Iverson WP. Closure STRESS Calculations in Anisotropic Formations. In: *SPE Low Permeability Reservoirs Symposium, Society of Petroleum Engineers*; 1995.

Equations

$$s_T = \begin{pmatrix} \frac{1}{E}+\mathrm{Zn}\sin^4(\theta)+\frac{1}{4}\mathrm{Zt}\sin^2(2\theta) & -\frac{\nu}{E} & -\frac{\nu}{E}+\mathrm{Zn}\sin^2(\theta)\cos^2(\theta)-\frac{1}{4}\mathrm{Zt}\sin^2(2\theta) & -\frac{\nu}{E} & -\mathrm{Zn}\sin(2\theta)\sin^2(\theta)-\frac{1}{2}\mathrm{Zt}\sin(2\theta)\cos(2\theta) & 0 \\ -\frac{\nu}{E} & -\frac{1}{E} & 0 & 0 & 0 & 0 \\ -\frac{\nu}{E}+\mathrm{Zn}\sin^2(\theta)\cos^2(\theta)-\frac{1}{4}\mathrm{Zt}\sin^2(2\theta) & -\frac{\nu}{E} & \frac{1}{E}+\mathrm{Zn}\cos^4(\theta)+\frac{1}{4}\mathrm{Zt}\sin^2(2\theta) & 0 & -\mathrm{Zn}\sin(2\theta)\cos^2(\theta)+\frac{1}{2}\mathrm{Zt}\sin(2\theta)\cos(2\theta) & 0 \\ 0 & 0 & 0 & \frac{1}{\mu}+\mathrm{Zt}\cos^2(\theta) & 0 & -\mathrm{Zt}\sin(\theta)\cos(\theta) \\ -\mathrm{Zn}\sin(2\theta)\sin^2(\theta)-\frac{1}{2}\mathrm{Zt}\sin(2\theta)\cos(2\theta) & 0 & -\mathrm{Zn}\sin(2\theta)\cos^2(\theta)+\frac{1}{2}\mathrm{Zt}\sin(2\theta)\cos(2\theta) & 0 & \frac{1}{\mu}+\mathrm{Zn}\sin^2(2\theta)+\mathrm{Zt}\cos^2(2\theta) & 0 \\ 0 & 0 & 0 & -\mathrm{Zt}\sin(\theta)\cos(\theta) & 0 & \frac{1}{\mu}+\mathrm{Zt}\sin^2(\theta) \end{pmatrix} \quad \text{(XXII)}$$

$$S_{VTI} = \begin{pmatrix} \frac{c_{11b}c_{33b}-c_{13b}^2}{4c_{66b}\left(c_{11b}c_{33b}-c_{33b}c_{66b}-c_{13b}^2\right)} & \frac{2c_{66b}c_{33b}+c_{13b}^2-c_{11b}c_{33b}}{4c_{66b}\left(c_{11b}c_{33b}-c_{33b}c_{66b}-c_{13b}^2\right)} & \frac{-c_{66b}c_{13b}}{2c_{66b}\left(c_{11b}c_{33b}-c_{33b}c_{66b}-c_{13b}^2\right)} & 0 & 0 & 0 \\ \frac{2c_{66b}c_{33b}+c_{13b}^2-c_{11b}c_{33b}}{4c_{66b}\left(c_{11b}c_{33b}-c_{33b}c_{66b}-c_{13b}^2\right)} & \frac{c_{11b}c_{33b}-c_{13b}^2}{4c_{66b}\left(c_{11b}c_{33b}-c_{33b}c_{66b}-c_{13b}^2\right)} & \frac{-c_{66b}c_{13b}}{2c_{66b}\left(c_{11b}c_{33b}-c_{33b}c_{66b}-c_{13b}^2\right)} & 0 & 0 & 0 \\ \frac{-c_{66b}c_{13b}}{2c_{66b}\left(c_{11b}c_{33b}-c_{33b}c_{66b}-c_{13b}^2\right)} & \frac{-c_{66b}c_{13b}}{2c_{66b}\left(c_{11b}c_{33b}-c_{33b}c_{66b}-c_{13b}^2\right)} & \frac{c_{11b}c_{66b}-c_{66b}^2}{c_{66b}\left(c_{11b}c_{33b}-c_{33b}c_{66b}-c_{13b}^2\right)} & 0 & 0 & 0 \\ 0 & 0 & 0 & \frac{1}{c_{44b}} & 0 & 0 \\ 0 & 0 & 0 & 0 & \frac{1}{c_{44b}} & 0 \\ 0 & 0 & 0 & 0 & 0 & \frac{1}{c_{66b}} \end{pmatrix}_{6\times 6} \quad \text{(XXXIV)}$$

$$N_\theta S_f N_\theta^T = \begin{pmatrix} Z_N\sin^4(\theta)+\frac{1}{4}Z_T\sin^2(2\theta) & 0 & Z_N\sin^2(\theta)\cos^2(\theta)-\frac{1}{4}Z_T\sin^2(2\boldsymbol{\theta}) & 0 & -Z_N\sin(2\theta)\sin^2(\theta)-\frac{1}{2}Z_T\sin(2\theta)\cos(2\theta) & 0 \\ 0 & 0 & 0 & 0 & 0 & 0 \\ Z_N\sin^2(\theta)\cos^2(\theta)-\frac{1}{4}Z_T\sin^2(2\theta) & 0 & Z_N\cos^4(\theta)+\frac{1}{4}Z_T\sin^2(2\theta) & 0 & -Z_N\sin(2\theta)\cos^2(\boldsymbol{\theta})+\frac{1}{2}Z_T\sin(2\theta)\cos(2\theta) & 0 \\ 0 & 0 & 0 & Z_T\cos^2(\theta) & 0 & -Z_T\sin(\theta)\cos(\theta) \\ -Z_N\sin(2\boldsymbol{\theta})\sin^2(\theta)-\frac{1}{2}Z_T\sin(2\theta)\cos(2\theta) & 0 & -Z_N\sin(2\theta)\cos^2(\theta)+\frac{1}{2}Z_T\sin(2\boldsymbol{\theta})\cos(2\theta) & 0 & Z_N\sin^2(2\theta)+Z_T\cos^2(2\theta) & 0 \\ 0 & 0 & 0 & -Z_T\sin(\theta)\cos(\theta) & 0 & Z_T\sin^2(\theta) \end{pmatrix} \quad \text{(XXXV)}$$

Appendix A

The elements in **Equation XXXVII** are explained as follows in **Equations AI–AXII**:

$$S_{11m}=\frac{M^2(\delta-\varepsilon)-(\delta+1)\mu M+\mu\left(\mu-\sqrt{(M-\mu)(-\mu+2\delta M+M)}\right)}{2(2\gamma+1)\mu\left(2M^2(\delta-\varepsilon)+\mu M(2\gamma-2\delta-1)+2\mu\left(\mu-\sqrt{(M-\mu)(-\mu+2\delta M+M)}\right)\right)}+\mathrm{Zn}\sin^4(\theta)+\frac{1}{4}\mathrm{Zt}\sin^2(2\theta) \quad \text{(AI)}$$

$$S_{12m}=\frac{M^2(\varepsilon-\delta)+\mu M(\delta-2\gamma)+\mu\left(\sqrt{(M-\mu)(-\mu+2\delta M+M)}-\mu\right)}{2(2\gamma+1)\mu\left(2M^2(\delta-\varepsilon)+\mu M(2\gamma-2\delta-1)+2\mu\left(\mu-\sqrt{(M-\mu)(-\mu+2\delta M+M)}\right)\right)} \quad \text{(AII)}$$

$$S_{13m}=\frac{-\sqrt{(M-\mu)(M+2M\delta-\mu)}+\mu}{4M^2(-\delta+\varepsilon)+2M(1-2\gamma+2\delta)\mu+4\left(\sqrt{(M-\mu)(M+2M\delta-\mu)}-\mu\right)\mu}+\mathrm{Zn}\sin^2(\theta)\cos^2(\theta)-\frac{1}{4}\mathrm{Zt}\sin^2(2\theta) \quad \text{(AIII)}$$

$$S_{15m}=-\mathrm{Zn}\sin(2\theta)\sin^2(\theta)-\frac{1}{2}\mathrm{Zt}\sin(2\theta)\cos(2\theta) \quad \text{(AIV)}$$

$$S_{22m}=\frac{M^2(\delta-\varepsilon)-(\delta+1)\mu M+\mu\left(\mu-\sqrt{(M-\mu)(-\mu+2\delta M+M)}\right)}{2(2\gamma+1)\mu\left(2M^2(\delta-\varepsilon)+\mu M(2\gamma-2\delta-1)+2\mu\left(\mu-\sqrt{(M-\mu)(-\mu+2\delta M+M)}\right)\right)} \quad \text{(AV)}$$

$$S_{23m}=\frac{-\sqrt{(M-\mu)(M+2M\delta-\mu)}+\mu}{4M^2(-\delta+\varepsilon)+2M(1-2\gamma+2\delta)\mu+4\left(\sqrt{(M-\mu)(M+2M\delta-\mu)}-\mu\right)\mu} \quad \text{(AVI)}$$

$$S_{33m}=\frac{M^2(\delta-\varepsilon)-(\delta+1)\mu M+\mu\left(\mu-\sqrt{(M-\mu)(-\mu+2\delta M+M)}\right)}{2(2\gamma+1)\mu\left(2M^2(\delta-\varepsilon)+\mu M(2\gamma-2\delta-1)+2\mu\left(\mu-\sqrt{(M-\mu)(-\mu+2\delta M+M)}\right)\right)}+\mathrm{Zn}\cos^4(\theta)+\frac{1}{4}\mathrm{Zt}\sin^2(2\theta) \quad \text{(AVII)}$$

$$S_{35m}=-\mathrm{Zn}\sin(2\theta)\cos^2(\theta)+\frac{1}{2}\mathrm{Zt}\sin(2\theta)\cos(2\theta) \quad \text{(AVIII)}$$

$$S_{44m}=\frac{1}{\mu}+\mathrm{Zt}\cos^2(\theta) \quad \text{(AIX)}$$

$$S_{46m}=-\mathrm{Zt}\sin(\theta)\cos(\theta) \quad \text{(AX)}$$

$$S_{55m}=\frac{1}{\mu}+\mathrm{Zn}\sin^2(2\theta)+\mathrm{Zt}\cos^2(2\theta) \quad \text{(AXI)}$$

$$S_{66m}=\frac{1}{(1+2\gamma)\mu}+\mathrm{Zt}\sin^2(\theta) \quad \text{(AXII)}$$

where ε, γ, and δ are Thomsen anisotropy parameters. ε describes the difference in the P-wave velocity between the vertical and horizontal directions, while γ describes the difference in the S-wave velocity between the vertical and horizontal directions. *M* is the longitudinal wave modulus, representing the ratio of axial stress to axial strain under a uniaxial strain condition.

RETRACTION NOTE

DOI: 10.36922/jse.corr062725
Published online: June 27, 2025

Ba J, Chen J, Guo Q, Chen X, Yan X, Fang Z. Bayesian linearized inversion for petrophysical and pore-connectivity parameters with seismic elastic data of carbonate reservoirs. *Journal of Seismic Exploration*. 2024;33(1):1–24.

This article is retracted at the request of the authors and with the approval of the Editor-in-Chief of *Journal of Seismic Exploration*. The article was originally published while the journal was still under the management of the former publisher, prior to its acquisition by AccScience Publishing.

The prime reason for this retraction is duplicate publication of the same article, which arose from an unintentional error committed by the authors and an editorial oversight in the former publisher's workflow. During the proofreading process, the authors inadvertently uploaded a different manuscript—the one intended for submission to another journal—onto the submission platform. Due to an editorial oversight at that time, the wrongly uploaded manuscript was published without proper article verification in the *Journal of Seismic Exploration*, while the previously accepted manuscript (Dong H, Ba J, Zhang M, Carcione J M, Pang M, Tan W. 3D rock-physics templates for estimating the reservoir properties of interbedded sandstone and shale thin layers) was not published. The wrongly uploaded manuscript was intended for submission to the *Journal of Geophysics and Engineering* and has been published therein (doi: 10.1093/jge/gxae076).

All authors are aware of this issue and agree to this retraction.

Publisher's Note: AccScience Publishing acquired *Journal of Seismic Exploration* after the original publication of this article. AccScience Publishing remains committed to maintaining ethical standards and transparency in academic publishing and remains neutral with regard to jurisdictional claims in published maps and institutional affiliations.

Our Journals

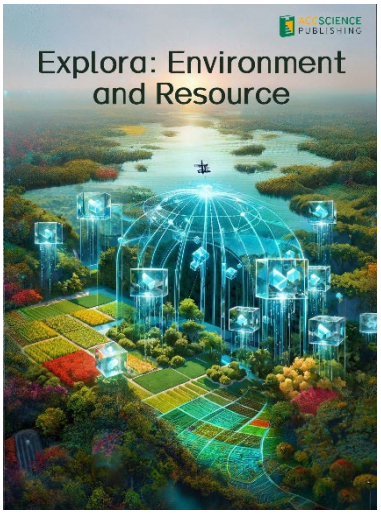

Explora: Environment and Resource (EER) is an international and multidisciplinary journal covering all aspects of the environmental impacts of socio-economic development. It is concerned with the complex interactions among society, development, and the environment, aiming to explore ways and means of achieving sustainability in all human activities related to development.

EER covers subject areas, including but not limited to the following:

- Water reclamation, wastewater treatment and waste management for eco-environment sustainability
- Innovative nanotechnology, catalysis, photocatalysis and nano materials for decontamination practices and renewable energy resources.
- Climate change-related sustainable resource and environment quality analysis
- Microorganisms and plants-oriented low-carbon processes and strategies for clean energy, water and resource management

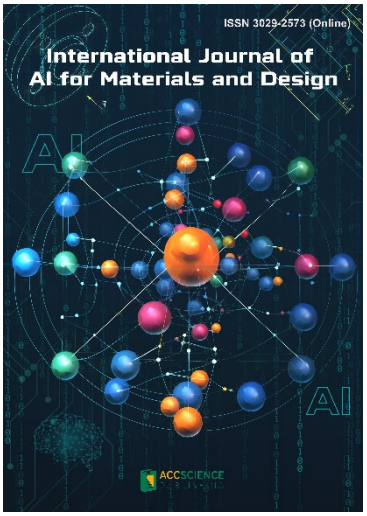

International Journal of AI for Materials and Design is an international, peer-reviewed open-access journal that aims to bridge the cutting-edge research between AI and materials, AI and design. In recent years, the tremendous progress in AI is leading a radical shift of AI research from a mainly academic endeavor to a much broader field with increasing industrial and governmental investments. The maturation of AI technology brings about a step change in the scientific research of various domains, especially in the world of materials and design. Machine learning (ML) algorithms enable researchers to analyze extensive datasets on material properties and accurately predict their behavior in different conditions. This subsequently impact the industry to leverage on big data and advanced analytics to build scientific strategies, scale operational performance of processes and drive innovation. In addition, AI and ML are uniquely positioned to enable advanced manufacturing technologies across the value chain of different industries. Integration of multiple and complementary AI techniques, such as ML, search, reasoning, planning, and knowledge representation, will further accelerate advances in scientific discoveries, engineering excellence and the future of cyber-physical systems manufacturing.

International Journal of AI for Materials and Design covers the following topics: AI or machine learning for material discovery, AI for process optimization, AI and data-driven approaches for product or systems design, application of AI in advanced manufacturing processes such as additive manufacturing, IoT, sensors, robotics, cloud-based manufacturing, intelligent manufacturing for various applications, autonomous experiments, material intelligence, energy intelligence, and AI-linked decarbonization technologies.

Start a new journal

Write to us via email if you are interested to start a new journal with AccScience Publishing. Please attach your CV, professional profile page and a brief pitch proposal in your email. We shall inform you of our decision whether we are interested to collaborate in starting a new journal.

Contact: info@accscience.com

https://accscience.com/journal/JSE

Access Science Without Barriers

Contact

www.accscience.com
9 Raffles Place, Republic Plaza 1 #06-00 Singapore 048619
E-mail: editorial@accscience.com
Phone: +65 8182 1586